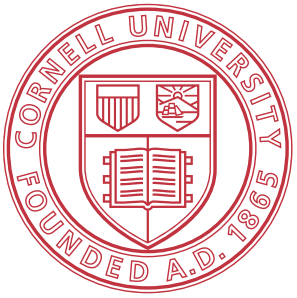

Cornell University

Modular Active Self-Assembling Space Telescope Swarms

NIAC PHASE I, FINAL REPORT: 17-NIAC18B-0165

PI: DMITRY SAVRANSKY (CORNELL UNIVERSITY, CARL SAGAN INSTITUTE)

STUDY TEAM: DEAN KEITHLY, JACOB SHAPIRO, GABRIEL SOTO, ERIK GUSTAFSON,
KEVIN LIU, CHRISTOPHER DELLA SANTINA

EXECUTIVE SUMMARY

Current trends in astrophysical instrumentation and an extrapolation of the science cases currently being explored by the astrophysical community make it highly likely that there will be a future demand for giant (30+ m diameter) space telescopes. However, current explorations of next generation mission concepts such as the Large Ultraviolet/Optical/Infrared Surveyor (LUVOIR) at even the 15 m diameter scale are already straining our capabilities for manufacturing and launching such telescopes from the ground. Projections based on extrapolations of construction experiences with other space telescopes including the Hubble and James Webb Space Telescopes suggest that a 30+ m scale space telescope, approached with previously proven construction techniques, would cost in excess of 100 billion dollars and would take more than half a century to construct. Similarly, even under the assumption of new heavy launch vehicles coming online in the future, it is unlikely that a 30 m diameter structure could possibly be packaged without extreme difficulties and potentially mission-endangering deployment complexity.

To address the perceived need of this class of telescope along with the engineering challenges it entails, we propose a modular, self-assembling architecture that would construct a giant primary mirror, on-orbit, from identical, mass-produced modules. This approach would allow us to leverage the time and cost benefits of true mass production, while avoiding packaging complexity and actually allowing for components of the telescope to all be launched (over a period of years) as payloads of opportunity. The individual modules would use solar sails for propulsion, allowing them to gradually navigate to their intended final orbit and rendezvous without carrying significant quantities of propellant. The solar sails would further be repurposed into the planar sunshield for the assembled structure, thereby minimizing mass waste.

The Phase I study included a detailed exploration of a specific mission concept based on this architecture – a 31 m diameter version of the LUVOIR mission concept with the same wavelength coverage and wavefront quality requirements. The study focused on establishing the feasibility of the proposed concept with respect to what were identified as the most challenging aspects of the mission: the ability to find orbital solutions using solar sail propulsion for both the initial transfers and subsequent rendezvous trajectories; and the ability to generate the required final primary mirror surface out of uniformly polished individual module mirrors using deformation via mechanical degrees of freedom.

As a result of the Phase I work it was shown that both orbital and optical solutions are feasible, but will require technology advancement in multiple key areas. In particular, improvements to solar sail areal densities and loading factors will allow us to more easily find fully general solutions for the transfer trajectories, while lower mass, ultra-precise cryogenic linear actuators will likely be needed to form the final mirror shape. However, it was found that current state of the art in solar sails was sufficient for rendezvous trajectories once on-orbit, that the requisite wavefront quality could be achieved with actuation requirements not more stringent than those being carried by LUVOIR, and that there exists a well define design space in which the module spacecraft designs can be optimized.

The technology development required to progress this work overlaps significantly with numerous NASA technology roadmaps, as well as the Exoplanet Exploration Program's technologies gap list, meaning that continued development of this concept would directly benefit a variety of NASA programs, as well as enabling the completely unique capabilities provided by a 31 m optical space telescope.

TABLE OF CONTENTS

1 INTRODUCTION

Despite the significant advances in extreme adaptive optics for ground-based imaging systems [1] and current plans for the next generation of giant, ground-based observatories [2], there are fundamental limits to the space science that can be achieved from the ground, meaning that space-based astrophysical observatories will continue to form an indispensable part of the observational assets available to researchers. The Hubble space telescope was unequivocally transformative in its contributions to a broad range of studies, and we fully expect that the James Webb Space Telescope (JWST) will make equally important contributions after its launch. At the same time, the astrophysics community has clearly indicated the need for even larger space-based apertures to enable new science cases with ever higher spatial and spectral resolution needs, targeting ever-fainter objects such as distant galaxies and Earth-like exoplanets. This is evidenced by the Large Ultraviolet/Optical/Infrared Surveyor (LUVOIR) mission concept. Highlighted in the NASA Astrophysics Roadmap [3], and currently being studied for the 2020 decadal survey, the LUVOIR concept features an 8 - 16 m aperture supporting instruments covering a broad wavelength range with numerous highly exciting science cases.

Unfortunately, the construction of this scale of telescope using previously proven approaches of Hubble and JWST will be extraordinarily challenging [4], and likely completely untenable for even larger apertures. It is also highly likely that the astrophysical community will want space telescopes beyond the 16 m class in the future. Taking just a small subset of the science cases discussed in the LUVOIR interim report [5], we can consider the impact of increased aperture sizes on our understanding of galactic evolution and planetary formation.

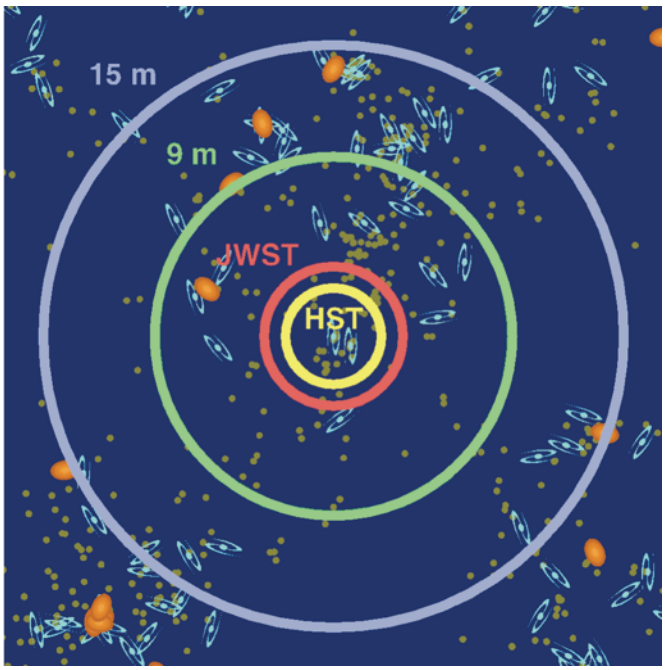

Figure 1: From: LUVOIR Interim Report [5]. Figure by T. Brown. Observability of main sequence turnoff at different telescope scales (represented by colored circles) overlaid on a schematic view of the observable universe. A 31 m telescope would effectively be sensitive to the main sequence turnoff (at SNR of 5 in 100 hours of integration) throughout this entire volume of space.

Figure 1, from the LUVOIR interim report, shows a schematic view of the observable universe along with the sensitivity (at SNR = 5) to the main-sequence turnoff in 100 hours of integration time in the V and I bands for various apertures. These are key measurements when fitting galactic evolution models to color-magnitude diagrams (CMDs), and while a 15 m-class LUVOIR would allow us to expand our measurement capability beyond the local group, a 31 m-version would effectively expand this measurement to the full observable universe, allowing us to capture the full diversity of galaxies in space and time.

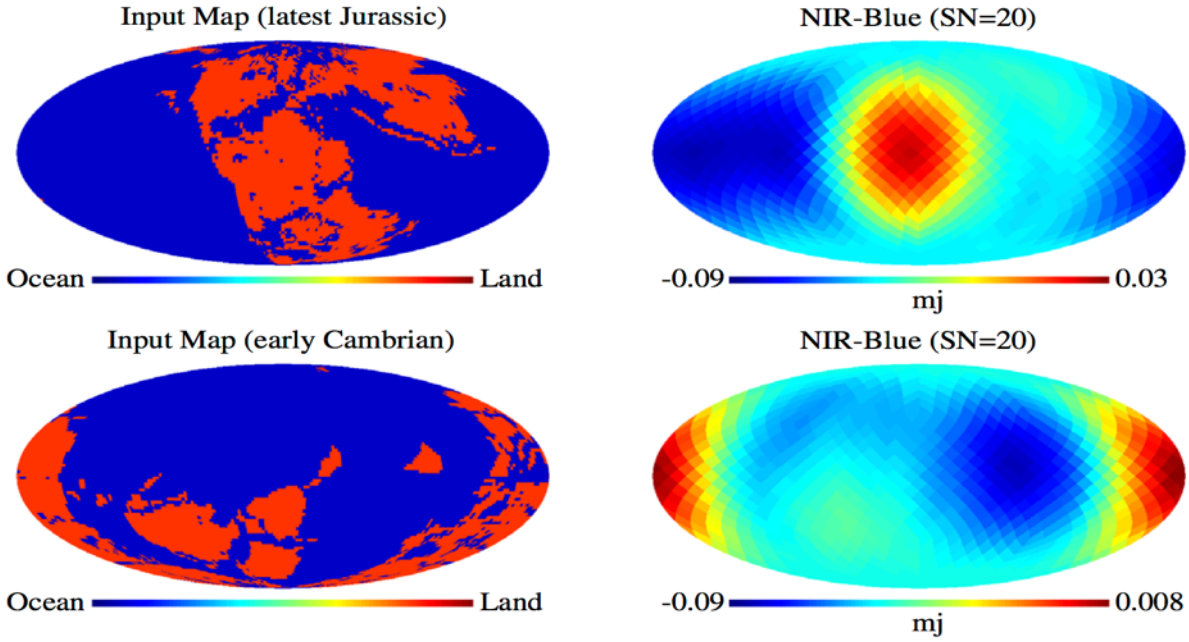

Figure 2: From: Fujii & Kawahara (2012). Left: Input surface maps of land distributions based on paleomaps of the latest Jurassic (upper panels) and early Cambrian (lower panels). Right: Reconstructed surface cover maps at effective SNR of 20. The color scale on the left-hand panels represents the surface cover type, while the color scale on right-hand panels is proportional to the reconstructed albedo of the surface.

Figure 2, from Fuji and Kawahara (2012) [6], shows the reconstruction of surface cover distributions for an observed exoplanet matching the continental distribution of Earth at two points in its geological history. These measurements make use of the spin–orbit tomography (SOT) technique, which the authors derived to enable the generation of two-dimensional albedo maps from annual variations of the disk-integrated scattered light detected from a directly imaged exoplanet. This technique inherently requires time-resolved photometry of Earth-like exoplanets in order to derive the planets' spin rates, and therefore can only be achieved with a space telescope with a large collecting area and small angular resolution. While Fuji and Kawahara estimated that this technique could be applied to an Earth-sized planet at 10 pc with a 5 m aperture, and to one at 100 pc with a 15 m aperture, our increased understanding of wavefront control challenges and the construction of coronagraphs for large, segmented aperture (due largely to the WFIRST technology development programs and the LUVOIR investigations) indicate that we will actually need apertures beyond 15 m to push beyond even 30 pc of distance for these measurements. Given our current understanding of exoplanet demographics and the occurrence rates of Earth-like planets (as

extrapolated from Kepler and other survey results [7]), we can only expect a high confidence of getting at least one such measurement (> 95%) at the 30+ m aperture scale.

Beyond these two specific cases, similar arguments can be made for the enhancement of other science cases including a complete census of directly imaged exoplanets at all scales of masses, ages, and orbital separations, the search of biosignatures in exoplanet atmospheres, the study of galactic assembly at the infancy of the universe, the search for ultra-faint dwarf galaxies in the age of re-ionization, and the study of the earliest stars and the emergence of the first metals.

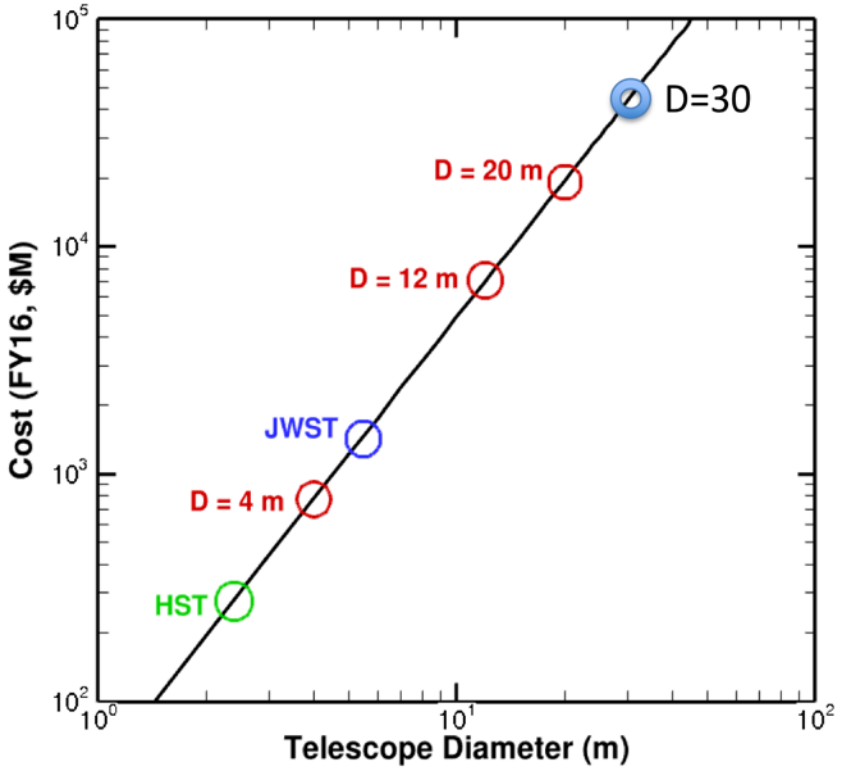

Figure 3: Adapted from Boyd et al. (2017), based on modeling from Stahl et al. (2013). Projected cost of the optical telescope assembly, based on historical examples, as a function of the aperture diameter. The OTA cost fraction of the total mission cost also grows linearly with telescope diameter and OTA costs can scale by as much as aperture diameter squared. Based on this model a 30 m telescope OTA (alone) would cost in excess of $50 billion FY16 dollars.

While the science cases are all uniformly enhanced with the introduction of increased aperture scale (assuming no sacrifice in wavefront quality), the engineering challenges of such a mission become increasingly harder. Figure 3 shows the trend in optical telescope assembly (OTA) cost as a function of aperture diameter as derived in Stahl et al. (2013) [8]. The basic findings of this work were that an extrapolation of historical time and cost complexity of the OTA could result in a a second-order dependence on aperture diameter, while the fraction of total telescope cost taken up by the OTA scales linearly with diameter. This means that the construction of a 31 m aperture space telescope using techniques derived from Hubble and JWST would result in mission costs in the hundreds of billions of dollars, and construction times in excess of 50 years. Clearly, a mission

with such a cost and time profile would never be considered for selection, and a different approach is needed to even consider the construction of 30+ m space telescopes.

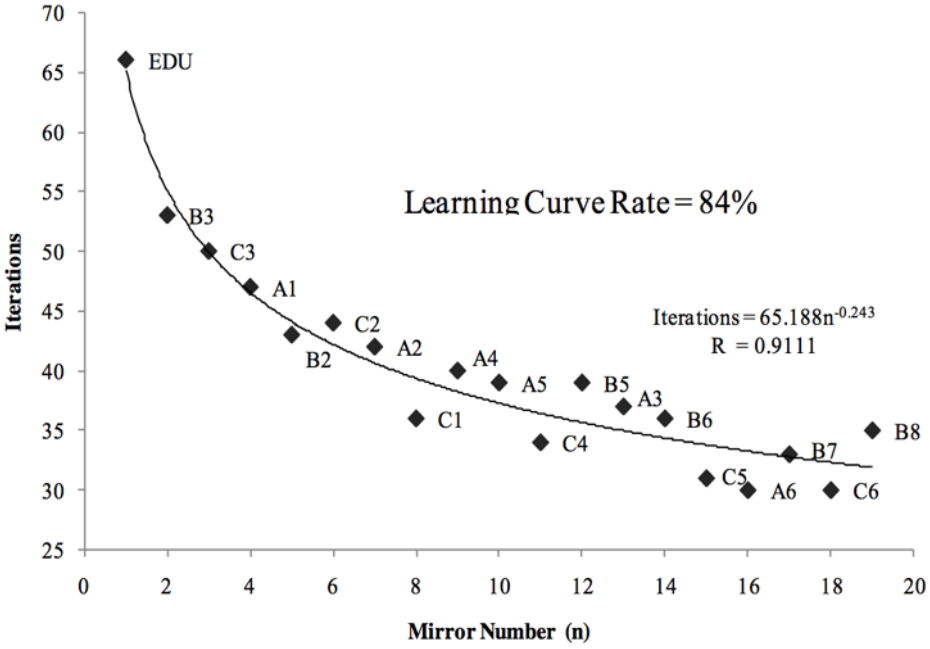

Figure 4: From: Stahl et al. (2016). Number of iterations required for polishing 19 JWST mirror segments as a function of the segment number (in the order of polishing) and a best-fit learning curve. The derived learning curve rate is 84%.

At the same time, it has also clearly been shown that the cost and time benefits of mass production apply to the fabrication of OTA elements, and, in particular, to mirror segments. Figure 4 shows a learning curve from Stahl et al. (2016) [9] derived for the polishing of the JWST mirror segments. The learning curve rate of over 80% indicates that each successive mirror was approximately 80% the cost of the previous one manufactured, and this result was found to be consistent with the experience of other segmented telescopes including CHARA, LBT, HET, and Keck. While the production costs of items cannot be infinitely reduced, and must reach some steady state value, the fits to these previous examples show that additional time/cost benefits can be achieved past tens of units, meaning that a 31 m telescopes with hundreds of mirror segments can attain significant cost savings, particularly if every component in the system is identical.

Finally, there is the significant limit of available launch fairing sizes, which, even with the projected next generation of heavy launch vehicles, will be limited to approximately 9 m in diameter, and is currently at 5.4 m. These limitations have a significant impact on the packaging and deployment complexity of giant aperture space telescopes, driving such concepts towards on-orbit assembly.

To directly address all of the difficulties and leverage the time and cost savings inherent in true mass production, we propose a modular, self-assembling architecture enabling the construction of a giant (31 m diameter), reflective space telescope with active optics.

1.1 Mission Concept and Architecture

The final structure of the primary mirror will be composed of identical, mass produced spacecraft modules. Each module, shown schematically in Figure 61 is a hexagonal spacecraft attached via an extensible, semi-rigid tether to a deployable and reefable solar sail. The sail is reflective on the top (spacecraft-facing) surface and highly absorptive on the bottom surface. Overlapped sails will form the sunshield for the assembled telescope. The module is topped by a polished, active mirror measuring 1 m flat-to-flat and 1.1547 m tip-to-tip. All modules have identically surfaced mirrors. The mirror backplane sits on top of the spacecraft on a Stewart platform, and linear actuators between the mirror and backplane set the mirror to its final required shape.

Modules will be launched as payloads of opportunity over a span of approximately seven years. After separation from the launch vehicle, each module will deploy its solar sail and navigate to the vicinity of the Sun-Earth L2 point where it will enter a quasi-periodic Lissajous parking orbit (see Figure 40). As modules come within 1000 km of one another (which the quasi-periodic orbit and random phasing guarantee will occur regularly), they will again use their solar sails to rendezvous and then join, as shown schematically in Figure 5. Controllable electromagnets on the spacecraft bodies will be used for final orientation and fine alignment and mechanical locking mechanisms will provide the final, rigid connections between neighboring modules.

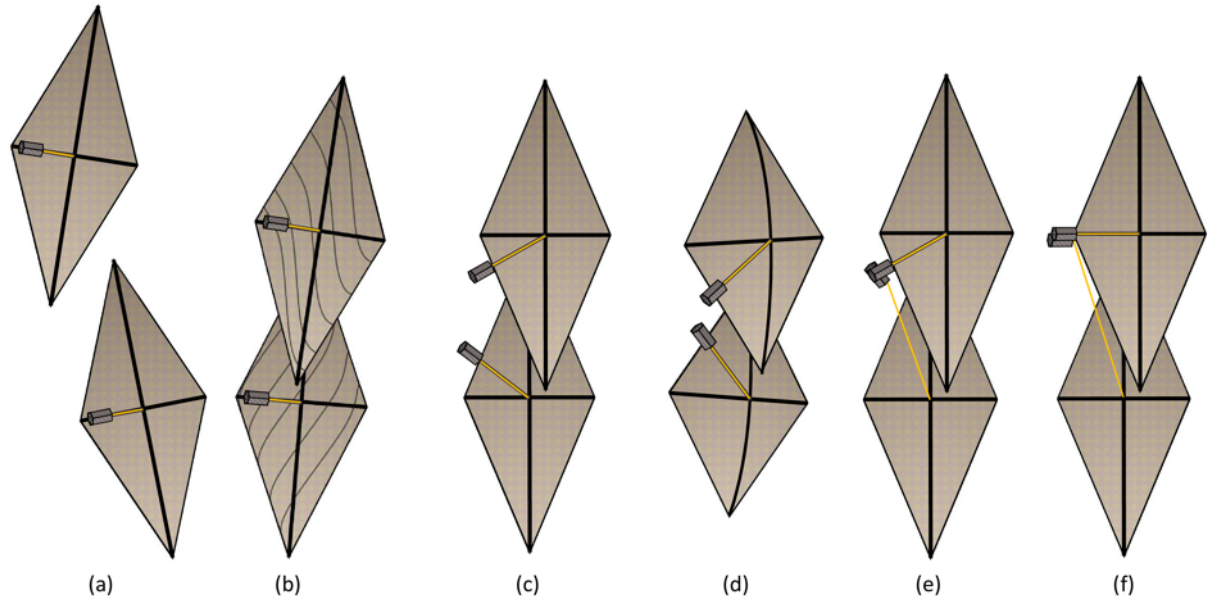

Figure 5: Schematic of module docking. (a) A module places itself on an intercept trajectory with another module or sub-assembly. (b) The sails make contact and stick via embedded hook-and-loop material or hooks on the booms. Energy is dissipated via sail vibration. (c-d) The sails reef their facing sides and the spacecraft pivot (using module ACS/RCS) on their extended tethers. (e) Controllable electromagnets on the modules' sides force them into the proper orientation and alignment. (f) Mechanical interconnects link the modules, the sails unfurl and one tether is optionally released (based on the size of the sub-assembly).

Individual modules will continue to autonomously join until a sub-assembly has reached a critical size of 14 modules in any radial direction. Critically sized sub-assemblies will then be guided into the final assembly using a combination of the joined sails, on-board reaction mass, and with potential input from ground controllers. The final telescope primary will be composed of 840 joined modules, while their overlapped solar sails simultaneously form a planar sunshield, with enough control retained over the sunshield orientation to allow for limited propulsion capability. The whole structure will transition to a fully periodic halo orbit about L2 and a secondary mirror and instrumentation package will be independently launched and dock with the structure, completing the telescope, as in Figure 6.

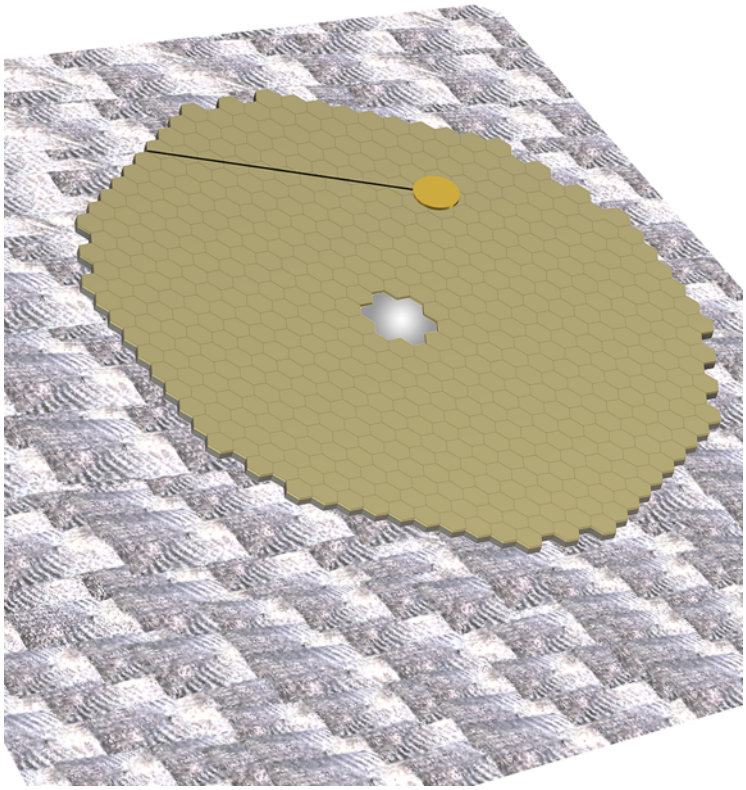

Figure 6: Schematic of the full primary assembly, consisting of 840 modules, and the assembled sunshield. Separate spacecraft provide the secondary and instrument package, which docks between the primary and sunshield. Extensible tethers (not shown for clarity) connect the sunshield to the primary mirror and carry power from solar panels on the face of the sunshield.

Attitude control for the full structure will be achieved by using the attitude and reaction control systems (ACS/RCS) of all of the modules in concert, with sensing provided by the module sensors on the outer edge of the structure. Power will be obtained from exposed, flexible, photovoltaics on the underside of the sunshield, transmitted to the structure via the remaining attached tethers. The mechanical interconnects between modules will include electrical ports allowing all of the modules to transmit power and communicate/operate in a single mesh network, and pass-through valves allowing for unused reaction mass from interior modules to be transferred to exterior ones. Once fully assembled, the module mirrors will be actuated into their nominal shapes based on their location in the structure, and final precision co-phasing of the primary mirror will be completed

via closed-loop control using wavefront sensing provided by the instrument package. The full assembly will be completed within ten years of the first module launch.

1.2 Mission Context

While this concept is directly applicable to a wide variety of astrophysical missions, the specific mission concept targeted for this study is an expanded version of the Large Ultraviolet/Optical/Infrared Surveyor (LUVOIR). The proposed architecture is a viable, and potentially more economical, alternative to the current LUVOIR formulation, while also allowing us to consider construction of even larger aperture scales in the same timeframe when the LUVOIR mission would be launched. Given this concept focus, we have adopted the mission characteristics (other than aperture) directly from LUVOIR, including the Sun-Earth L2 halo orbit, the wavefront requirements, and the science and instrumentation focus areas, as detailed in the LUVOIR interim report [5].

1.3 Prior Art and Novelty

The proposed architecture features multiple completely new and unique elements amongst existing concepts for modular, reflective space telescopes. Unlike the majority of previously proposed on-orbit assembly concepts, which focus on human or robotic assembly [10, 11, 12, 13], our concept requires no specialized robotic elements and therefore eliminates these single points of failure and keeps the complexity of the initial assembly operations to a minimum. Our architecture requires only a single module type allowing us to directly leverage the cost and efficiency benefits of true mass production, in direct contrast to previously explored self-assembling swarm concepts, which typically include multiple module types [14, 15]. We know of only one mission currently under development that seeks to assemble a primary out of identical sub-mirrors: the AAReST CubeSat demonstration mission [16]. However, this concept seeks only to demonstrate Earth-orbit assembly of a sparse aperture with limited co-phasing, and there is limited discussion available as to how this concept would scale up to a scientifically useful system. Our integrated analysis of the assembly and telescope operations in the context of an expanded LUVOIR-like space telescope makes the proposed concept truly unique.

Similarly, the use of solar sails for both propulsion and to form a sunshield is unique. The only other mention we can find of solar sails in the construction of giant space telescopes is in Izzo et al. (2005) [17], where the sails are used to form sections of the primary mirror itself. However, that work presents no details on how the sail structures could form a reflective surface with sufficiently good optical quality—difficulties that appear insurmountable. Using the sails to form a planar sunshield is significantly more compelling, as the sails must be hundreds of times larger in area than the modules, and will therefore allow for a large, multi-layered sunshield, as has been developed for the James Webb Space Telescope (JWST) and proposed for other large telescope concepts [18].

Finally, while the use of mechanical actuation to achieve precision mirror shape and perform on-orbit segment co-phasing has heritage in the JWST mirror design [19], our implementation significantly increases the degrees of freedom on each segment (from JWST's 7 to over 30), allowing for every segment to be polished to the same figure, and the final shape set depending on where the segment ends up in the assembled structure. The high number of degrees of freedom in the mirrors will produce an active primary which can potentially be used to correct mid spatial-frequency errors in real time, enabling completely new types of instrumentation for a space telescope.

1.4 Phase I Study Overview

The Phase I study focused on establishing the feasibility of the proposed concept with respect to what we consider to be the two 'tall-poles' of the mission:

1. The ability to find orbital solutions using solar sail propulsion for both the initial transfers to the Lissajous parking orbit starting from a broad range of possible launch conditions, and subsequent intercept trajectories on the parking orbit from random phasings.

2. The ability to create the required final primary mirror surface out of uniformly polished individual module mirrors using deformation via mechanical degrees of freedom.

Feasibility in both these areas was demonstrated in Phase I via extensive simulation and modeling efforts, detailed in this report. In addition, Phase I work included refinement of the initial mission concept in response to the findings from the feasibility studies, along with preliminary design activities for the module spacecraft.

This report details the nine months of the NIAC Phase I activities for this project. Section 2 presents the detailed optical design study carried out to assess the feasibility of forming a segmented primary mirror out of identically polished optical surfaces with mechanical degrees of freedom. Section 3 discusses the feasibility of transferring individual modules, launched as payload of opportunity, to the Sun-Earth L2 point using only solar sail propulsion. Section 4 discusses the nominal point design developed in the course of this study for the module spacecraft, along with the design phase space to be used for future optimization, and a preliminary analysis of all spacecraft subsystems.

2 OPTICAL DESIGN

In this section, we discuss the optical design of the telescope including the overall optical path and telescope parameters, the segmentation of the primary mirror, and the shaping of each segment. In each of these areas, a set of new challenges arises from the concept of operations—autonomous self-assembly in space of identical mirror segments on independent spacecraft. We address each of these in turn, and show a complete analysis of the point spread function of the resultant design. The general workflow of this portion of the project occurred in 5 steps:

1. Select telescope parameters
2. Design ideal primary shape
3. Decompose each segment shape into Zernike modes
4. Model the whole system
5. Simulate the system point spread function (PSF)

The last two steps are completed in Zemax OpticStudio, a commercial optical propagation software package.

2.1 Telescope Design

After a careful review of the designs of current space telescopes including Hubble [20] and JWST [21], and current plans for giant, ground-based telescopes, such as the Thirty Meter Telescope [2], a Ritchey-Chrètien Cassegrain design was selected. This particular design, with two hyperbolic mirrors, removes coma and spherical aberrations better than a standard parabolic Cassegrain. These comparisons to similar telescopes and our design goals have led to the selection of the following parameters:

- Primary Aperture d=31m
- Primary focal length F_P of f/2
- Distance from primary to secondary $D = 0.9F_P$
- Total effective focal length F of f/5.6

The size of the primary mirror is set by the mission concept, but we also wish to keep the secondary mirror to within ~ 3 m in diameter, such that it could be manufactured as a monolithic structure. Following the examples of the aforementioned telescopes, which place the secondary mirror at approximately 90% of the primary focal distance places strict limits on the focal length of our system. These two requirements of secondary size and position translate to a maximum f/2 system. In comparison, the TMT telescope is f/1. At exactly 90% of the distance to an f/2 focal point, the secondary mirror is 3.06 m in diameter, meeting the sizing goal. The image plane is placed at 2d behind the primary mirror and the complete optical path is shown in Figure 7.

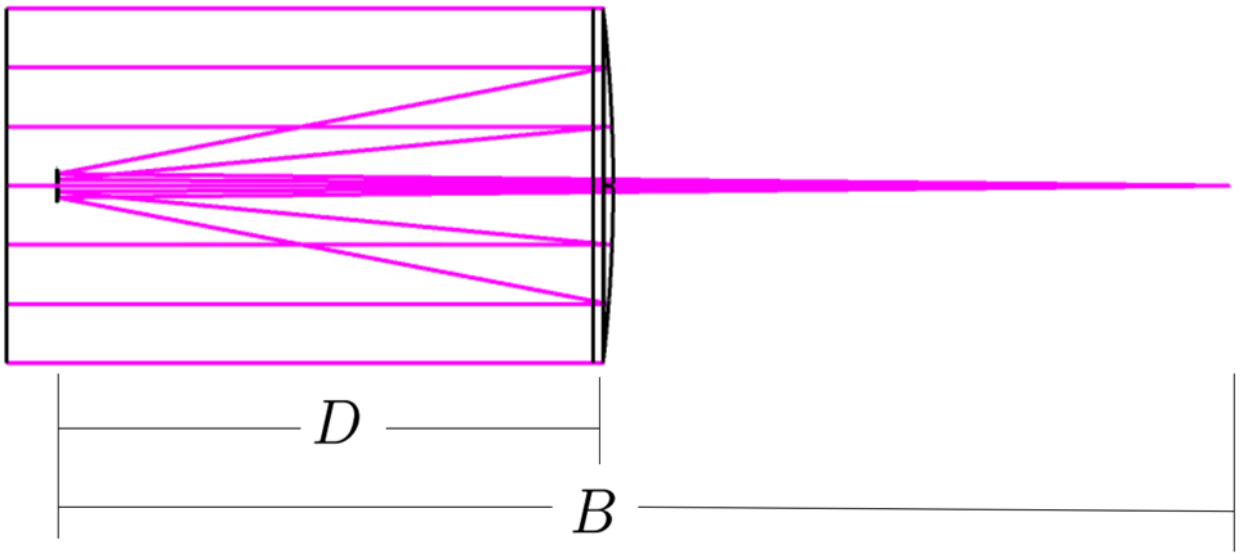

Figure 7: Side view of extended focus, with dimension labels.

The intent is that the beam path will be folded within the instrument package. However, as the instrument package was not the focus of this phase of research, and the specific folding of this path has no impact on determining the feasibility of constructing the primary mirror in space, no detailed analysis was carried out on the instrument package itself. A sample folded focus, that has not been analyzed in detail nor optimized, is shown in Figure 8.

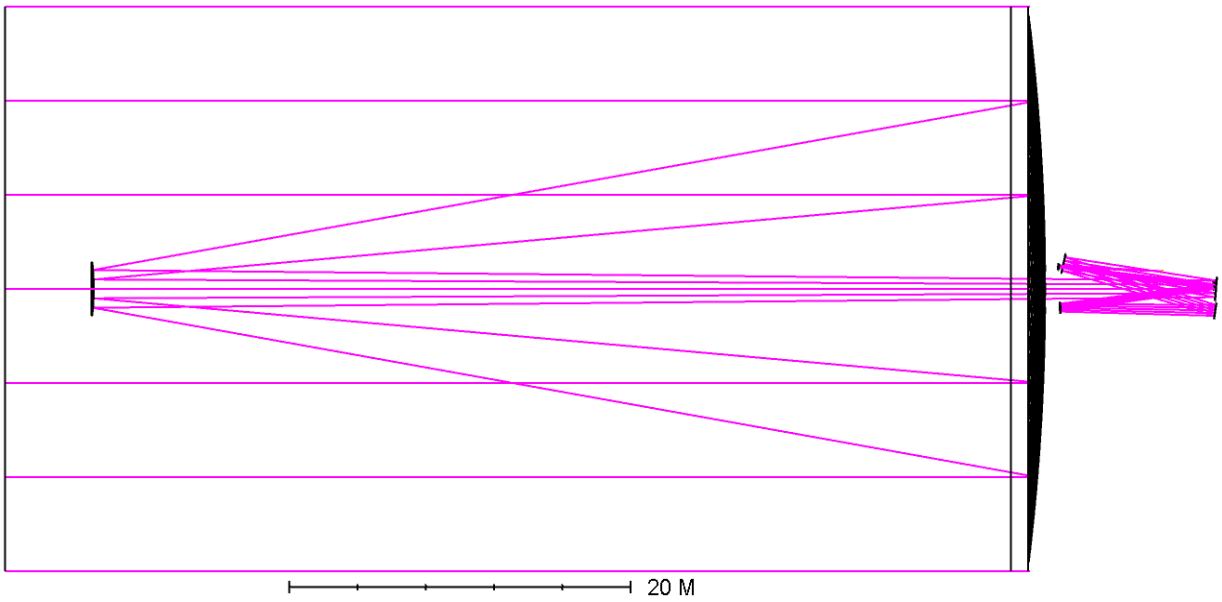

Figure 8: A sample ray trace of the full telescope design, including a folded focus behind the primary mirror.

Using the above parameters, we can evaluate the equations that determine the shape of the mirrors:

- Primary Radius of Curvature

$$R_1 = \frac{DF}{F - B} \tag{1}$$

- Primary Conic Constant

$$K_1 = -1 - \frac{2B}{M^3 D} \tag{2}$$

- Secondary Radius of Curvature

$$R_2 = \frac{2DB}{F - B - D} \tag{3}$$

- Secondary Conic Constant

$$K_2 = -1 - \frac{2}{(M-1)^3}\left[M\left(2M - 1) + \frac{B}{D}\right)\right] \tag{4}$$

- Magnification

$$M = \frac{F - B}{D} \tag{5}$$

These equations describe the radius of curvature at the center of each mirror, and the conic constant for each mirror in a perfect system. Evaluating these equations yields the results in Table 1.

Table 1: Table of values defining the shape of the primary and secondary mirrors

	Radius of Curvature (m)	Conic Constant
Primary	124	-1.000615574022776
Secondary	13.0888888889	-1.241807651272672

The final design produces a primary mirror that is relatively flat, with a large radius of curvature. It also has a nearly parabolic shape, with a conic constant just less than -1. These ensure that segmentation, discussed in Section 2.2, will be a reasonable endeavor. In contrast, the secondary mirror has a much more pronounced curve, and is highly hyperbolic, strengthening the case for manufacturing the secondary as a monolithic mirror.

Using these results, we can describe the shape of a given mirror with

$$z = \frac{R + \sqrt{R^2 - (K+1)r^2}}{K+1}. \tag{6}$$

where *r* is the radial distance from the center of each mirror in the *xy* plane. This design, with all parameters, was modeled and analyzed in Zemax OpticStudio, assuming perfect, monolithic mirrors in both cases. The resultant point spread function from this system, shown in Figure 9, verifies that the system performs ideally.

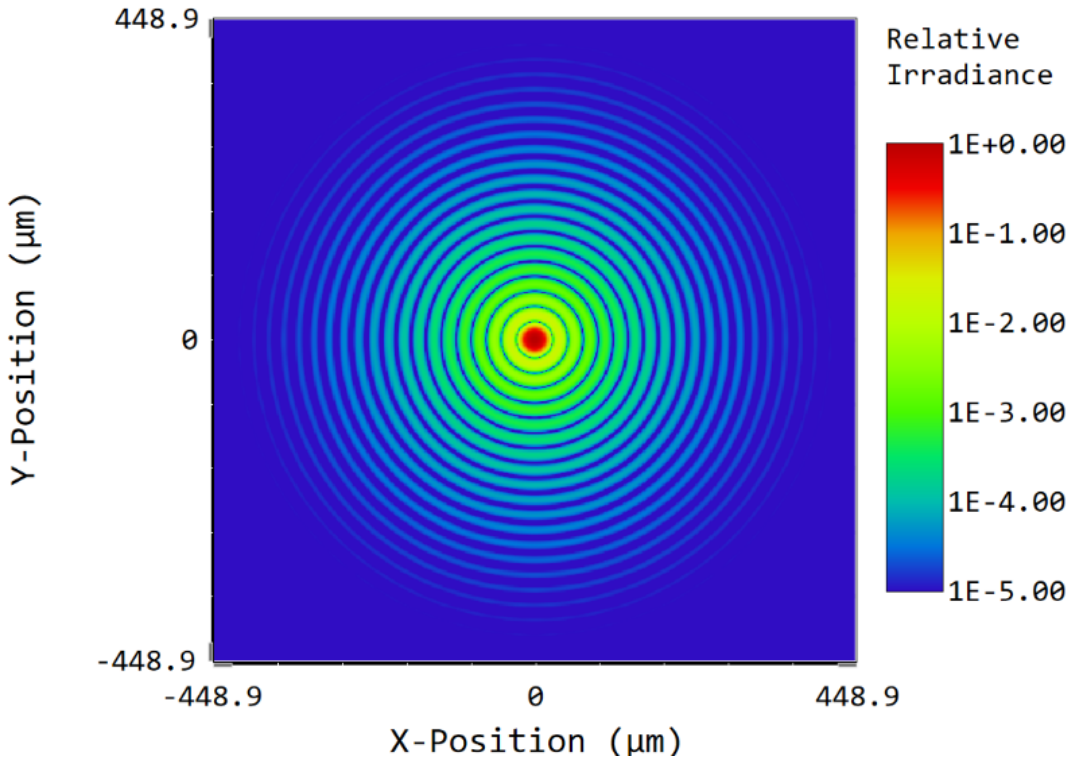

Figure 9: Analysis from Zemax of the point spread function of the ideal mirror displayed in a logarithmic color scale. A central, circular region is shown with a normalized, uniform value of one, surrounded by concentric rings of diminishing strength, as expected for the idealized system.

2.2 Segmentation

Next, the ideal primary shape was decomposed into hexagonal segments sized 1 m flat-to-flat. This sizing lies within the bounds of the design phase space, as discussed in Section 4.4, and was selected as the point design for optical analysis.

2.2.1 Gap Sizes

The first step is to determine the spacing of the mirrors, placing them as close as possible to each other whilst guaranteeing that the segments do not impact one another when tip/tilt corrections are applied to generate the final mirror shape.

The gap between the mirror segments was calculated purely from the mirror geometry, assuming that each mirror had the worst case tip/tilt applied relative to its neighbor. As seen in the Figure 10, the footprint for each mirror's possible position is carved out by the arc with a radius from the center of the surface of a mirror (the point of rotation) to the bottom corner of the mirror. Thus, the worst case scenario for gap size necessary would be described by

$$0.5^2 + t^2 = \left(0.5 + \frac{g}{2}\right)^2 \tag{7}$$

where *g* represents the full gap between the two mirrors. The thickness of the mirror, *t* was calculated by scaling the thickness of the James Webb mirrors based on the mirror diameter of the two designs. This process results in a required gap size of 6 mm.

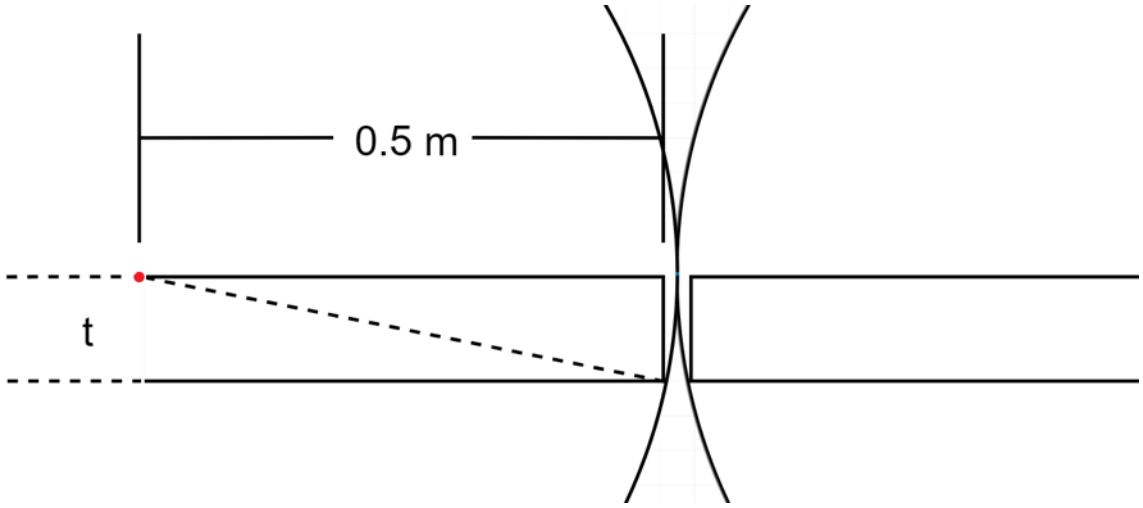

Figure 10: A side view of two adjacent mirrors. These are spaced sufficiently far such that the arcs drawn by the farthest point in worst-case scenario tilt do not intercept each other. This determines the gap spacing.

2.2.2 Center Gap and Edges

Ideally, the primary mirror would have a perfectly circular aperture. However, because of the segmentation and the telescope design, it will have two significant deviations from the ideal circular shape: near the center and at the edge of the aperture.

Because of the Cassegrain design, light must be allowed to pass through the primary to reach the image plane. If all mirrors are the same size, the only solution is to eliminate rings of mirrors near the center. We have calculated the most extreme point where the beam would cross a complete primary, and exclude the segments it intercepts and all mirrors interior.

The edge of the aperture as well will no longer resemble a circle. Along the hexagonal spokes of the primary, targeting a diameter of 31 m is accomplished by placing 15 segments on all sides of a central hex (had the central hex not been removed). However, to more closely approximate a circular aperture, more segments are included beyond the hexagonal pattern in between these spokes. We continue to add more layers beyond 15, eliminating mirrors as needed. The criteria we used was to continue adding segments as long as at least approximately 2/3 of the area of each hexagon is inside the 31 m diameter, leading to the final design shown in Figure 11.

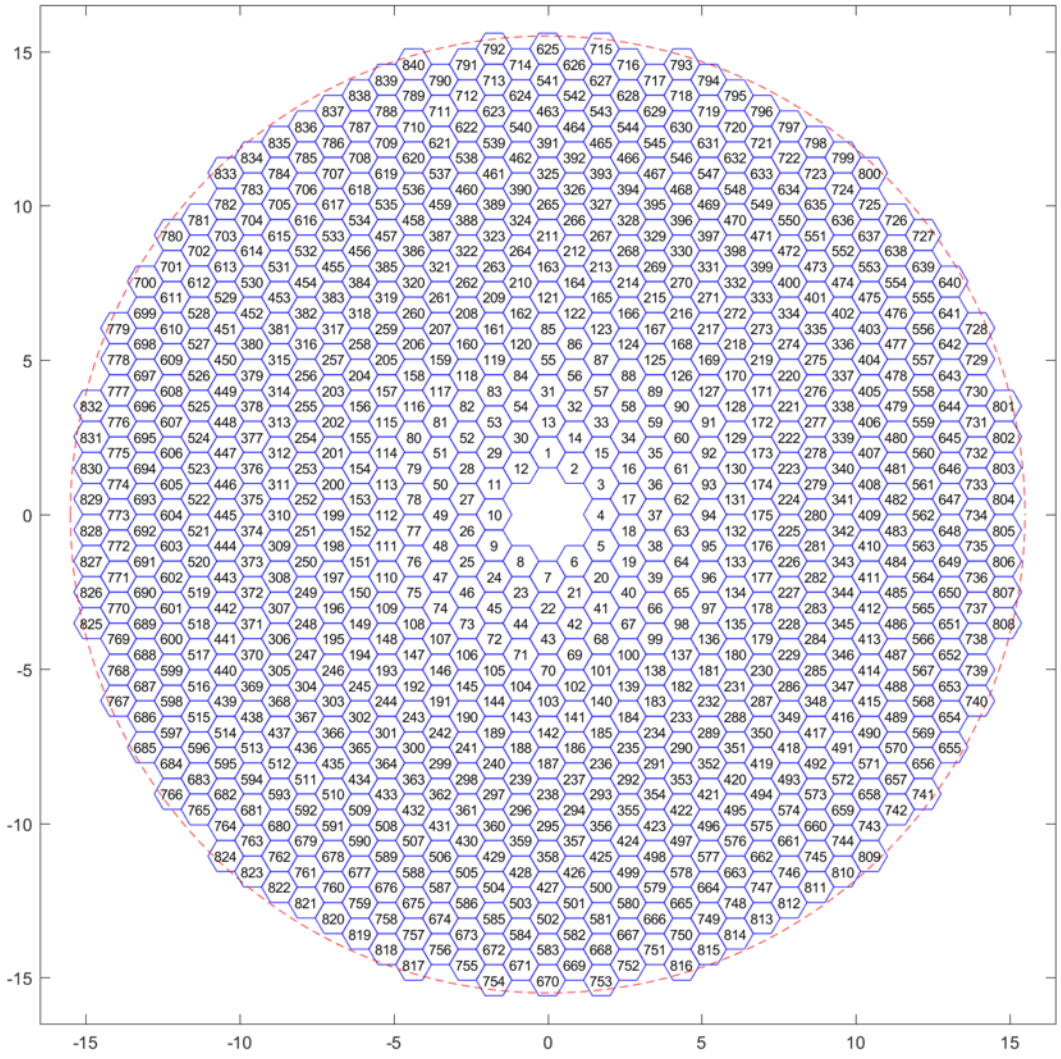

Figure 11: A scheme for segmentation and placement of individual mirrors on the primary assembly. Seven central mirror segments are missing (one exactly center and the surrounding ring of 6). A dotted red line shows the 31 meter diameter circle. Each mirror is numbered in a clockwise spiral pattern, ending at mirror 840. The size scale is in meters.

2.3 Mirror Modal Decomposition

While knowing the ideal shape of an individual segment is helpful, we must next attempt to recreate that shape. Because each segment could end up at any location within the primary, all mirrors must start identical. To transform the mirrors to the desired shape, we must first determine the differences between the stock shape, and the ideal one.

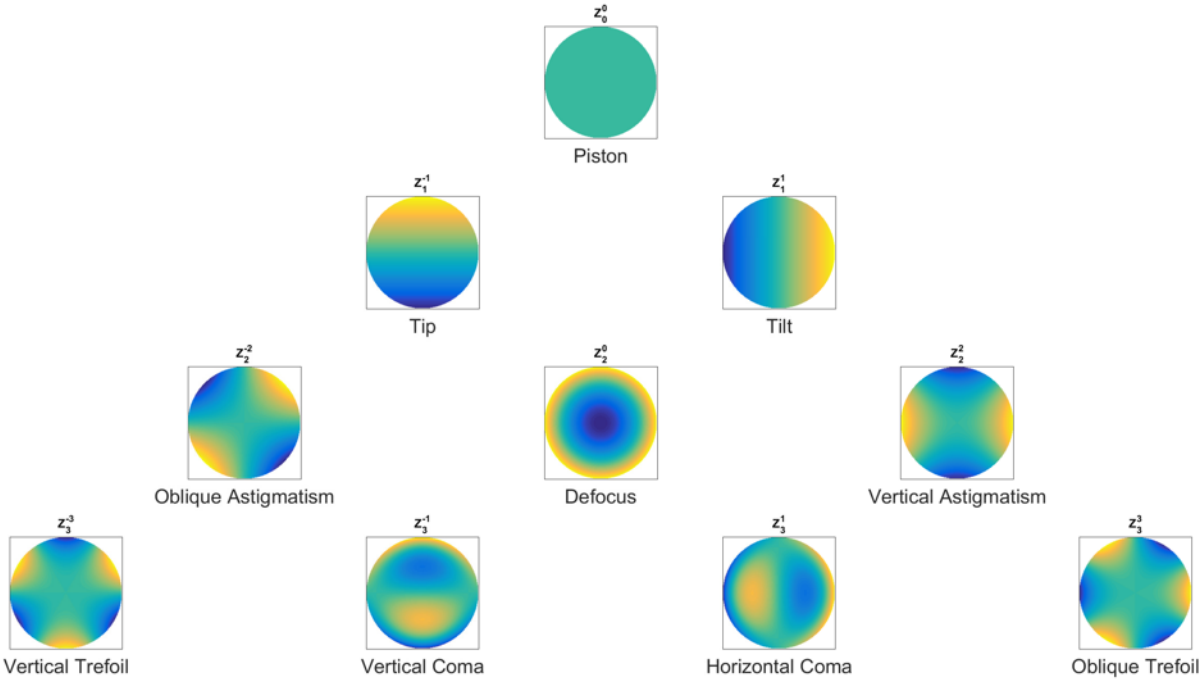

Figure 12: The first 10 Zernike modes. Each is a two dimensional polynomial orthogonal to the others, and in the domain of the unit circle.

To do so, we have decomposed each mirror into Zernike polynomials. The Zernike polynomials are a standard set of two-dimensional polynomials that form an orthogonal basis on the unit circle. We modified this to conform to a hexagonal domain by setting all terms for each polynomial that lie outside the hexagonal domain to 0. The Zernike polynomial are defined as

$$Z_n^m(\rho,\theta) = R_n^m(\rho)cos(m\theta)$$
$$Z_n^{-m}(\rho,\theta) = R_n^m(\rho)sin(m\theta)$$
$$R_n^m = \sum_{k=0}^{\frac{n-m}{2}} \frac{(-1)^k(n-k)!}{k!\left(\frac{n+m}{2}-k\right)!\left(\frac{n-m}{2}-k\right)!}\rho^{n-2k} \quad (8)$$

where ρ, θ are the polar coordinates defined on the unit circle, and n, m are non-negative integers. Each polynomial is normalized such that

$$\int_0^{2\pi}\int_0^1 Z_n^{m2}\rho d\rho d\theta = \pi. \quad (9)$$

The Zernike modes are visually represented (in their original circular domains) in Figure 12.

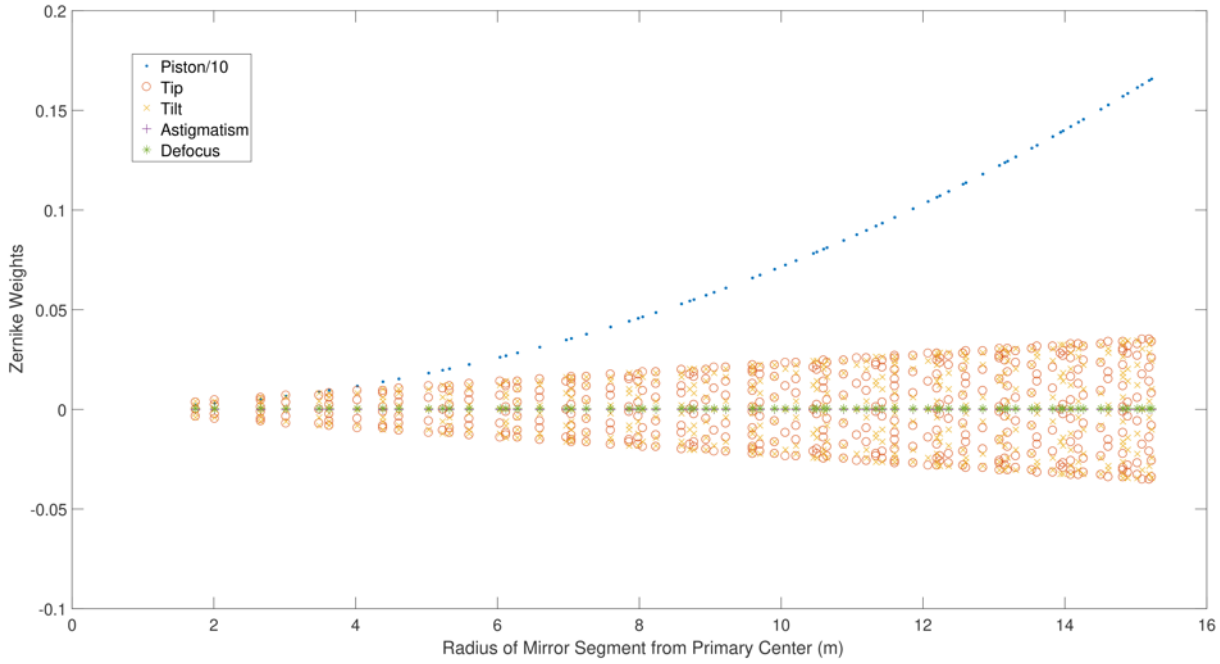

Figure 13: The weights of the Zernike modes for each mirror segment from Figure 11. As the distance of the mirror from the center of the assembly increases, the piston mode and maximum angle (tip and tilt) increase. These modes, along with defocus, have the highest impact on the mirror shape.

The shape of each mirror segment from Figure 11 was decomposed into the Zernike modes via least square fitting to the normalized polynomial functions. Figure 13 shows how the modal weights of the leading five modes (piston, tip/tilt, astigmatism, and defocus) vary with segment distance from the mirror center. The lowest order Zernike modes (piston, tip, tilt) can be easily removed with a Stewart platform, which provides 6 degrees of freedom, and is a well-established technology. Defocus is similarly straightforward to remove, using the same technology as JWST: a strut to induce curvature on a segment [22]. These four modes contain the vast majority of the shape information. Additionally, the defocus mode was found to not change significantly across all segments, as shown in Figure 14.

Since defocus is a purely symmetric, spherical change, applying a nominal curvature to all mirrors in polishing on the ground before launch is a feasible option. This severely reduces the requirements on any actuators to achieve this shape. Other Zernike modes are directional, and thus could not be manufactured in polishing without knowing the final location of each segment in the primary mirror.

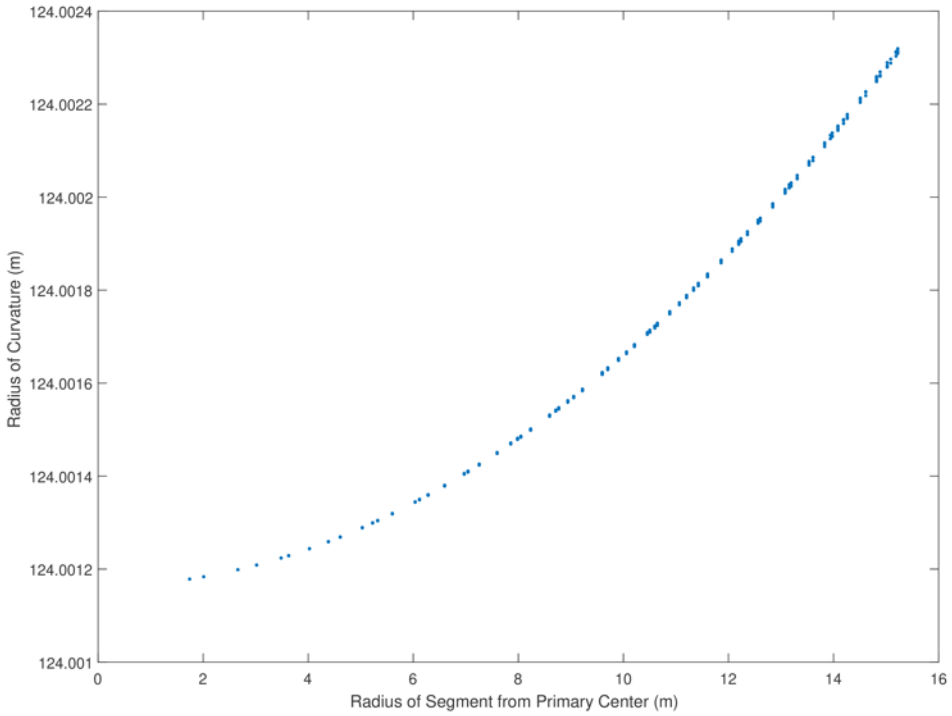

Figure 14: The radius of curvature for each mirror segment associated with the defocus mode. All are on the order of 124 m, and the difference between the largest and smallest curvatures is approximately 0.0011 m.

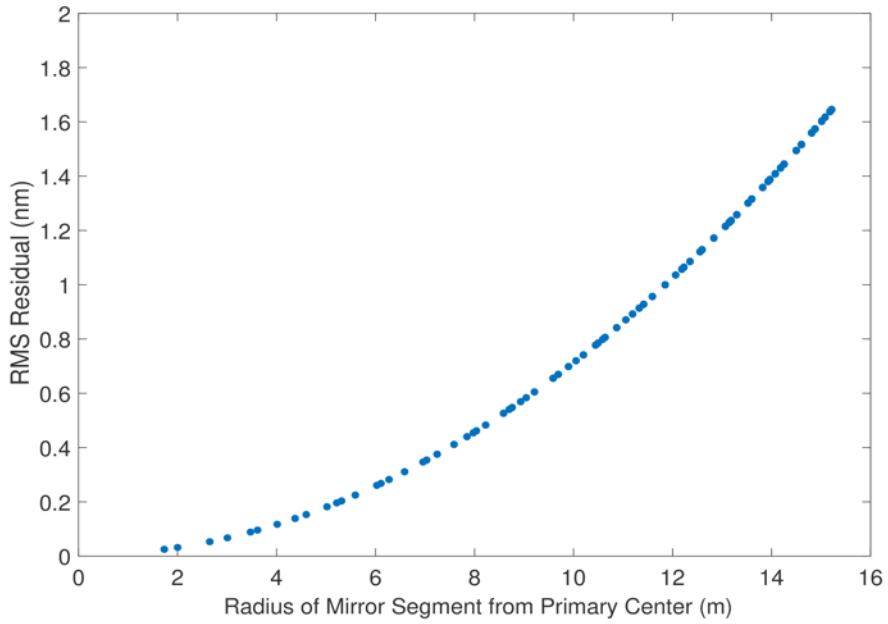

Figure 15: RMS of the residuals for each segment after reconstruction from the first 4 Zernike modes. There is a quadratic dependence of this error on the segment distance from the center of the primary. The maximum value does not exceed 2 nm.

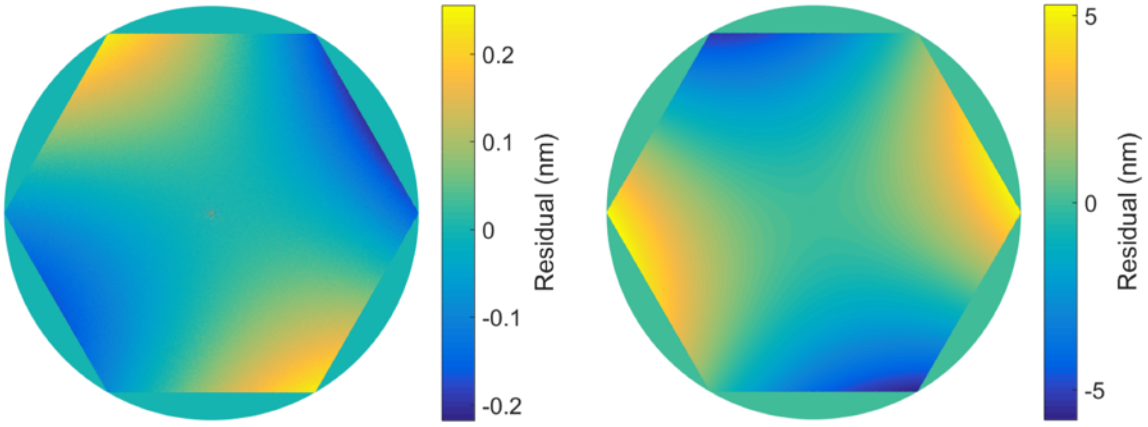

Figure 16: A comparison between the residuals of Mirror 16 (left) and Mirror 816 (right). Mirror 816 has residuals that peak at just over 5 nm, whereas Mirror 16 is as low as 0.25 nm. This is consistent and representative of their position relative to the center of the primary array. The pattern in both mirrors resemble astigmatism.

We subtract out the 4 leading Zernike modes from each segment shape and compute the root-mean-square (RMS) error (as compared with the ideal segment shape) of the reconstruction, shown in Figure 15, with a result of 2 nm RMS of error in the worst case. Figure 16 shows two illustrative examples of the residuals on individual mirrors. This includes both a low RMS error mirror and a high RMS error mirror. In both cases, the remaining error strongly resembles the next Zernike mode – astigmatism. This is expected, as astigmatism is the highest weighted mode that was not removed. This, and higher order modes will be set as required using additional actuators on the mirrors, as described below.

2.4 Analysis

The analysis of the mirror design was completed in Zemax Opticstudio. This software allows specifications of mirror shapes through radii of curvature and conic constants, Zernike weights, and many other methods, thus fitting our needs perfectly. It is capable of calculating diffraction effects, which is particularly relevant considering the gaps in the primary mirror (illustrated in Figure 17).

One of the key goals in this portion of the study was to quantify the effects of the gaps and segmentation compared to effects from reconstruction of the mirror shape. Therefore, we created two models: one with the ideal primary mirror shape, with the hexagonal geometry and gaps overlaid, and another model with each segment reconstructed based entirely on the first four Zernike weights for that mirror. Since each mirror segment in the primary is used in tandem, this had to be built in a non-sequential component of a mixed mode model.

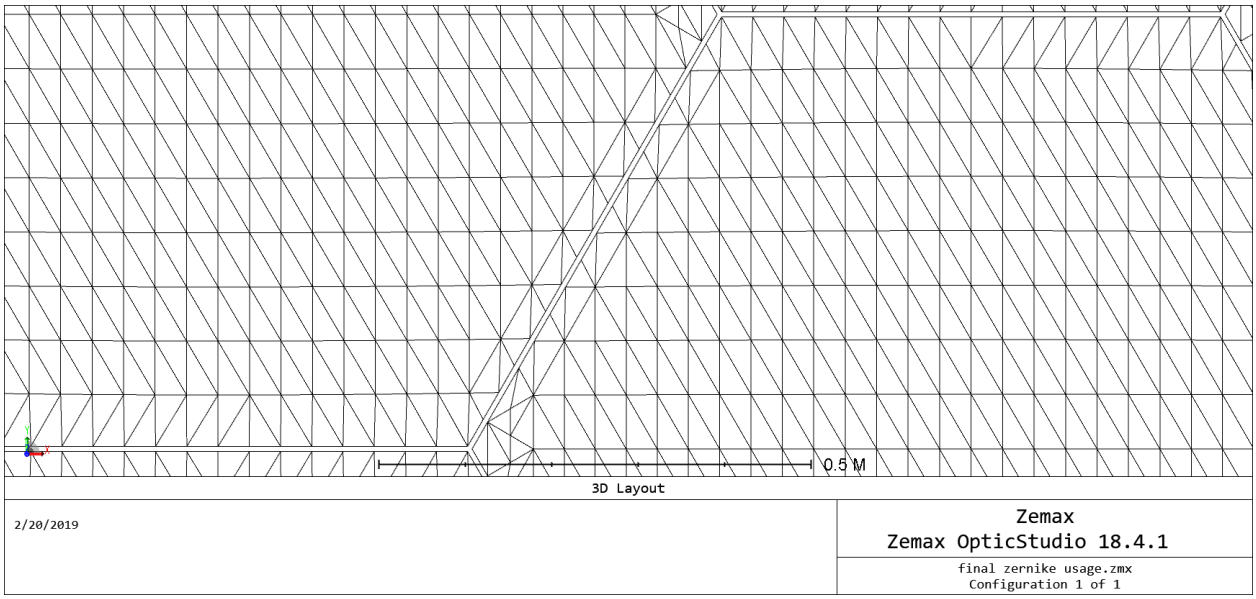

Figure 17: A zoomed in view of the Zemax OpticStudio model of the primary mirror assembly showing the 6 mm gaps between each mirror segment.

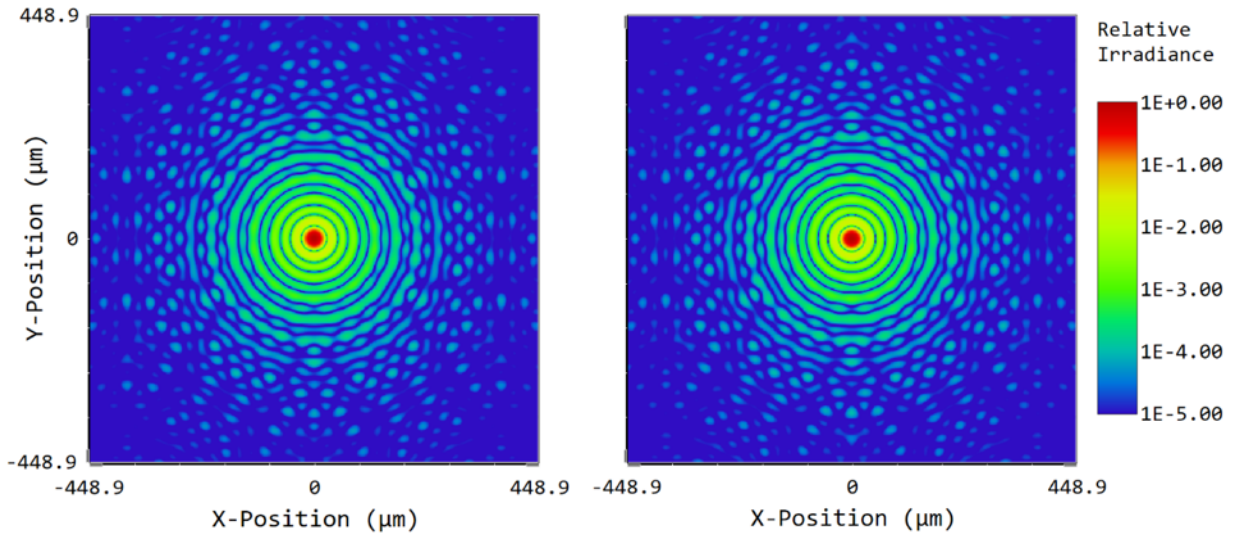

Figure 18: Simulated point spread functions of (left) the ideal primary mirror shape over-laid with the required segment gaps and (right) the reconstructed mirror shape of the true segmented primary, using only piston, tip, tilt and defocus modes for each segment. The reconstruction has a marginally lower Strehl ratio, but comparable wavefront quality to the ideal version, which can be further improved by direct control of higher-order Zernike modes.

The Huygens PSF, which accounts for diffraction in no-sequential components, was calculated in Zemax for both models, as shown in Figure 18, demonstrating excellent agreement. The ideal mirror, with gaps, represents the best possible PSF we can achieve for this setup. Improvements in the surface figure of each segment will trend the other model towards greater agreement with the

ideal model. In both models, the core PSF is very clearly visible, as is a hexagonal structure that arises from the segmentation.

In addition to the on-axis PSF we sought to characterize the segmentation effects on off-axis point sources, and so multiple fields were added at approximately 10 resolution elements away from the center of the image. The resulting spot diagram of all field points is shown in Figure 19.

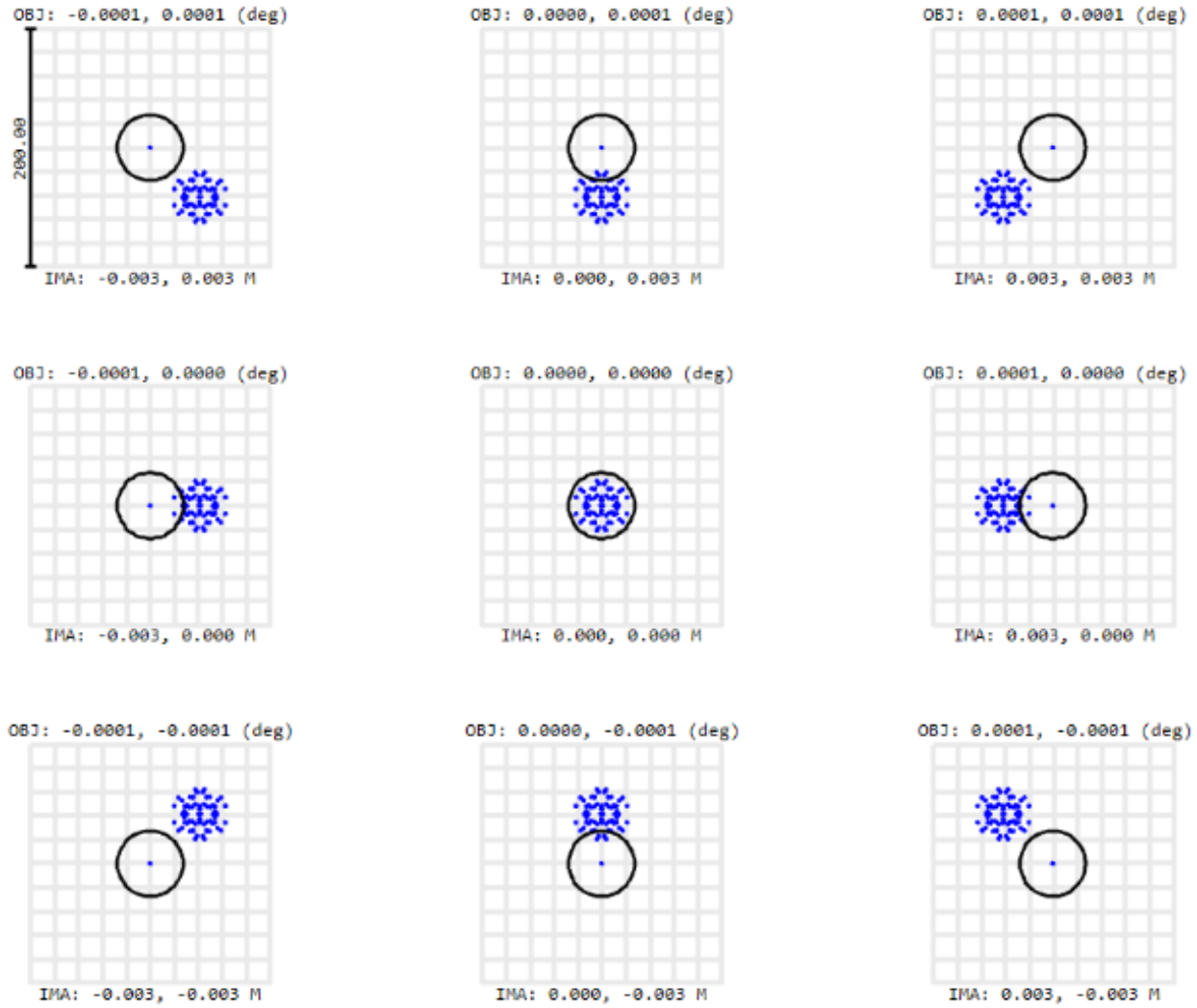

Figure 19: Spot diagram of the true, segmented primary model. This includes 1 axial field, and 8 other fields offset by approximately 10 $\frac{\lambda}{d}$*. The dark circle in each field is the size of one resolution element. In each case, the diffraction of the spot is approximately the size of the circle. Off-axis fields have a slight displacement towards the center of the image plane compared to their true location.*

These results indicate that simply using a Stewart platform for piston, tip, and tilt for each mirror, coupled with a mirror-ground curvature and curvature strut will sufficiently meet the needs

of the optical design for this telescope in ideal situations. Actuators and active control will still be necessary for distortions in the mirrors and to correct for mid-spatial frequency wavefront errors.

2.5 Mirror Deformation Analysis

The ideal mirror design and subsequent analysis in sections 2.1-2.4 prescribes and assumes the desired mirror surface figure for each individual mirror segment. In order to ensure segments can rendezvous and dock in any order or position, each module must be capable of achieving the desired shape of any of the segments in Figure 11.

While a complete design of the mirror actuation control system is deferred to future work, in Phase I, we sought to develop a complete tool set for carrying out detailed mirror deformation analyses. Here we present initial mirror deformation analyses which sought to discover the smallest possible mirror RMS error (between the structurally modeled mirror surface figure and the desired surface figure) that can be achieved using independent linear actuation under various assumptions. It is important to note that this application requires direct control of low spatial frequency modes – a generalization of the curvature strut in the JWST mirrors, as well as additional independent linear actuation. The tools we have developed and refined by testing on independent actuators will allow us to fully develop mirror models with both types of actuation in the future. For these analyses, we select materials and mirror design similar to those of the JWST segments due to the prior investments in, and current maturity of, those technologies.

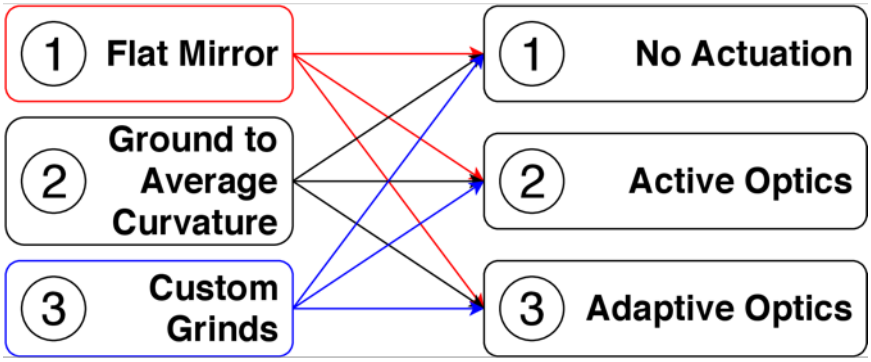

Figure 20: A graph depicting mirror grind and actuation options.

In general, there are three nominal mirror structural model mirror surfaces we could consider. The first is a flat mirror, which is the simplest to model for a structural analysis. Milling the JWST mirror-substrate and grinding the optical surface induce residual stresses in the mirror structure so reducing the amount of material removal can reduce these induced stresses. The second is a mirror ground to the average curvature of all segments which retains the radially symmetric properties of the flat mirror, thereby still allowing for a randomized assembly order. The third option is a mirror ground specifically for the intended position of each segment. Customizing each mirror vastly increases scheduling complexity for ordering of individualized manufacturing, launch, and rendezvous making this option generally undesirable. These options are graphically shown in the first column of Figure 20.

Assuming low areal density mirrors (such as those used for JWST) requires mechanisms for correcting mirror misalignments caused during launch or docking, deforming a nominal mirror into its position-determined shape, correcting for off-nominal thermal distortions, and positioning mirrors into their coarse position as a part of the primary mirror. After docking the module, a

Stewart platform will be used to re-position the mirror into its primary mirror coarse position, effectively subtracting the piston, tip, and tilt modes of the mirror. There are three options for controlling higher order Zernike modes of the mirror segment shapes. The first is no actuation, relying upon the surface figure of the mirror alone to achieve the desired surface figure. The second is active optics, which could include up to 127 individual actuators per segment. The third is adaptive optics intended to continually deform the mirror, controlling higher frequency deformations. These options are shown in the right column of Figure 20.

Table 2: Enumeration of Mirror/Actuation Combinations and Rationale

#	**Mirror Grind**	**Actuation Type**	**Studied** (Y/N)	**Rationale**
1	FlatMirror	No Actuation	N	Preliminary optical analysis eliminates this option
2	Flat Mirror	Active Optics	Y	Actuators with extensive testing for this exist, JWST will provide heritage for on orbit segment co-phasing
3	Flat Mirror	Adaptive Optics	N	High energy cost for operation
4	Ground to Average Curvature	No Actuation	N	On-List for Analysis
5	Ground to Average Curvature	Active Optics	N	On-List for Analysis
6	Ground to Average Curvature	Adaptive Optics	N	High energy cost for operation
7	Custom Grinds	---	N	Uncertainty in sail delivery times and requires ordered docking

The small graph in Figure 20 displays the possible combinations of default mirror surface figures and mirror deformation mechanisms and is reiterated in a full tradespace enumeration in Table 2, showing what was investigated and the supporting rationale. The optical analysis in section 2.1 shows mirrors in Option 2 and Option 3 combined with no-actuation are capable of meeting root-mean square error (RMSE) of the desired to actual surface figure to within 2nm, under the assumption of no polishing or other errors. We adopt the suggested 6nm rms surface figure error requirement for a 'visible spectrum' JWST mirror segment [23].

This indicates structural analysis is necessary for Options 1 and 2 mirrors and any combination of actuators should ideally improve the surface figure further. The Option 1 flat mirror combined with No-actuation does not meet RMSE requirements so we are motivated to explore active optics actuation schemes. While beyond the scope of the originally proposed Phase I work, the positive results from the optical analyses motivated us to start the development of tools that would allow us to fully analyze the mechanical deformations required to impart the desired shapes on identically polished mirror segments.

The following subsections discuss how we model the mirror (section 2.5.1), our RMSE minimization using commanded node-displacements for various actuator configurations (section 2.5.5), and RMSE minimization by optimizing mirror forces (section 2.5.6).

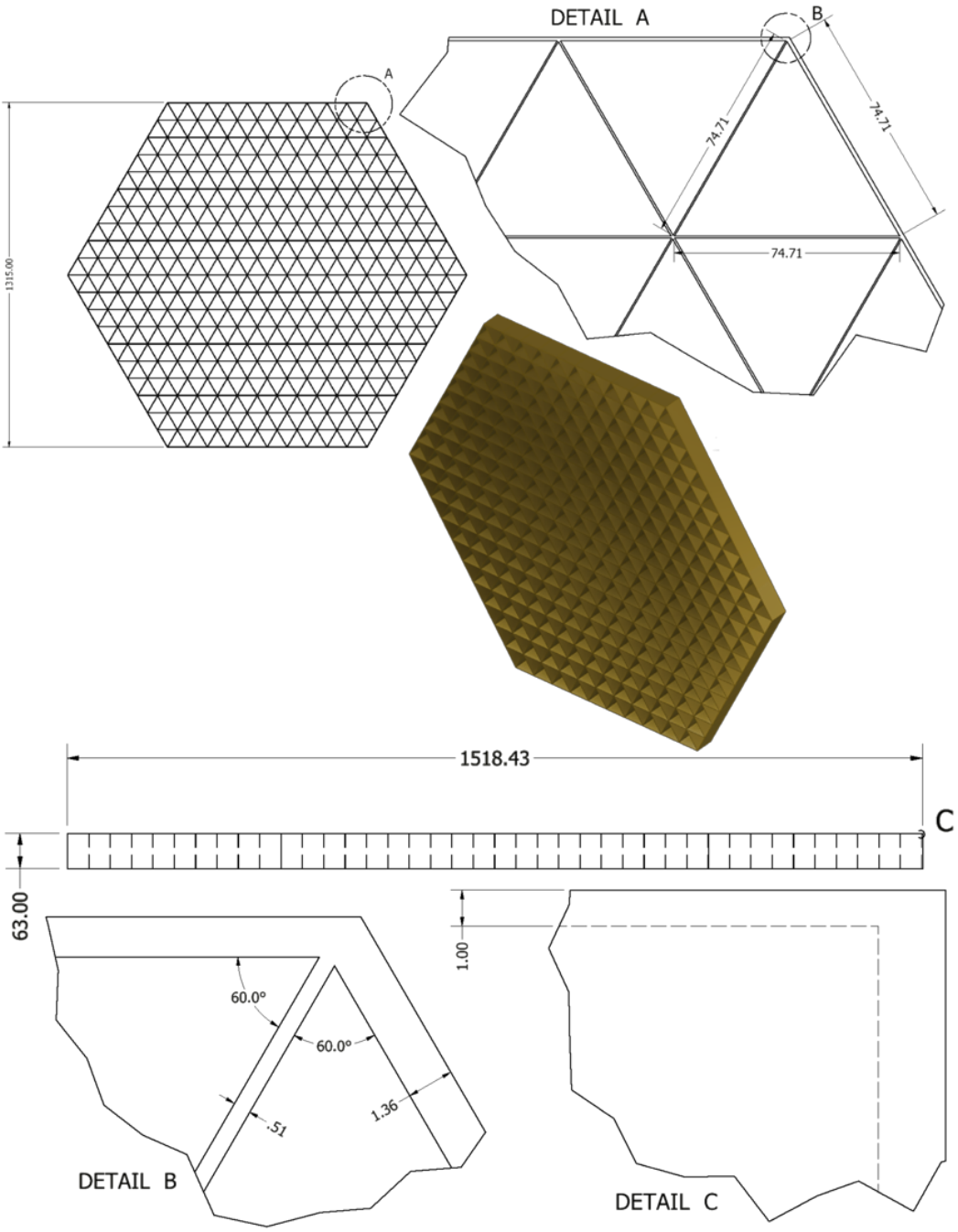

Figure 21: 1.315 m flat-to-flat hexagonal module mirror CAD model dimensioned in the likeness of a JWST mirror segment, backplane view with 'A' section noted (top left), 'A' section view of black plane indicating triangle isogrid dimensions and 'B' section noted (top right), isometric view of back side (center), mirror side view also showing 'C' section (bottom center), 'B' section showing further isogrid design details like 0.51mm rib thickness (bottom left), 'C' section showing mirror shell thickness of 1mm (bottom right). All units in mm or degrees. The JWST mirror has 271 backplane rib intersections, 870 ribs, and 600 triangles.

2.5.1 Mirror Modeling

We reverse engineered our original mirror model using a combination of dimensions taken from JWST segments in Ref. [24], personal conversations with Phil Stahl conveying a select few dimensions, and relaxing dimensions to achieve geometric constraints. The result is the mirror CAD model depicted in Figure 21. Omitted from this CAD model are fillets at rib intersections on the backplane as well as Wiffle Plate attachment holes. The real version of this mirror would be machined from a solid billet of beryllium where one side is machined into the isogrid pattern in our CAD file with added fillets and mounting holes to avoid stress concentration and the other side ground to whichever specification in Table 2 we choose.

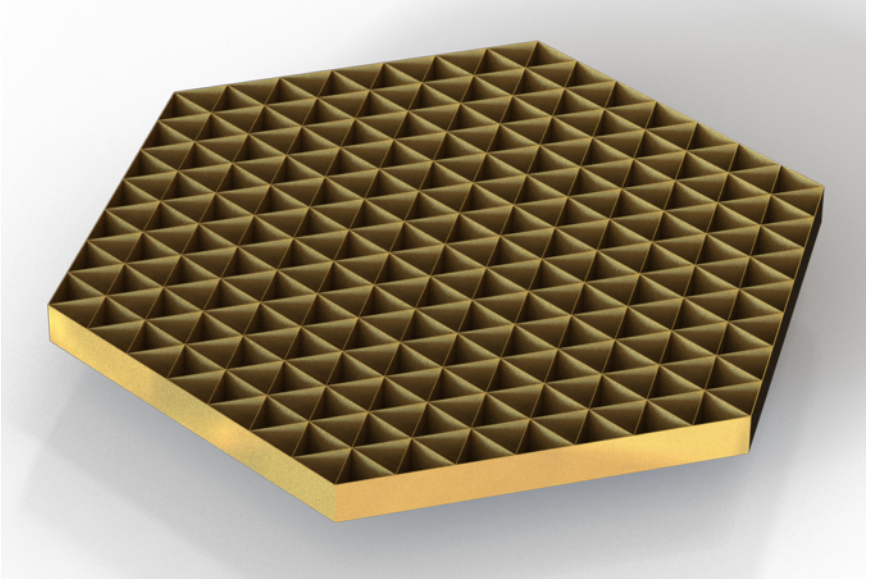

Figure 22: 1 m mirror segment model.

The nominal module mirror design in the optical system design from section 2.1 uses a 1m flat-to-flat mirror. We created a 1m flat-to-flat mirror based on the medium fidelity model (Figure 21). The triangular ribs were modeled with a thickness of 0.5 mm, while the mirror surface and outer edge of the mirror had 1.0 mm thicknesses. In reducing the size of the mirror, the number of triangles per edge was decreased from 10 to 7, however, we did not decrease the mirror thickness of 63.0 mm. An image of the 1m mirror segment model is shown in Figure 22 with drawing dimensions in Figure 23.

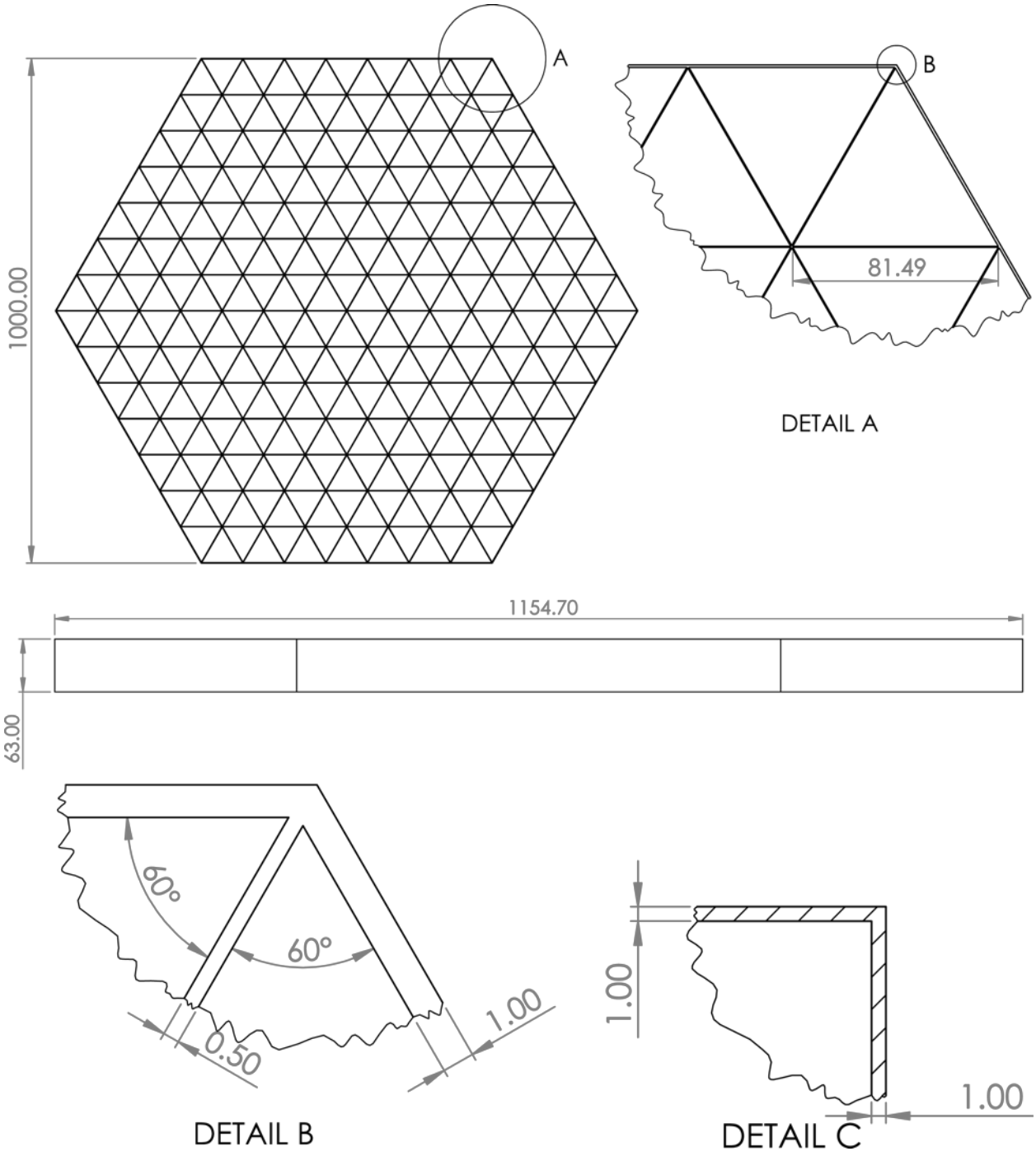

Figure 23: 1 m Flat-to-Flat mirror CAD model showing bottom view with flat-to-flat dimensions and 'A' section location (top left), 'A' section showing triangle side length and 'B' section location (top right), mirror side view showing mirror corner-to-corner dimension and thickness with 'C' section being top right corner of this view (center), 'B' section view showing triangle corner angles, rib thickness, and outer edge thickness (bottom left), 'C' section showing assumed top surface thickness (bottom right).

2.5.2 Mirror Material

We selected beryllium as our mirror material of choice as a result of the Advanced Mirror Demonstrator Program (AMDP) result and Mirror Recommendation Board conclusions. The AMDP funded a trade study comparing Kodak/Corning manufactured ULE® Glass and Ball Aerospace/Brush-Wellman/AXSYS/Tinsley manufactured Beryllium mirror. In the conference proceedings of Ref. [25]:

> Beryllium was rated as the highest performing, lowest technical risk solution for the JWST cryogenic application. Its cited strengths included superior cryogenic CTE and thermal conductivity; significant margins on thermal performance, stiffness and mass; and its excellent potential science performance. Specific concerns included managing surface stress to achieve convergence to the required final surface figure and manufacturing schedule.

The manufacturing timeline is also a critical factor in our material selection in order to address schedule constraints experienced in JWST and Hubble [20]. JWST segment manufacturing times from Ref. [26] indicate each mirror takes ≈3mo to manufacture. If the telescope requires 840 mirrors manufactured within 7 years at 3 months per mirror, a single production line could produce 28 mirrors ($7yr \times 12\ \frac{mo}{yr} / 3\ \frac{mo}{mirror} = 29 mirror$). We would require a minimum of 29 production lines ($29 \times 29 = 841$) to achieve our goal of launching within 7 years. This could be mitigated by the reduction in manufacturing time of the mirror by removing time intensive steps in the process [24]. Of course, we expect that the learning curve (Figure 4) will decrease the manufacturing times for latter segments, but we have chosen to go with a conservative estimate to ensure mission viability.

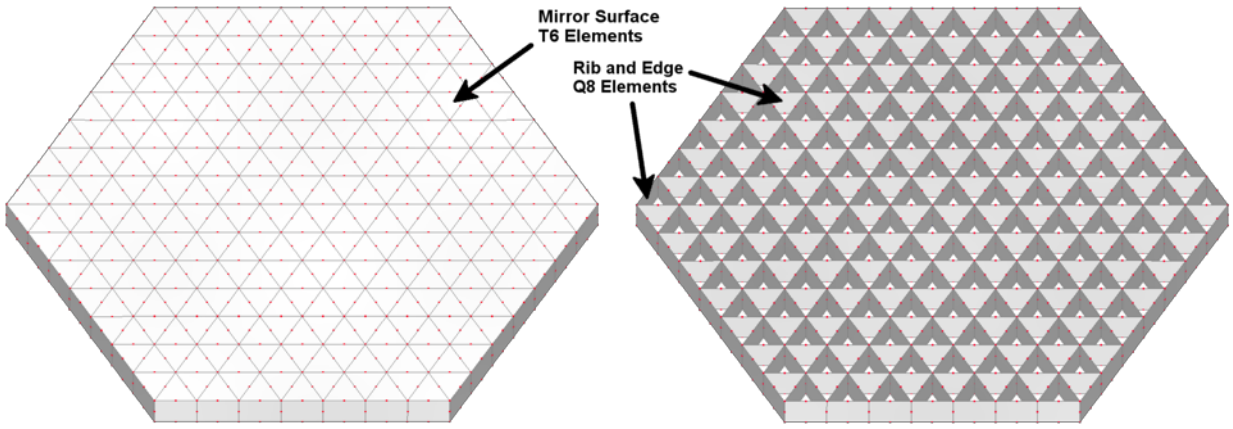

Figure 24: FEMAP generated mesh with top surface type T6 elements with 1mm thickness and edge/rib elements of type Q8 elements where edge elements have thickness 1mm and rib elements have thickness 0.5mm. This mesh contains 756 elements with 1431 nodes. Red dots indicate nodes.

In our finite element models, we make use of material properties for beryllium from Refs. [27, 28, 29, 30, 31, 32], which are outlined in Table 3. Each of the elements in Figure 24 were assigned these assumed properties. We note these properties represent a nominal value for use in this

analysis and could vary by more than 10% from nominal. The actual deformations in this report should be considered representative of a nominal mirror design but not necessarily equal to the actual deformations.

Table 3: Beryllium material properties [27]

Property	**SI**	**Imperial**
Tensile strength	370 MPa	53700 psi
Yield strength	240 MPa	34800 psi
Elastic modulus	303 GPa	43900 ksi
Poisson's ratio	0.0700 - 0.180	0.0700 - 0.180
Elongation at break	3%	3%
Charpy impact	1.50-5.50 J	1.11-4.06 ft-lb
Hardness, Rockwell B (converted from Brinell hardness)	75 - 85	75 - 85

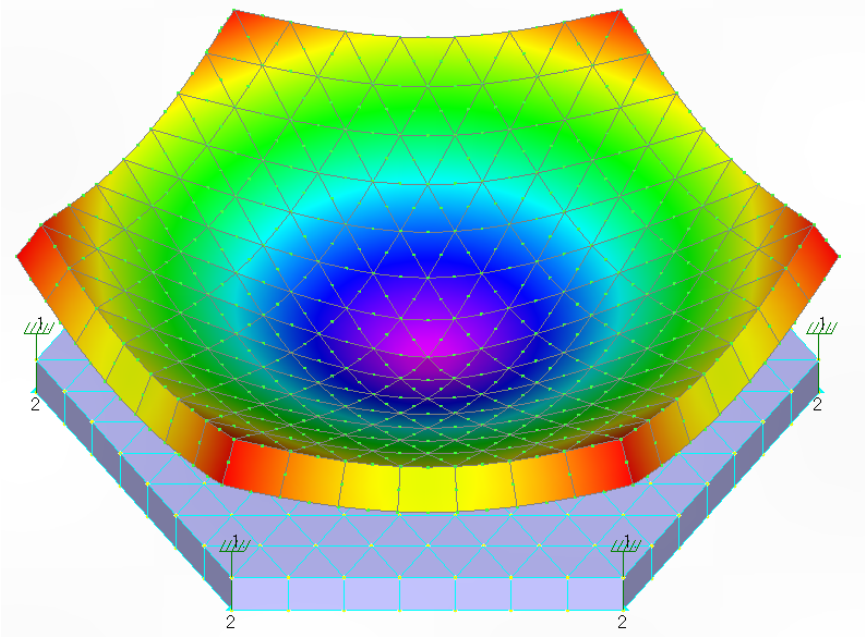

Figure 25: Example deformed shape of mirror (deformations are not to scale but exaggerated for visibility)

2.5.3 Structural Finite Element Model

We created a structural finite element (FE) model, using FEMAP, a commercial analysis program created by Siemens PLM. The model was used to quantify surface figure errors between an ideal mirror shape and deformed mirror shape for specific modules with different actuation and actuator configuration schemes. First, we imported the mirror CAD model from Figure 23 into FEMAP and used the midsurface tool to convert the 3D model into a collection of 2D surfaces. We then combined the collection of 2D surfaces with a non-manifold add process and subsequently applied surface meshes. There are two types of elements used in our mesh: a T6 type element on the mirror surface and Q8 type element along the outer edges and ribs, as shown in Figure 24. Our use of

second order elements allows a high level of accuracy with a lower node count. This enables us to solve the structural model on a machine with 16GM of ram in less than 1 second. This further enables us to use this model for optimization, where optimized values would be validated against a higher resolution mesh with a substantially longer solve time. A sample deformed shape of the mirror is shown in Figure 25.

2.5.4 Actuator Mounting Locations

For isogrid structures in general, actuators and other attachments are mounted at rib intersections. We use Ball Aerospace's cryogenic actuators as a nominal reference implementation. Given an estimate for the size of a cryo-actuator based on those of JWST, we can show that actuators can be arranged in orientations alternating in 60° angles to allow actuators to be placed at each rib intersection point if desired, as shown in Figure 26.

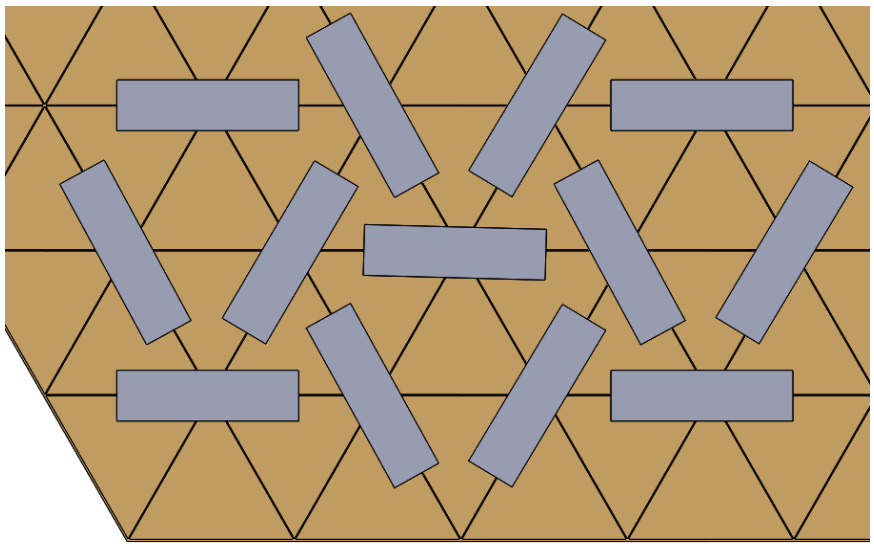

Figure 26: Fitting of actuators showing actuators can be fitted to every rib intersection.

Using an approach that is generalized to any mirror mesh model, we are capable of isolating backplane nodes where loads can be applied. This process results in the set of mesh grid IDs associated with each grid point x,y,z location shown in Figure 27.

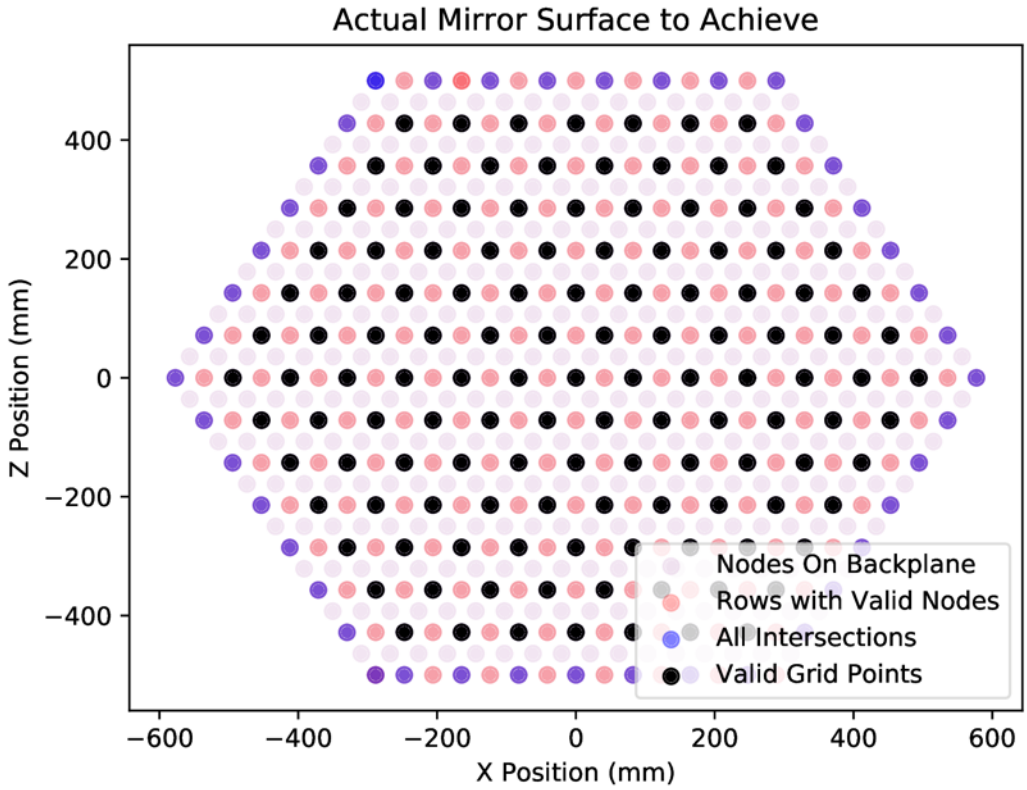

Figure 27: A plot showing valid force application locations based on the requirement that forces can only be applied at rib intersection nodes and not along edges

2.5.5 Enforced Deformation Analysis

For each actuator configuration, the tip, tilt, and piston were removed from the optimal mirror shape, and remote displacements were applied at the location of the actuators to match the nominal mirror shape. The simulation was run and the model generated the deformed shape of the mirror. The deformed coordinates of the mirror surface nodes were extracted to calculate an RMS error of the mirror. However, because the points on the mirror translate in the XY plane in addition to Z-axis displacement, the applied remote displacement no longer matches the nominal Z displacement at the (X,Y) position. As a result, the simulation is iterated using the new (X,Y) position until the correct applied displacement is determined. An error plot of a 19 actuator configuration is shown in Figure 28. The displacement error is found by subtracting the nodal Z displacement of the top surface from the nominal mirror displacement.

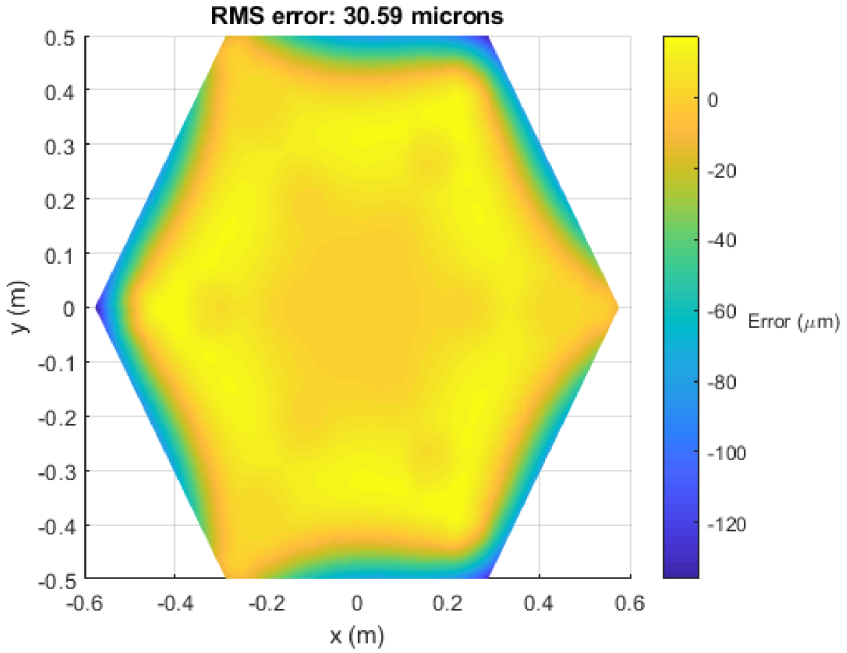

Figure 28: Error plot of 19 actuator configuration

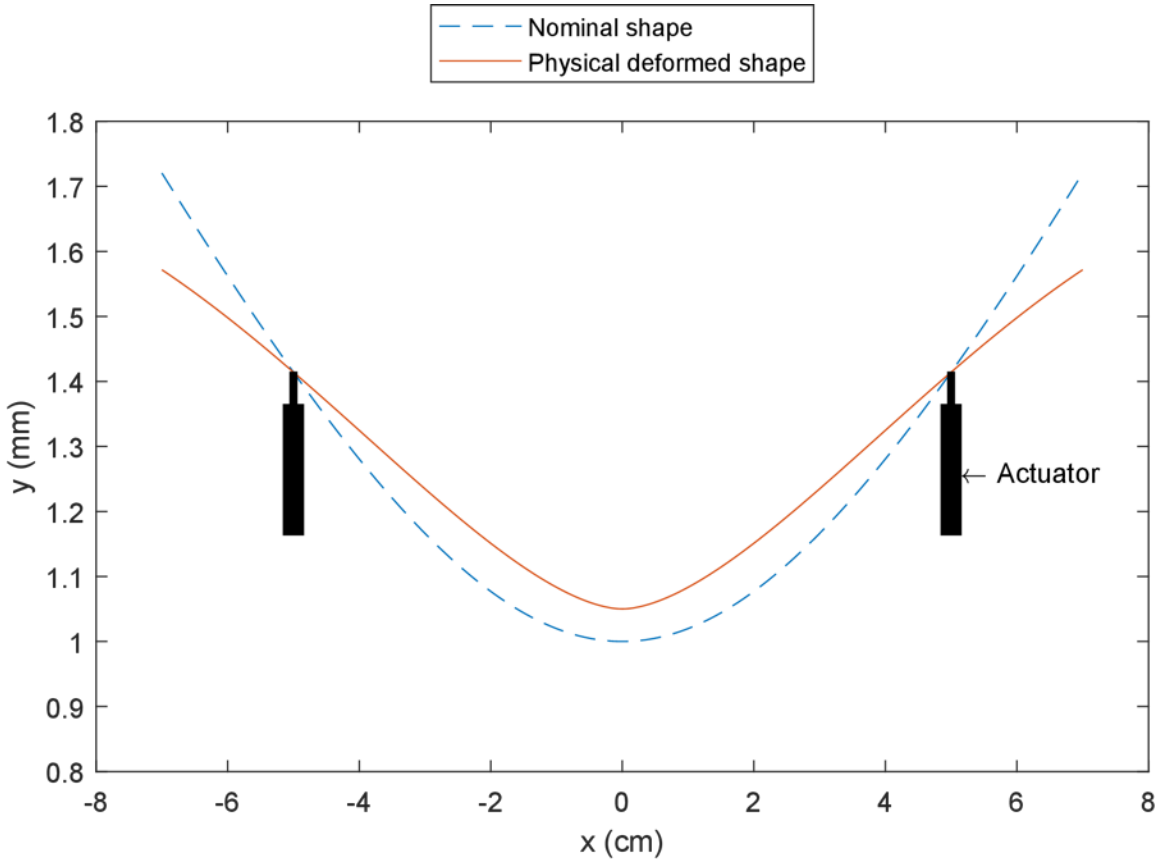

Figure 29: Illustration of error between actuators

Multiple actuator configurations using varying numbers of actuators were tested with actuators spaced symmetrically and evenly across the surface. As expected, the error plots indicate that the error is 0 at the location of the actuator, but between actuators the surface deviates from the nominal shape – the nominal shape of the mirror is a hyperbolic, which generally will not be the shape of a plate when deflected at discrete points. This effect is illustrated in a two-dimensional example in Figure 29. As a result, while the error is 0 locally at the actuator point, surface error still exists which is largely a function of actuator spacing. As actuator count increases and spacing between actuators decreases, the surface error of the mirror will similarly decrease.

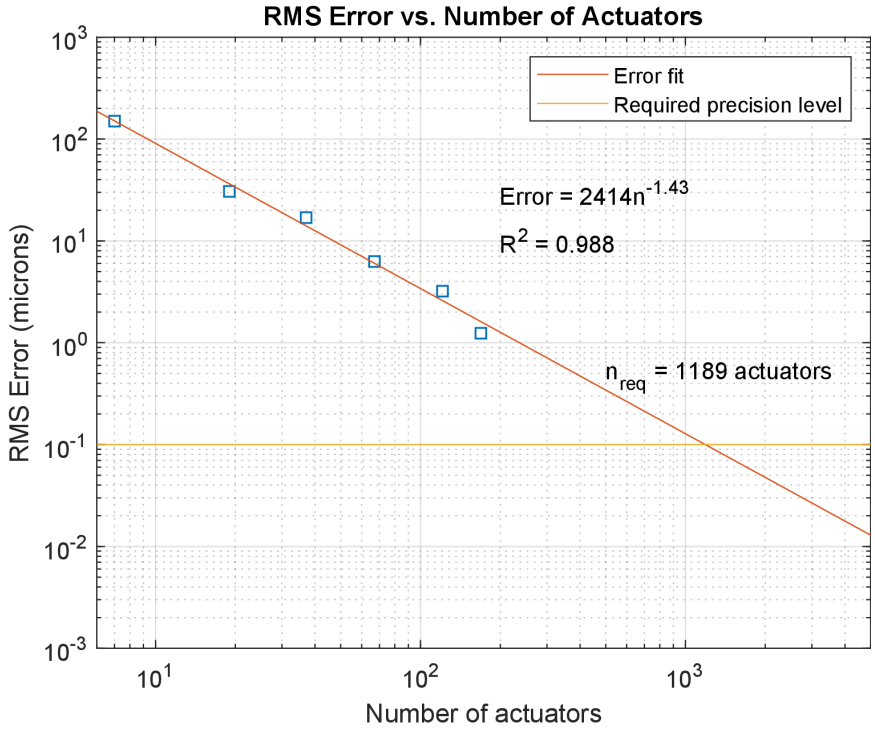

Figure 30: Plot of RMS error vs. number of actuators with power regression fit.

Figure 30 shows a log-log plot with RMS error plotted against the number of actuators. As expected, the error decreases as the actuator count decreases. A power regression fits the data well, showing that the error decreases proportionately with $n^{-1.4}$. Also plotted is the RMS error level of 10 nm, which is approximately the surface figure required. From extrapolating the plot, we see that on the order of 1000 actuators would be required to achieve 10 nm RMS error with solely this method of actuation. These actuators would also require nm precision and travel ranges up to 1-2 mm. Currently the only such cryoactuators that we are aware of are the JWST cryoactuators, which are too large and heavy to be a viable option [33].

Our analysis has some limitations. We only locally optimized the actuator displacements, which resulted in zero error at the actuator position and large error in between actuators. It is possible that the global error can be reduced by doing a general optimization. In addition, we used a relatively low fidelity structural model. These limitations would likely change the error results slightly, but the trend displayed is still valid. We have shown that to deform the flat mirror via independent linear actuators to a nominal shape to the required 10 nm RMS error will require an unfeasible number of actuators. This clearly points to the need to directly control low spatial

frequency modes – in other words replicating and generalizing the curvature strut of the JWST mirrors.

The modeling tools developed here will prove invaluable in the development and analysis of the required low-spatial frequency mirror control mechanisms. One key finding of this work is that the radius of curvature (ROC) of mirror segments varies very little over the telescope radius. The ROC at the center and edge is 124.0023m and 124.0012m respectively. As a result, each mirror segment can be manufactured with a mean ROC and still achieve optical requirements. By making all segments exactly identical to one other, the cost of manufacturing can be reduced in comparison with other segmented mirror designs. In addition, because of the large number of segments, the learning curve of producing identical segments will result in large cost savings over time.

2.5.6 Force Optimization Analysis

There are three main issues with the approach of applying deformation at individual nodes of our mirror model. The first is the ability to specify infeasible surface deformations: the actuators specified in section 2.5.4 could exceed the maximum actuator force (F_{max}). The second issue is a difference between backplane node deformation (where the deformations are applied) and mirror surface node deformations (where we calculate error). The third is the accounting of error for non-actuated nodes. The only mesh nodes that can support the mounting of actuators are the rib intersection nodes. However, the mesh surface has nodes located on the mirror surface at midpoints between rib-intersection nodes, which are used in the calculation of error. These midpoint nodes cause higher spatial frequency errors which the enforced deformation cannot accommodate for without a minimization-optimization process. To address these issues, we developed a force optimization process on the mirror to determine the optimal forces each actuator should apply to minimize the surface figure error between the desired mirror shape and the actual deformed mirror shape.

The FEMAP mirror mesh is originally specified with mirror top-surface in the -Y direction, a corner in the +X direction, and a mirror flat in the +Z direction with force vectors applied in the -Y direction on backplane nodes. Let us call this coordinate system O_{FE}. Our optimization process is set up to accept input of meshes with the aforementioned general form, which allows us to input different meshes and mirror sizes.

In order to apply forces to the mirror, we need to isolate the nodes where forces can be applied, namely rib intersection nodes that do not lie along the mirror edge. The mirror nodes can easily be broken down into 3 classifications based on their bulk Y position, y≈62mm are all backplane nodes ($\mathbf{N}_{bp}$), y≈30mm are midpoint nodes of ribs positioned between the backplane and mirror surface, and finally mirror surface nodes ($\mathbf{N}_{s}$) at y≈0mm. We generalize this node subset classification as

$$\mathbf{N}_{bp} = \{i | i \in \mathbf{N} \text{ and } y_i > \min(\mathbf{y}) + 0.95 \times (\max(\mathbf{y}) - \min(\mathbf{y}))\}, \quad (10)$$

where **y** is the array of node y values corresponding to each node in **N**, **N** is the set of all nodes in the mesh, and we assigned 0.95 as a reasonable cutting plane value to isolate the backplane nodes. We then leverage the geometry of the backplane nodes by incrementally binning the nodes of $\mathbf{N}_{bp}$ by Z values (saved as a set of G_z where $G_z \subseteq$ Z) that are near each other. We make use of a notation **G** δ **H**≡**G** is near **H** for generic sets **G** and **H** where δ describes the maximal distance between an item in **G** and **H**. By iterating over each node's z value (z_i), we either add the current node index,

i, to the set of indices associated with z_i ($\mathbf{I}_{z_i}$) or, if there are no existing nearby bins, create a new bin of G_z and add add *i* to $\mathbf{I}_{z_i}$. We then turn our set G_z into an ordered set sorted by ascending and keep track of indexing using a surjective, *f*, which is used to map the set of indices associated with G_z to their new set $\mathbf{I}_z$'. We then keep node indices from every other even indexed z grid resulting in $\mathbf{N}_{\mathbf{bp,odd\ z}}$.

Figure 31: Algorithm: Extracting subset of nodes containing z component on even grid index.

Algorithm 1: Extracting subset of nodes containing z component on even grid index

Result: $\mathbf{N}_{\mathbf{bp,odd\ z}}$, the set of nodes in rows with odd indices of Z groupings

$\mathbf{N}_{bp}$, $\mathbf{z}$, $\delta \Leftarrow$2mm

$\mathbf{I}_{z_i} \Leftarrow \{i \in \mathbf{N}_{bp}\}$ // assign random backplane node

$G_z \Leftarrow \{z_i | i \in \mathbf{N}_{bp}, i \in \mathbf{I}_{z_i}\}$ // create initial set of 'Z' values

for $i \in \mathbf{N}_{bp} | i \notin \mathbf{I}_{z_j},\ \forall\ j \in \mathbf{N}_{bp}$ **do**

  // iterate over backplane nodes not assigned to a G_z value

  if $\{z_i\}\boldsymbol{\delta}\ G_z$ **then**

    // if z value is near z value in G_z

    $\mathbf{I}_{z_i} \cup \{i\}$ // add node index to list of nodes associated with z_i

  else

    $G_z \cup \{z_i\}$ // add new z to collection of z values

    $\mathbf{I}_{z_i} \cup \{i\}$ // add node index to list of nodes associated with z_i

  end

end

$G'_z \Leftarrow \mathrm{sort}(G_z)$ // sort by ascending Z values

$f : G_z \longmapsto G'_z$ // surjective f maps G_z to G'_z

$\mathbf{I}'_z \Leftarrow f(\mathbf{I}_z)$ // remap Z value indices

$G'_z \Leftarrow \{G'_{z,(2i-1)}\ \forall\ i \in \{1..\ \lfloor |G'_z|/2 \rfloor\}\}$ // keep every odd G'_z value

$\mathbf{N}_{bp,odd\ z} \Leftarrow \{I'_{z_{(2i-1)}}\ \forall\ i \in \{1..\ \lfloor |G'_z|/2 \rfloor\}\}$

The set of nodes resulting from the algorithm shown in Figure 31 are shown as red dots in Figure 27. We duplicate this process for each row of nodes in $\mathbf{N}_{bp,odd\ z}$ where we sort nodes in a valid z row by their x value and keep every odd indexed node. Our final down selection is to filter nodes along the edges by defining a hexagonal region with corners slightly smaller than the backplane corner nodes. This gives us the grid IDs of the back nodes ($N_{bp,Fnodes}$) in Figure 27. For the sake of this analysis, we assume every backplane node has an actuator attached to it.

We make use of the mesh model generated using FEMAP and an open source project called pyNASTRAN[1], which allows us to load a template mesh model and then add or subtract forces and displacement constraints as well write this new object to a NASTRAN instruction file used as an input when we use Python to run the NASTRAN file. We initially strip the input file of all

[1] https://pynastran-git.readthedocs.io/en/latest/

displacement constraints and applied forces, and then reapply a displacement constraint on the mirror center node to its nominal x,y,z position on the desired mirror surface as well as its rx,ry,rz displacement. This acts as our input seed to the optimization process along with a vector of 0's for each Zernike mode used.

There are multiple ways to formulate the force inputs to the FE model. Initially, we applied forces at each node with individual amplitudes which resulted in 127 + 6 degrees of freedom in the optimization process. This repeatedly resulted in forces at adjacent nodes being drive to their force limits and either long solution times (~ 3 days) or no optimized solution. To reduce the number of degrees of freedom, we implemented force amplitudes based on Zernike polynomials discussed in section 2.3 in Eq. 8. We assign a force amplitude (F_j) to a given node, index by j, using

$$F_j = \sum_{i \in M} P_i \times Z_n^m(\rho, \varphi), \forall\ j \in N_{bp,Fnodes}. \tag{11}$$

Where M is the set of n, m combinations fed into the Zernike polynomials, P_i is the amplitude assigned to a specific Zernike mode, ρ is the radial coordinate of the node measured from the center and is bounded by $0 \le \rho \le R_{max}$, $\phi = \tan^{-1}(z/x)$ in radians and z,x are coordinates of the mesh, and R_{max} is the center to corner distance of the mirror.

We calculate the RMSE in Eq. 13 by summing squares of position errors for each node (δ_i) over the set of nodes on the top surface of the mirror ($\mathbf{N}_s$). Note this is a redefinition of previous uses of δ, where

$$\delta_i = Z(x_i, y_i) - \hat{Z}_i. \tag{12}$$

For our application, we define Z as the desired mirror position for a given x,y location. In practice, we have mirror surface figure files provided by Zemax which describe the desired mirror top surface x,y,z locations for a set of gridded x,y points. To convert this into a function describing the z value at any x,y pair ($Z(x,y)$), we fit a 2D rectilinear spline to these points using a cubic interpolant. The variable $\hat{Z}_i$ describes the actual deformed position of the mirror at the associated $x_i y_i$ points.

$$RMSE = \sum_{i \in N_s} \delta_i^2 \tag{13}$$

So far, our force optimization process has resulted in RMSE = 47.6 μm with high deformations at the mirror edge driving error as shown in Figure 32. The maximum δ was 0.0001549 m and minimum delta was -0.0002489 m. This again confirms the need to directly control focus and additional, higher Zernike modes, and gives us another powerful tool for future investigations of such control.

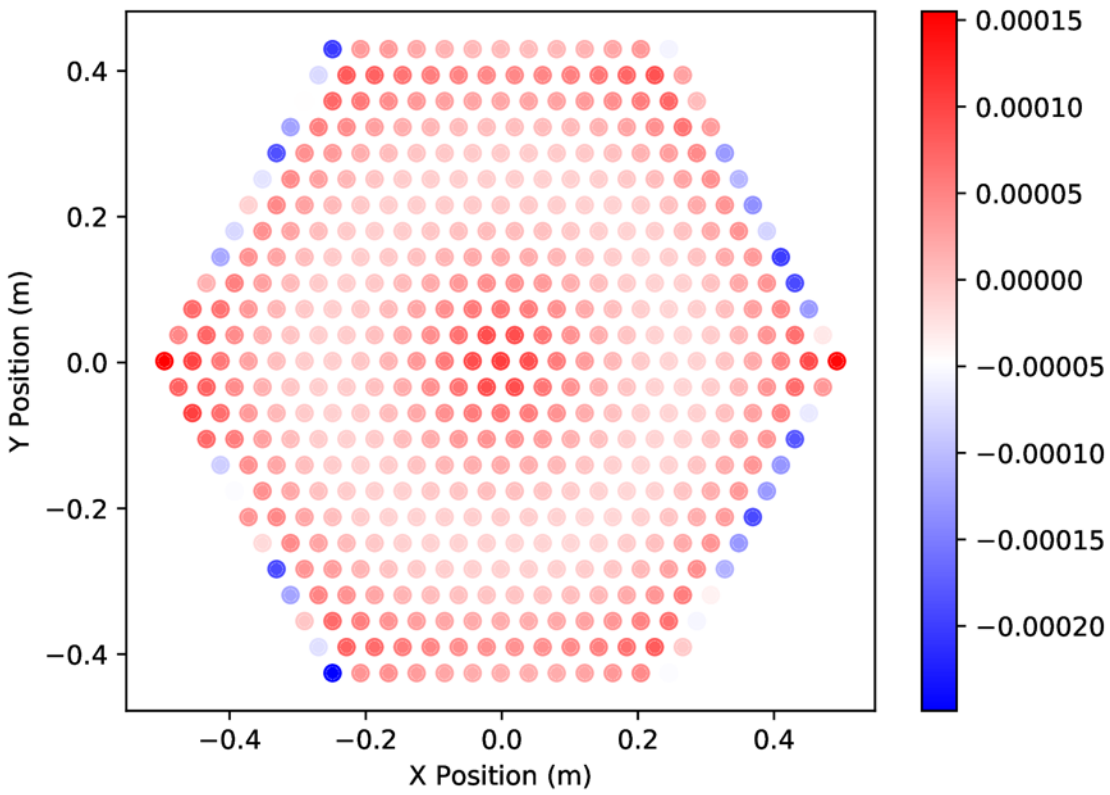

Figure 32: Minimum mirror surface figure error (δ) achieved through force optimization for mirror 99 using only radially symmetric zernike modes (i.e. n,m=[(2,0), (4,0), (6,0), (8,0), (10,0), (12,0), (14,0), (16,0)])

3 ORBITAL DESIGN

3.1 Historical Launch Analysis

Predicting future launch capability is central to determining how many segments can be launched as payloads of opportunity, and how many would have to be launched on rockets dedicated to this mission. To predict future launch capability, a historical launch analysis was performed, targeted at recent launches (2016-2018) from the United States.

This process began by gathering data on launch and payload history. Launch data was collected from the Orbital Launch Log [34], last updated in May of 2018. It includes data on launch dates, sites, vehicles, and the Committee on Space Research (COSPAR) designation for each payload on the launch.

Payload data was collected from the Union of Concerned Scientists' satellite catalogue [35], which contains orbital elements and payload mass for most satellites in order. Satellites were matched to launches using COSPAR designations.

Launches were selected based on their launch site, and year. For this analysis, launches from Kennedy Space Center/Cape Canaveral (KSC/CC), Wallops (W), and Vandenburg Airforce Base (V/VS) were selected, if they took place between January 1st, 2016, and December 31st, 2017. Once the payloads for each launch were identified based on their COSPAR designation, the mass of each payload, and the inclination and semi-major axis of their orbit was collected. The semi-major axis was used to calculate the characteristic energy (C_3) value for each payload. Launches where payload data was missing were removed from the data pool.

For launches with a full data set, a total payload mass, inclination, and C_3 value was calculated. The C_3 value for the launch was taken to be the weighted average of the C_3 values for each payload, weighted by mass. The inclination launch was taken to be the average inclination for each payload item.

Next, launches were categorized based on launch vehicle. Then, for each launch, a spare payload was calculated. This calculation was performed conservatively, by defining spare payload as the difference between a given launch's payload, and the maximum payload carried by the same launch vehicle, on a launch with an equal or higher C_3. This definition means that many flights have zero spare payload, but ensures that the spare payload estimate is based off of the payload capabilities that have been demonstrated by each launch vehicle.

For recent years (2016, 2017), many launches took place on launch vehicle variants that only had one flight. Many launches also took place on launch vehicles that had few enough flights that no spare payload could be calculated. For 2016-2017, Only the Falcon 9 and Atlas V 401 had enough launches to define spare payload. Therefore, only these launch vehicles were used to predict future spare payload capacity.

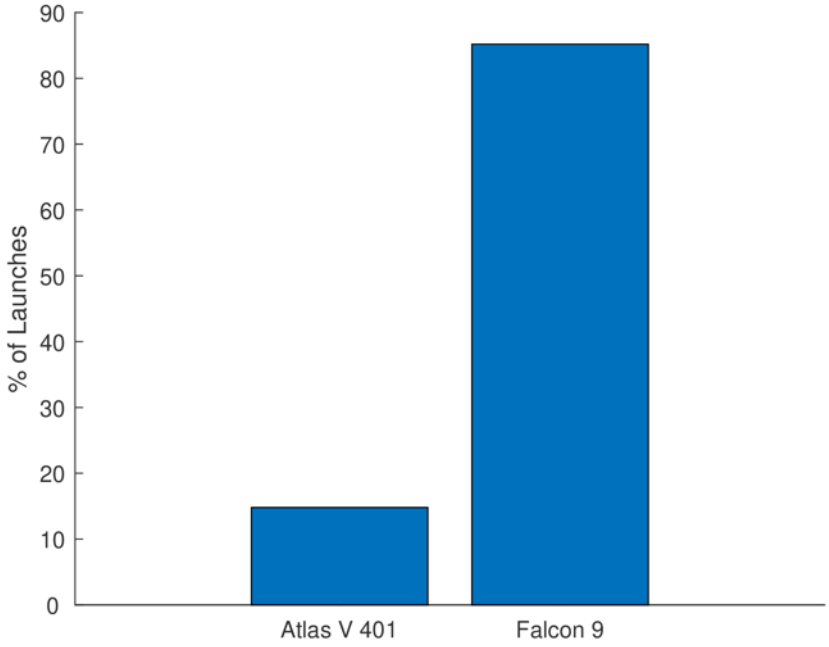

Figure 33: A histogram of of randomly generated future launches consistent with historical launch data. The x axis is the type of launch vehicle, and the blue bars indicate the percentage of future launches that will use that vehicle.

To predict future launch capacity, launches were randomly generated based on the historical launch data. The distribution of launch vehicles in 2016 and 2017 was used to randomly select a launch vehicle from the pool of launch vehicles for which spare payload was calculated. Once a launch was chosen, a launch profile was randomly selected from the launches for that vehicle from 2016 to 2017. The payload, spare payload, launch site, inclination, and C_3 for that launch were taken to be the values for the randomly generated launch.

Figure 34 shows 1000 randomly generated launches describing the projected distribution of future launches. The results from this analysis were that the majority of launches have little to no spare payload, and are launched on geosynchronous transfer orbits (GTO), which have little to no inclination. Fewer launches are to low Earth orbit, or are launched to a high inclination or polar orbit, and 43% of launches have more than 500 kg of spare payload.

To determine the number of modules that could be launched, random launches were generated for 7 years, with each year containing 34 launches (the total number of relevant US launches in 2018, and therefore a conservative estimate that doesn't project any growth in the orbital launch market). The spare payloads were then run through the methods described in Section 4.1.1, to estimate that there should be sufficient spare capacity to launch 1450 segments over a 7 year period. This indicates that the current rate of launches would be sufficient to launch all 840 modules in less than 7 years, with no dedicated launches required.

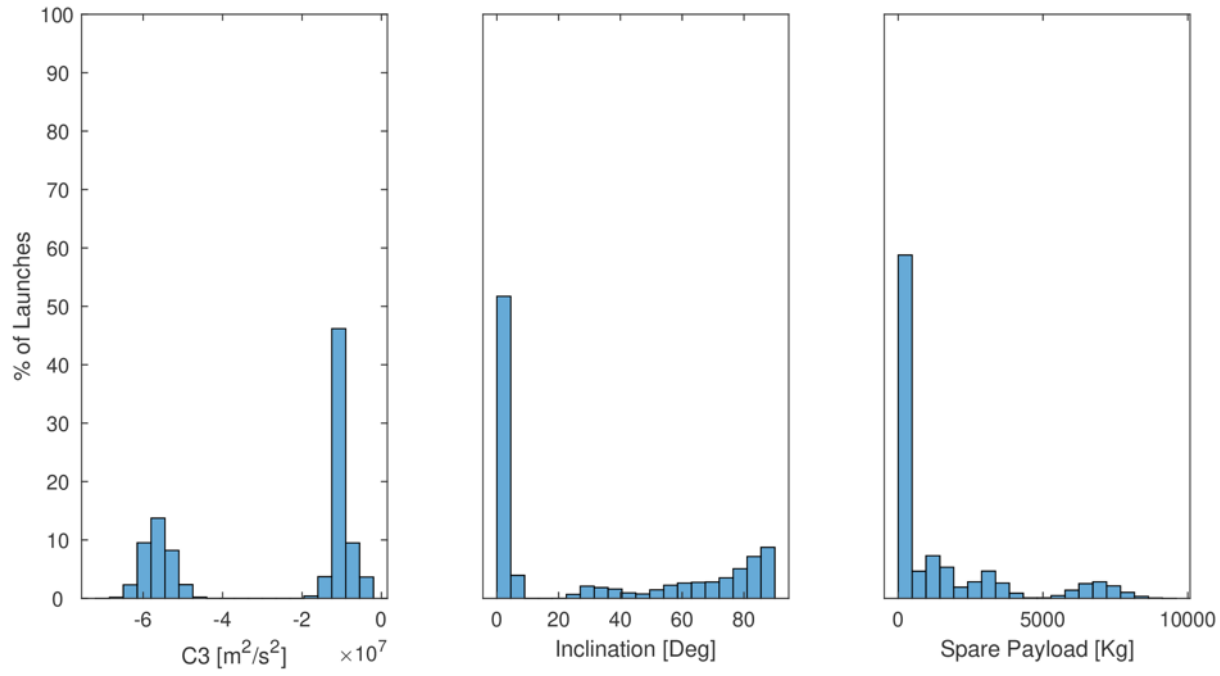

Figure 34: Histograms of randomly generated launch attributes. The figure on the left is a histogram of launch C_3, the center figure is a histogram of launch inclination, and the figure on the right is a histogram of spare payload capacity.

3.2 Dynamic Model

The trajectory design is framed within the Circular Three Body equations of motion [36], where a particle is under the gravitational influence of two primary bodies (in this case the Sun and Earth). The two primaries are assumed to be on circular orbits about their mutual center of mass. Let *I* be an inertial frame with origin *O*, coordinates (*X*,*Y*,*Z*), and orthonormal unit vectors $\hat{\mathbf{i}}, \hat{\mathbf{j}}, \hat{\mathbf{k}}$—the first two defining the ecliptic plane of the Earth's orbit. The origin coincides with the barycenter of the Sun and Earth. Dynamics are studied in a rotating frame where the primaries are stationary: a frame *R*–with origin *O*, coordinates (*x*,*y*,*z*), and orthonormal unit vectors $\hat{\mathbf{x}}, \hat{\mathbf{y}}, \hat{\mathbf{z}}$–defined to rotate with the two primaries as shown in Figure 35. The frame is centered on the barycenter of the Sun and the Earth. Non-dimensional units are used for distance and time: one distance unit (DU) is equal to the distance between the Sun and Earth (1 AU), one time unit TU is equal to the orbital period of the Sun and Earth about their center of mass divided by 2π. This ensures that the gravitational constant *G* and the mean orbital period ω are both 1. The mass unit (MU) is the mass sum of the two primaries. A reduced mass fraction is introduced, defined as

$$\mu = \frac{m_2}{m_1 + m_2}, \tag{14}$$

where m_1 and m_2 are the masses of the primaries (the Sun and Earth, respectively). μ is equal to both the mass of the smaller primary (the Earth) in non-dimensional units and the distance of the first primary from the barycenter, as shown in Figure 35.

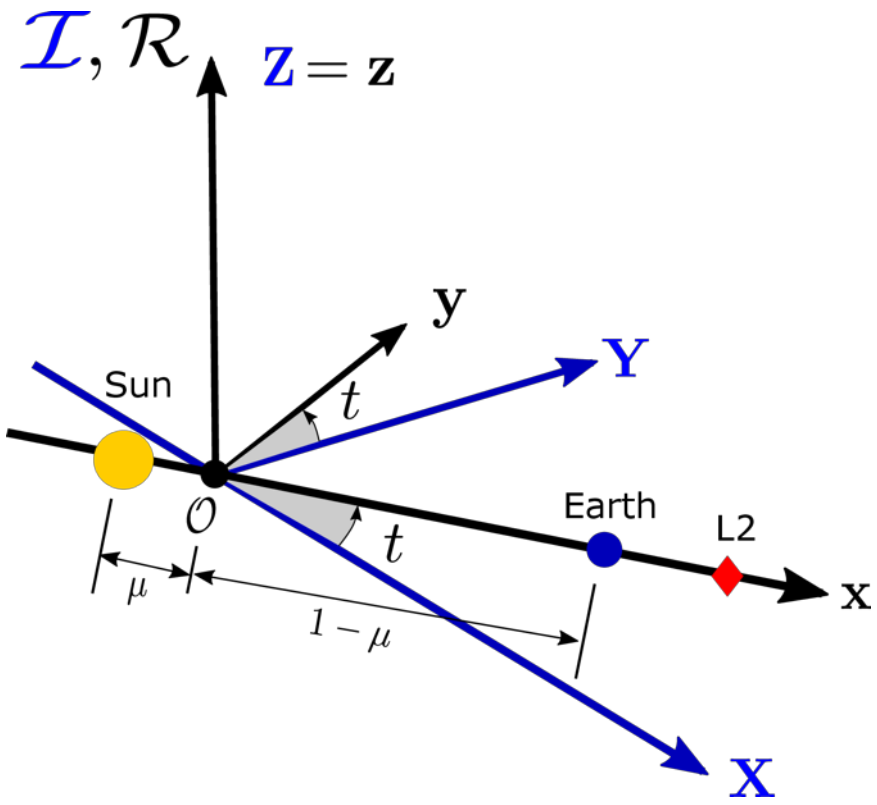

Figure 35: Diagram of the inertial I *and rotating* R *frames where the two primaries, the Sun and Earth, are fixed on the x-axis of* R*. Distances are shown in non-dimensionalized units.*

The equations of motion of the third body as influenced by the two primaries are

$$\begin{aligned} \ddot{x} - 2\dot{y} &= \frac{\partial \Omega}{\partial x} \\ \ddot{y} + 2\dot{x} &= \frac{\partial \Omega}{\partial y} \\ \ddot{z} &= \frac{\partial \Omega}{\partial z} \end{aligned} \tag{15}$$

where Ω is an effective potential term in the rotating frame dependent only on spatial coordinates:

$$\Omega(x, y, z) = \frac{1}{2}(x^2 + y^2) + \frac{1-\mu}{r_1} + \frac{\mu}{r_2}. \tag{16}$$

The terms r_1 and r_2 are the distances from each respective primary to the third object defined as

$$\begin{aligned} r_1 &= \sqrt{(\mu + x)^2 + y^2 + z^2} \\ r_2 &= \sqrt{(1 - \mu - x)^2 + y^2 + z^2}\,. \end{aligned} \tag{17}$$

Because the rotating frame is fixed onto the circular orbit of the two primaries, converting a position vector to an inertial frame involves a simple direction cosine matrix

$$Q = \begin{bmatrix} \cos(t) & -\sin(t) & 0 \\ \sin(t) & \cos(t) & 0 \\ 0 & 0 & 1 \end{bmatrix} \tag{18}$$

and its derivative

$$\dot{Q} = \begin{bmatrix} -\sin(t) & -\cos(t) & 0 \\ \cos(t) & -\sin(t) & 0 \\ 0 & 0 & 0 \end{bmatrix}. \tag{19}$$

The rotation of the full state vector from the rotating frame to the inertial frame is achieved by the following transformation matrix

$${}_{I}Q_{R} = \begin{bmatrix} Q & \mathbf{0}_{3\times3} \\ \dot{Q} & Q \end{bmatrix}. \tag{20}$$

where t is the time measured in TU. At the initial time t=0, the inertial and rotating frame align; this coincides with the vernal equinox by convention. The transformation matrix to rotate a state vector from the inertial frame to the rotating frame is

$${}_{R}Q_{I} = \begin{bmatrix} Q^{T} & \mathbf{0}_{3\times3} \\ -Q^{T}\dot{Q}Q^{T} & Q^{T} \end{bmatrix}. \tag{21}$$

The equations of motion can be integrated by converting the second-order equations into a first order system. The full state vector includes both positions and velocities as follows

$$\mathbf{x} = [\ \mathbf{r}\ \ \mathbf{v}\ ]^{T} = [\ x\ \ y\ \ z\ \ \dot{x}\ \ \dot{y}\ \ \dot{z}\ ]^{T}. \tag{22}$$

The differential equations for each of the state variables are therefore

$$\dot{\mathbf{x}} = \mathbf{f}(t,\mathbf{x}) = \begin{bmatrix} \dot{\mathbf{r}} \\ \dot{\mathbf{v}} \end{bmatrix} = \begin{bmatrix} \dot{x} \\ \dot{y} \\ \dot{z} \\ 2\dot{y} + \frac{\partial \Omega}{\partial x} \\ -2\dot{x} + \frac{\partial \Omega}{\partial y} \\ \frac{\partial \Omega}{\partial z} \end{bmatrix} \tag{23}$$

using Eq. 15 given previously. An energy integral of motion also exists for these equations of motion, called the Jacobi integral, and is given by convention as

$$C = -(\dot{x}^{2} + \dot{y}^{2} + \dot{z}^{2}) - 2\Omega \tag{24}$$

which is a function of the position and velocity coordinates in the rotating frame.

3.2.1 Points of Equilibrium

The Circular Three Body equations of motion have five equilibrium points: three are collinear with the two primaries while the other two are off-axis but on the same orbit plane. The equilibrium points are found by setting the right hand side of Eq. 23 equal to zero [36] while ignoring the z-direction. The collinear equilibrium points are the critical points that solve

$$\left.\frac{\partial \Omega}{\partial x}\right|_{y=0} = 0. \tag{25}$$

Through some algebraic manipulation [37], the location of L2 for a given μ is the unique positive, real solution of the quintic equation

$$\gamma^5 + (3-\mu)\gamma^4 + (3-2\mu)\gamma^3 - \mu\gamma^2 - 2\mu\gamma - \mu = 0 \qquad (26)$$

where γ is the distance from the second, smaller primary (in our case, the Earth). This equilibrium point is located on the right side of the origin on the x-axis of the *R* frame in Fig 35 past the Earth. To an observer near L2, the Sun, Earth, and Moon are almost perfectly aligned. Orbits about L2 are therefore lucrative final locations for a space telescope that wants to maximize its possible pointing range: it is limited by light coming from approximately one location in the sky rather than three distinct sources at different locations.

3.3 Parking Orbit

The fully assembled primary mirror will operate near Sun-Earth L2 as in the LUVOIR design [38]. The mirror assembly will take place on a parking orbit about L2—a Lissajous orbit which maximizes the probability that individual modules will come within close enough proximity to rendezvous and dock together. The following sections describe the methods used to obtain periodic orbits and the quasi-periodic Lissajous orbit. Periodic orbits such as the vertical Lyapunov are used to generate invariant manifolds near the Earth.

3.3.1 First Order Approximation

A first order approximation for the equations of motion about L2 can be used as an initial guess for the iterative numerical methods that generate periodic and quasi-periodic orbits. First, the coordinates of the *R* frame are translated so that L2 is the new origin *O*' [36, 39] as shown in Fig 36. The length unit is also scaled so that the distance between the second primary (the Earth) and L2 γ is 1. The rescaling ensures that the series expansions in Legendre polynomials holds [39]. The change of coordinates is given as

$$\begin{aligned} \bar{x} &= \frac{x - (1-\mu+\gamma)}{\gamma} \\ \bar{y} &= \frac{y}{\gamma} \\ \bar{z} &= \frac{z}{\gamma}. \end{aligned} \qquad (27)$$

If we keep the mass unit the same as before (i.e. scaled by the mass sum of the two primaries) we would need to change the time unit so that the gravitational constant for the system is still equal to 1. We achieve this by introducing a new time variable [39]

$$\tau = \gamma^{\frac{3}{2}} t. \qquad (28)$$

The proportionality constant is found by solving Kepler's Third Law so that

$$G(M_1 + M_2) = \dot{\theta}^2 r_{12}^3 = 1 \qquad (29)$$

where $\dot{\theta}$ is the rate of rotation of the *R* frame relative to the inertial frame *I* and r_{12} is the distance between the primaries. Derivatives in τ are denoted with a $()'$ symbol.

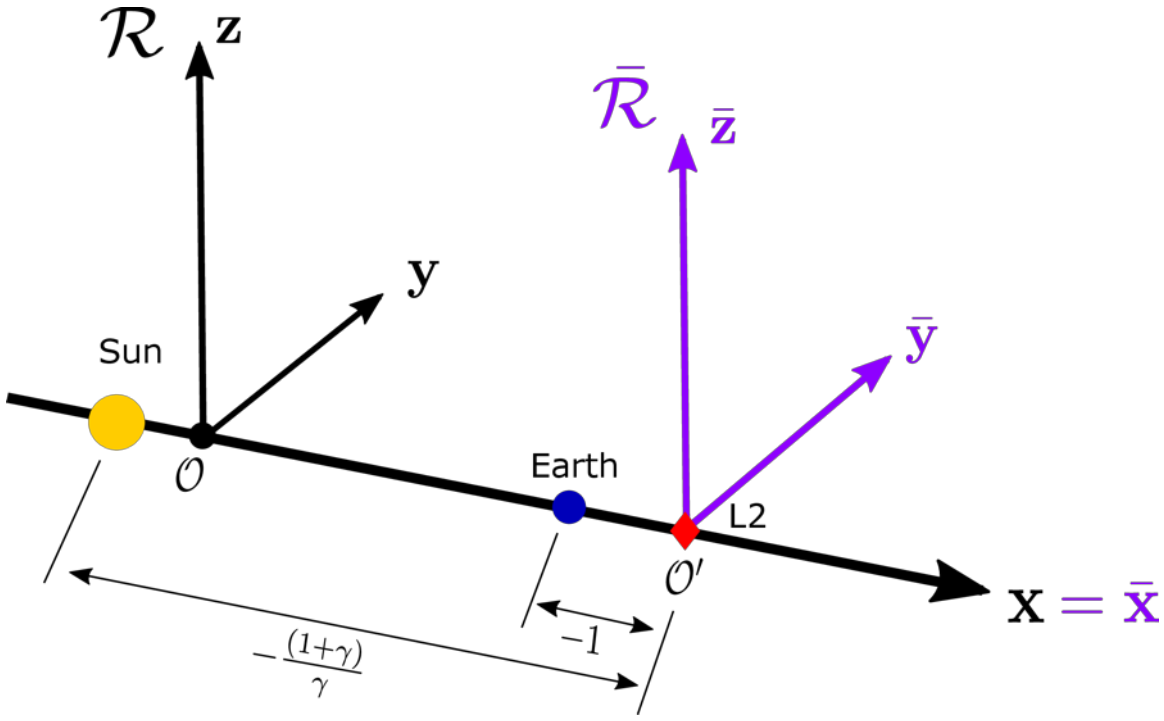

Figure 36: Diagram of the rotating R *frame and the new* R *frame centered about L2, the new origin* O′*. Distances from the primaries are shown in new non-dimensionalized units, where the length unit is scaled by the distance γ between the Earth and L2.*

Next, the nonlinear terms in Eq. 23, mainly the spatial terms $\frac{1-\mu}{r_1}+\frac{\mu}{r_2}$ of the effective potential Ω, are expanded in Legendre polynomials [39, 40]. The equations of motion are then written as

$$\begin{aligned}
\bar{x}'' - 2\bar{y}' - (1+2c_2)\bar{x} &= \frac{\partial}{\partial \bar{x}} \sum_{n\geq 3} c_n \rho^n P_n\left(\frac{\bar{x}}{\rho}\right) \\
\bar{y}'' + 2\bar{x}' + (c_2 - 1)\bar{y} &= \frac{\partial}{\partial \bar{y}} \sum_{n\geq 3} c_n \rho^n P_n\left(\frac{\bar{x}}{\rho}\right) \\
\bar{z}'' + c_2\bar{z} &= \frac{\partial}{\partial \bar{z}} \sum_{n\geq 3} c_n \rho^n P_n\left(\frac{\bar{x}}{\rho}\right)
\end{aligned} \tag{30}$$

where $\varrho^2=x^2+y^2+z^2$ and the coefficients c_n are defined as

$$c_n = \frac{(-1)^n}{\gamma^3}\left(\mu + \frac{(1-\mu)\gamma^{n+1}}{(1+\gamma)^{n+1}}\right) \tag{31}$$

for motion about L2. We obtain a first order approximation of the equations of motion by setting the right hand side of each equation to be zero as follows

$$\bar{\mathbf{x}}' = \mathbf{f}(\tau, \bar{\mathbf{x}}) = \begin{bmatrix} \bar{x}' \\ \bar{y}' \\ \bar{z}' \\ 2\bar{y}' + (1 + 2c_2)\bar{x} \\ -2\bar{x}' - (c_2 + 1)\bar{y} \\ -c_2\bar{z} \end{bmatrix}. \tag{32}$$

Finally, we want an approximation of the periodic orbits using Eq. 32. Motion in the z-axis is simple-harmonic since $c_2>0$ and is only dependent on μ and γ. Motion in the xy-plane is coupled; analysis of the linear behavior shows that its characteristic equation has two real and two imaginary roots ($\pm\lambda, \pm i\omega_p$). Choosing initial conditions to restrict the exponential solutions yields bounded solutions in the xy-plane. The solutions are of the form

$$\bar{\mathbf{r}} = \begin{bmatrix} -A_x \cos(\omega_p \tau + \phi) \\ \kappa A_x \sin(\omega_p \tau + \phi) \\ A_z \sin(\omega_z \tau + \psi) \end{bmatrix} \tag{33}$$

where

$$\kappa = \frac{\omega_p^2 + 1 + 2c_2}{2\omega_p} \tag{34}$$

and ω_p and ω_z are the in-plane and out-of-plane frequencies respectively given as

$$\omega_p^2 = \frac{2 - c_2 + \sqrt{9c_2^2 - 8c_2}}{2} \tag{35}$$

and

$$\omega_z^2 = c_2. \tag{36}$$

These derivations are shown in more detail within [36]. Ultimately, these solutions produce Lissajous-type trajectories as shown in Fig. 37 that can be used as initial guesses to find both periodic and quasi-periodic orbits within the full Circular Three Body equations of motion (i.e. Eq. 23).

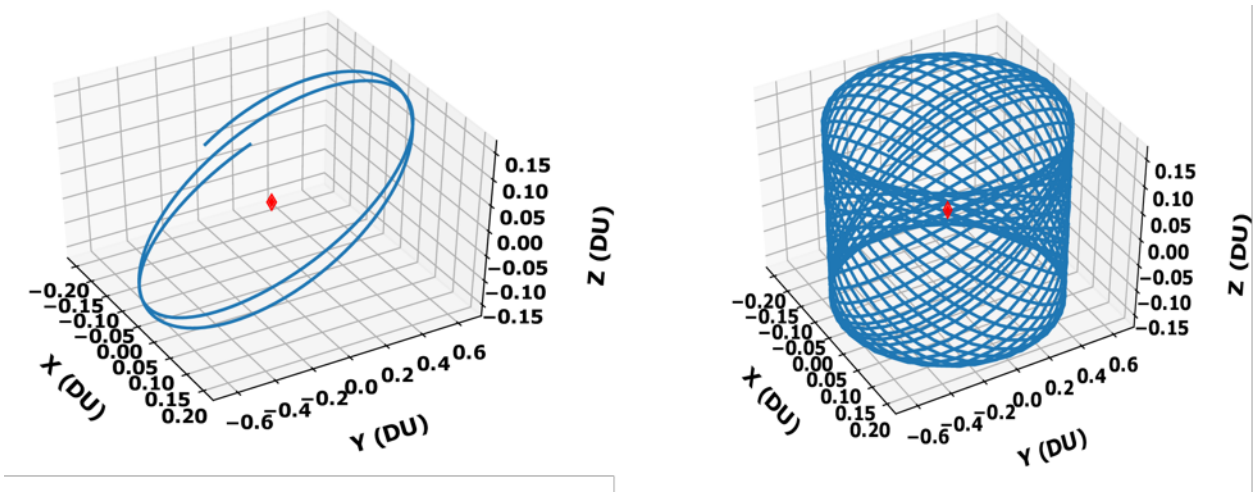

Figure 37: First order approximation of a Lissajous orbit for 2 (left) and 15 (right) revolutions in and out of the xy-plane. Amplitudes of 300,000 km and 250,000 km were used in the in-plane and out-of-plane terms respectively.

3.3.2 Differential Control

Differential control is employed to refine initial conditions within the full equations of motion to a desired reference trajectory. Let the flow map of the dynamical system $\dot{\mathbf{x}}=\mathbf{f}(\mathbf{x})$ be defined as

$$\phi(t, t_0) : \mathbf{x}(t_0) \mapsto \mathbf{x}(t) \tag{37}$$

where t_0 denotes some initial time. The same flow map can be defined as $\varphi(t;\mathbf{x}_0)$ to show dependency on the initial conditions of the state. If we vary the initial state by some $\delta\mathbf{x}_0$, a neighboring trajectory is formed. The difference in states between these two trajectories at some time t_1 is

$$\delta\mathbf{x}(t_1) = \phi(t_1; \mathbf{x}_0 + \delta\mathbf{x}_0) - \phi(t_1; \mathbf{x}_0). \tag{38}$$

Through a Taylor Series expansion of these terms, a first order relationship between the initial and final state differences of the neighboring trajectories emerges:

$$\delta\mathbf{x}(t_1) = \frac{\partial\phi(t_1; \mathbf{x}_0)}{\partial\mathbf{x}_0}\delta\mathbf{x}_0 \tag{39}$$

which can be rewritten as

$$\delta\mathbf{x}_1 = \mathbf{\Phi}(t_1, t_0)\delta\mathbf{x}_0 \tag{40}$$

where $\mathbf{\Phi}(t_1,t_0)$ is the state transition matrix from t_0 to t_1. The state transition matrix is the solution to the variational differential equations of $\mathbf{f}(\mathbf{x})$:

$$\dot{\mathbf{\Phi}}(t, t_0) = \frac{\partial\mathbf{f}(\mathbf{x})}{\partial\mathbf{x}}\mathbf{\Phi}(t, t_0). \tag{41}$$

The Jacobian is defined as

$$\frac{\partial \mathbf{f}(\mathbf{x})}{\partial \mathbf{x}} = \begin{bmatrix} \mathbf{0}_{3\times 3} & \mathbf{I}_{3\times 3} \\ -\mathcal{U} & 2\Delta \end{bmatrix} \tag{42}$$

where $\mathbf{I}_{3\times 3}$ is a 3 by 3 identity matrix,

$$\Delta = \begin{bmatrix} 0 & 1 & 0 \\ -1 & 0 & 0 \\ 0 & 0 & 0 \end{bmatrix}, \tag{43}$$

and

$$\mathcal{U} = \begin{bmatrix} \Omega_{xx} & \Omega_{xy} & \Omega_{xz} \\ \Omega_{yx} & \Omega_{yy} & \Omega_{yz} \\ \Omega_{zx} & \Omega_{zy} & \Omega_{zz} \end{bmatrix}. \tag{44}$$

For a system of 6 differential equations **f**(**x**) in position and velocity variables, the variational equations add 36 more for a total of 42 ordinary differential equations needed to be solved. Once they are solved, however, a trajectory and state transition matrix are produced. The state transition matrix maps how a variation in the initial state vector is propagated from time t_0 to time t_1. The state transition matrix is also invertible [36], meaning that a deviation in final states can be mapped back to a deviation in the initial states like so

$$\delta \mathbf{x}_0 = \mathbf{\Phi}(t_1, t_0)^{-1} \delta \mathbf{x}_1. \tag{45}$$

It is also important to note that

$$\mathbf{\Phi}(t_1, t_0)^{-1} = \mathbf{\Phi}(t_0, t_1). \tag{46}$$

Differential correction can therefore be used to iterate upon initial conditions to find a trajectory that maps to the desired final state. If we let $\mathbf{x}_D$ be the desired final state, then

$$\delta \mathbf{x}_1 = \mathbf{x}_D - \mathbf{x}(t_1) \tag{47}$$

where $\mathbf{x}(t_1)$ is the final state after integrating the 42 ODEs using the initial state $\mathbf{x}_0$=$\mathbf{x}(t_0)$. Eq. 45 maps this back to a deviation in initial state $\delta\mathbf{x}_0$ which is used to re-run the integration but with initial conditions $\mathbf{x}_0$+$\delta\mathbf{x}_0$. These steps are repeated until convergence; if the initial trajectory is close enough to the desired trajectory, convergence should occur within 3 or 4 iterations.

3.3.3 Solving a Boundary Value Problem

The process of finding periodic and quasi-periodic orbits can also be framed as a boundary value problem by cleverly selecting boundary conditions [41, 42]. The boundary value problem (BVP) for the L2 orbits is solved using collocation method `solve_bvp`, a Python implementation found in the `scipy` package [43] that is similar to MATLAB's `bvp4c` [44]. Collocation points are selected by the user which are constrained by boundary conditions (BCs) at some times t_a or t_b, either at the start or end of the trajectory in our case. The number of collocation points must be equal to the number of equations if no other variable parameters are included in the equations. The collocation algorithm selects an initial number of nodes and fits a continuous cubic spline between the nodes. It then compares the first derivatives of the cubic spline with the equations of motion

and iterates until the residual errors are below some specified tolerance, increasing or decreasing the number of nodes in the process.

3.3.4 Periodic Orbits

There are three main types of periodic orbits about L2: horizontal Lyapunov, vertical Lyapunov, and halo orbits. The former orbits strictly in the xy-plane while the other two have motion in the z-direction. We chose to find a family of vertical Lyapunov as an example. The vertical Lyapunov orbits form a figure-8 shape as they orbit near L2. The first order approximation of a Lissajous can be used as an initial guess within the full equations of motion (once they are converted back to the R frame from the $\bar{R}$ frame). The collocation algorithm described in Section 3.3.3 is used to find convergent solutions to the vertical Lyapunov. Only a quarter of the figure-8 is used within the boundary conditions: the initial BC is taken to be at the top of the orbit (maximum height z) and the final BC is at the crossing of the xy-plane. The corresponding BCs are

$$\begin{bmatrix} y(t=0) \\ \dot{x}(t=0) \\ \dot{z}(t=0) \\ y(t=T/4) \\ z(t=T/4) \\ \dot{x}(t=T/4) \end{bmatrix} = \mathbf{0} \tag{48}$$

where T is the full period of the vertical Lyapunov. A family of vertical Lyapunovs is shown in Fig. 38, found by altering the amplitudes of the first order approximation in Eq. 33 and solving the corresponding BVPs.

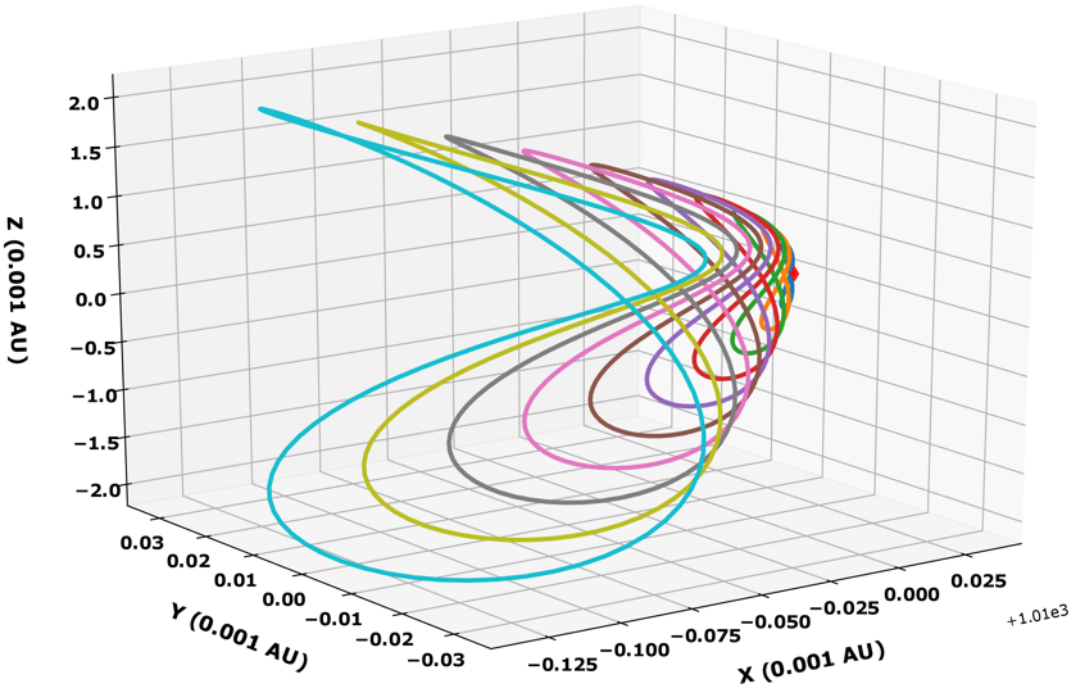

Figure 38: A family of Vertical Lyapunov periodic orbits found about the Sun-Earth L2.

3.3.5 Lissajous Orbits

The quasi-periodic Lissajous orbits were found using a two-step differential correction process given in [45] and summarized here. The first order linear approximation of the Lissajous is used as an initial guess and iterated upon until convergence. The initial trajectory is divided into segments as shown in Fig 39. In the first step, a trajectory is created which is continuous in position. The points p_- and p_+ are consolidated into a single point p. An initial value problem is solved by integrating the state $\mathbf{x}_0$ forwards in time to point p (or the time t_p during which the trajectory "should" be at point p). The full 6 equations of motion Eq. 23 are integrated along with the 36 variational equations (Eq. 41). A discontinuity in position is created which can be related back to a deviation in initial position by differential correction:

$$\delta \mathbf{x}_p = \mathbf{\Phi}(t_p, t_0)\delta \mathbf{x}_0 + \left.\frac{\partial \mathbf{x}}{\partial t}\right|_p \delta(t_p - t_0). \tag{49}$$

An extra term is introduced to Eq. 40 to determine a variation in the time of integration $t_p - t_0$. The difference between the desired final positions and the resultant positions from the integration are summarized in the vector

$$\mathbf{b} = [\ \delta x_p\ ,\ \delta y_p\ ,\ \delta z_p\ ]^T. \tag{50}$$

The deviations in the initial velocities and integration times that result in this neighboring trajectory, as described in Sec 3.3.2, are

$$\mathbf{u} = [\ \delta \dot{x}_0\ ,\ \delta \dot{y}_0\ ,\ \delta \dot{z}_0\ ,\ \delta(t_p - t_0)]^T. \tag{51}$$

Since not every element of the state transition matrix is relevant in finding $\delta \mathbf{x}_p$, it is truncated into the following matrix

$$\mathbf{L} = \begin{bmatrix} \Phi_{14} & \Phi_{15} & \Phi_{16} & \dot{x} \\ \Phi_{24} & \Phi_{25} & \Phi_{26} & \dot{y} \\ \Phi_{34} & \Phi_{35} & \Phi_{36} & \dot{z} \end{bmatrix} \tag{52}$$

The relationship between the initial and final deviations between the neighboring trajectories is therefore

$$\mathbf{L}\mathbf{u} = \mathbf{b}. \tag{53}$$

The needed deviations in initial conditions can be found by solving for **u** as follows

$$\mathbf{u} = \mathbf{L}^+\mathbf{b} \tag{54}$$

where $\mathbf{L}^+$ is the pseudo-inverse of **L** defined as

$$\mathbf{L}^+ = \mathbf{L}^T(\mathbf{L}\mathbf{L}^T)^{-1} \tag{55}$$

which, according to linear algebra, gives the solution to Eq. 53 with the smallest Euclidean norm (since we have three equations and four unknowns). A new initial value problem is then solved with the velocity and time deviations found from **u**. This is repeated until the difference $\mathbf{x}_p$ is below some tolerance. Once the tolerance is small enough, a BVP can also be solved using the collocation method in Section 3.3.3 to drive the error down even further. A trajectory that is continuous in position is therefore created, though with discontinuities in velocity space.

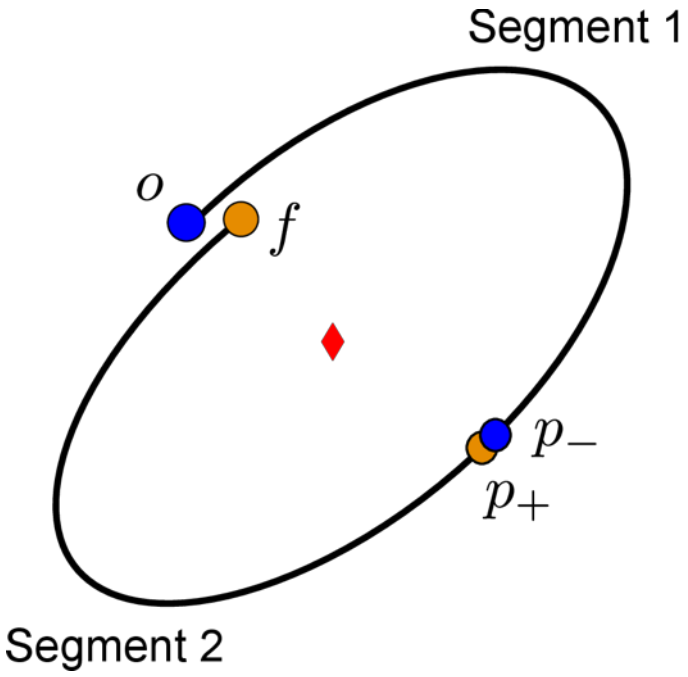

Figure 39: Set-up of segments for the two-step differential process of finding Lissajous orbits. Initial guess is divided into two segments: segment (o, p_) and segment (p_+, f). The L2 point is shown as the red diamond in the center.

The second step of the differential correction process is to create a trajectory continuous in velocity space using the result of the first step. Two simultaneous initial value problems are solved by integrating the state $\mathbf{x}_0$ forward in time and the state $\mathbf{x}_f$ backward in time, both to the point *p* (or to the time t_p corresponding to the point *p*). The final states of either integration will not coincide on the first iteration; these states are therefore labelled p_- and p_+ respectively. The deviations at both of these points will be

$$\delta\mathbf{x}_{p+} = \mathbf{\Phi}(t_{p+}, t_f)\delta\mathbf{x}_f + \left.\frac{\partial\mathbf{x}}{\partial t}\right|_{p+}\delta(t_{p+} - t_f) \tag{56}$$

and

$$\delta\mathbf{x}_{p-} = \mathbf{\Phi}(t_{p-}, t_0)\delta\mathbf{x}_0 + \left.\frac{\partial\mathbf{x}}{\partial t}\right|_{p-}\delta(t_{p-} - t_0) \tag{57}$$

similarly to the first step. However, the difference in "final" velocity (i.e. the velocity difference at point *p*) will be driven to zero in this second iteration process by varying the positions at points *o*, *p*, and *f*. Since the calculations are rather lengthy, further details can be found in [45] on how the Δv_p is minimized as well as how multiple simultaneous segment results can be incorporated into one final truncated state transition matrix. The final Lissajous, which can be integrated within the full three body equations of motion, is shown in Fig 40. The trajectory, as can be seen in the figure, frequently intersects itself especially near the top and bottom parts of the orbit (above and below

the xy-plane). These close points of contact make it a suitable parking orbit for modules to rendezvous and dock. The rendezvous of modules will be explored in greater detail in Section 3.6.

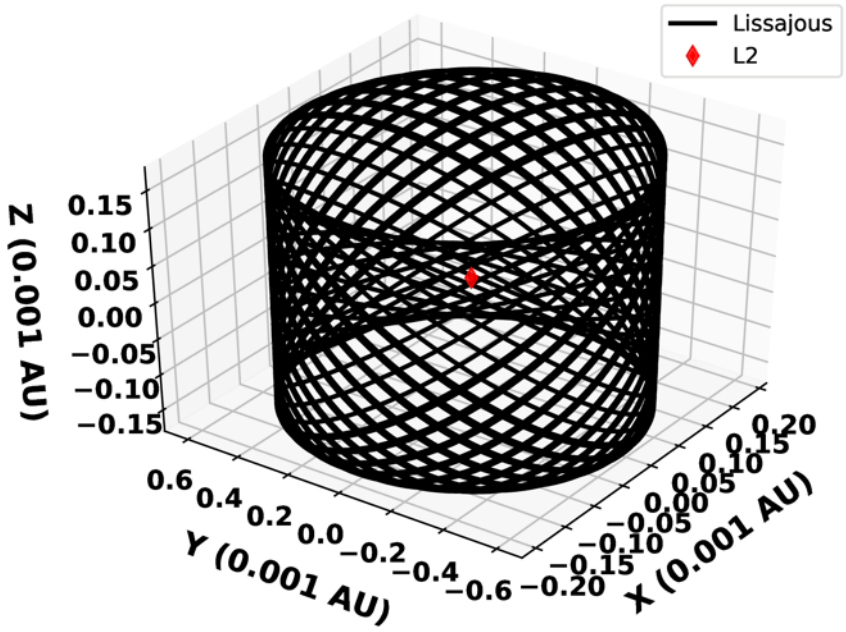

Figure 40: Lissajous about the Sun-Earth L2 found through a two-step differential correction process.

3.4 Escape Trajectories

The transfer to Sun-Earth L2 by means of solar sail is a difficult problem to solve given the nonlinearity of the equations of motion coupled with a highly constrained "thrust" that is very sensitive to direction and relatively low energy initial conditions compared to the desired final states. The transfer to L2 is facilitated by dividing the trajectory into manageable segments [46]: first an escape trajectory from Earth orbit, then a transfer to L2 targeting the Lissajous. The following sections describe the methods used to achieve these orbits although some will be the focus of future work. This section specifically describes the methods used to escape Earth orbit with a solar sail and how results are used as mission design tools.

3.4.1 Solar Sail Model

Each modular spacecraft is propelled by a solar sail in order to rendezvous and dock into the large segmented primary mirror. We assume an ideal solar sail model where the solar radiation pressure force is perfectly reflected from the surface of the sail [47, 48]. A square sail is also assumed. The acceleration due to the radiation pressure force on the solar sail is given by

$$\mathbf{a}_S = \beta \frac{1-\mu}{r_1^2}(\hat{\mathbf{r}}_1 \cdot \hat{\mathbf{n}})^2 \hat{\mathbf{n}} \tag{58}$$

where all units are non-dimensionalized. As shown in Figure 41, $\hat{\mathbf{r}}_1$ is the position vector from the first primary to the spacecraft and $\hat{\mathbf{n}}$ is a unit vector normal to the solar sail. The components of $\hat{\mathbf{n}}$ can be expressed in an auxilliary S frame defined as follows

$$\begin{aligned}\hat{\mathbf{s}}_1 &= \hat{\mathbf{r}}_1 \\ \hat{\mathbf{s}}_2 &= \frac{\hat{\mathbf{z}} \times \hat{\mathbf{s}}_1}{|\hat{\mathbf{z}} \times \hat{\mathbf{s}}_1|} \\ \hat{\mathbf{s}}_3 &= \hat{\mathbf{s}}_1 \times \hat{\mathbf{s}}_2\end{aligned} \tag{59}$$

where $\hat{\mathbf{z}}$ is the unit vector perpendicular to the Earth and Sun's orbit as defined in the R frame. In this new S frame, the components of $\hat{\mathbf{n}}$ can be expressed as spherical angles

$$\hat{\mathbf{n}} = \begin{bmatrix} \cos(\alpha) \\ \sin(\alpha)\cos(\delta) \\ \sin(\alpha)\sin(\delta) \end{bmatrix} \tag{60}$$

where α and δ are spherical angles representing the pitch and clock of the solar sail attitude. With this definition, the solar sail acceleration is rewritten as

$$\mathbf{a}_S = \beta \frac{1-\mu}{r_1^2} \cos^2(\alpha) \hat{\mathbf{n}} \tag{61}$$

The parameter β is a non-dimensional number that represents the sail performance. It is defined as

$$\beta = \frac{\sigma^*}{\sigma} \tag{62}$$

where σ is the total areal loading factor of the spacecraft and σ^* is a constant equal to

$$\sigma^* = \frac{L_\odot}{2\pi G M_\odot} \tag{63}$$

where actual units are used ($L_\odot$ is the solar luminosity at 1 AU). The total sail loading parameter depends on the total mass m_T of the spacecraft. For the purposes of our design study, the mass is split into a payload mass and a solar sail mass: the latter constitutes the sail and all the structures needed to pack and unfurl the sail, the former represents all other subsystems including the structure and mirror payload. The total sail loading factor then becomes

$$\sigma = \frac{m_T}{A_s} = \frac{m_p + m_s}{A_s} = \frac{m_p}{A_s} + \sigma_s \tag{64}$$

where m_p is the payload mass, m_s is the sail and sail structure combined mass, A_s is the area of the square sail, and σ_s is defined as the sail density.

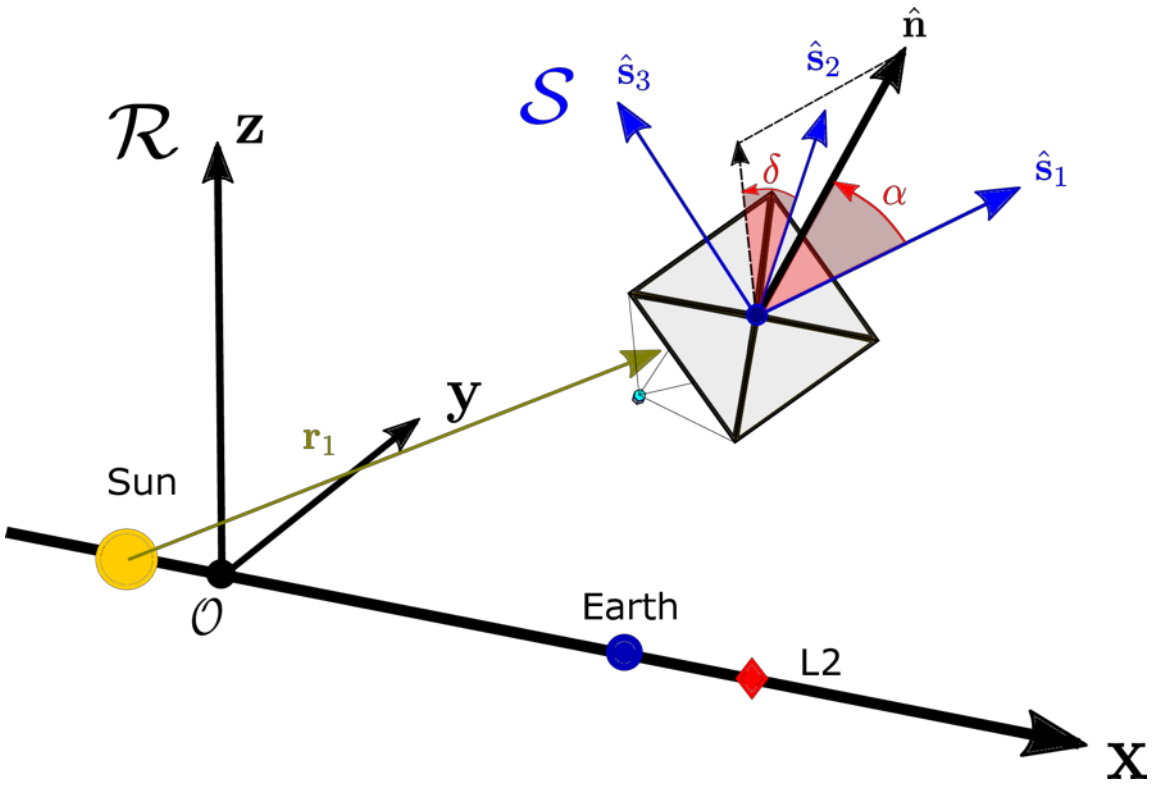

Figure 41: Isometric view of the rotating frame including definition of clock and pitch angles for a solar sail relative to the axes.

The solar radiation pressure acceleration can be expressed as an additional acceleration on the original Circular Three Body equations of motion as follows:

$$\dot{\mathbf{x}} = \mathbf{f}(t, \mathbf{x}, \mathbf{u}) = \begin{bmatrix} \dot{x} \\ \dot{y} \\ \dot{z} \\ 2\dot{y} + \frac{\partial \Omega}{\partial x} + \mathbf{a}_S \cdot \hat{\mathbf{x}} \\ -2\dot{x} + \frac{\partial \Omega}{\partial y} + \mathbf{a}_S \cdot \hat{\mathbf{y}} \\ \frac{\partial \Omega}{\partial z} + \mathbf{a}_S \cdot \hat{\mathbf{z}} \end{bmatrix} \tag{65}$$

where $\mathbf{u}$ is the vector of input variables $[\,\alpha\,\delta\,]^T$. The equations can be integrated forward or backwards in time for a given set of input variables; we now try to identify the control history of the pitch and clock angles that lead to our desired trajectories.

3.4.2 Drag Constraints

Before analyzing trajectories, we must first consider constraints on initial solar sail deployment due to drag effects. When fully deployed, the solar sail will be slowed down by atmospheric drag in LEO or during small periapsis. Initial Earth orbits must start above a minimum periapsis before the sail can be unfurled to avoid crashing back down to the Earth surface.

The atmospheric drag specific force is defined from the following equation [49]

$$a_D = \frac{1}{2}\rho A_s \frac{C_D}{m_T} v^2, \tag{66}$$

where ϱ is atmospheric density, A_s is the cross-sectional area of the spacecraft (essentially the area of the sail), C_D is the drag coefficient, m_T is the total spacecraft mass, and *v* is the velocity of the spacecraft relative to the atmosphere. A drag coefficient of 2.2 was selected for this study. Atmospheric density varies with altitude as

$$\rho = \rho_B \exp\left[-\frac{g_0 M(h-h_B)}{RT_B}\right]. \tag{67}$$

Values were interpolated using a MATLAB package [50] and standard atmospheric data [51]. The relative velocity *v* is defined more formally as

$$v = |{}^{\mathcal{I}}\mathbf{v}_{S/O} - {}^{\mathcal{I}}\mathbf{v}_{atm/O}| \tag{68}$$

where $I\mathbf{v}_{S/O}$ is the spacecraft velocity and $I\mathbf{v}_{atm/O}$ is the velocity of the atmosphere, both defined in an inertial frame *I* with origin *O*. For simplicity, the spacecraft is assumed to be on a circular orbit about Earth for a range of altitudes *h* as follows

$$\mathcal{E}v_{S/E} = \sqrt{\frac{GM_{Earth}}{R_{Earth}+h}} \tag{69}$$

where Ev_S is the geocentric velocity of the spacecraft in an Earth-centered frame *E*, M_{Earth} is the mass of the Earth, R_{Earth} is the radius of the Earth and *G* is the gravitational constant. The Earth is also assumed to be in a circular orbit about the origin *O*, the Sun-Earth barycenter. The full velocity expression is therefore

$${}^{\mathcal{I}}\mathbf{v}_{S/O} = {}^{\mathcal{E}}\mathbf{v}_{S/E} + {}^{\mathcal{I}}\omega^{\mathcal{E}} \times \mathbf{r}_{S/E} + {}^{\mathcal{I}}\mathbf{v}_{E/O} \tag{70}$$

where $E\mathbf{v}_{S/E}$ is the spacecraft velocity in the Earth frame relative to the Earth's location, $I\boldsymbol{\omega}E$ is the rate of rotation of the Earth frame *E* relative to the inertial frame *I*, $\mathbf{r}_{S/E}$ is the spacecraft location relative to the Earth, and $I\mathbf{v}_{E/O}$ is the Earth's tangential velocity relative to the inertial origin *O*. If we define v_E as the Earth's circular speed in the inertial frame and we assume all velocities are pointing in the same direction, then we get

$${}^{\mathcal{I}}v_{S/O} = {}^{\mathcal{E}}v_{S/E} + \frac{v_E}{r_E}(R_{Earth}+h) + v_E \tag{71}$$

where r_E is the radius of the Earth's orbit (1 AU). The atmospheric velocity is found similarly by assuming the atmosphere moves with the Earth's rotation:

$${}^{\mathcal{E}}v_{atm/E} = (R_{Earth}+h)\Omega_{Earth} \tag{72}$$

where Ω_{Earth}=2π/(23.93*hrs*) converted to the appropriate units. The full velocity of the atmosphere is defined in the same frame as for the spacecraft, so the velocity difference can finally be written as

$$v = {}^{\mathcal{E}}v_{S/E} - {}^{\mathcal{E}}v_{atm/E}. \tag{73}$$

The atmospheric drag equation can be rewritten as

$$a_D = \frac{1}{2}\rho\frac{C_D}{\sigma}v^2, \tag{74}$$

to incorporate the same parameters as a_S for the solar sail in this study.

An array of values for solar sail side length and height above the Earth's surface are used to calculate values for both drag and SRP accelerations. The height affects the drag acceleration more than the solar radiation pressure acceleration due to density gradients being more sensitive. Both accelerations increase with increasing sail side length. The differences between the two accelerations are shown in Figure 42. Values where the drag acceleration dominates over the solar radiation pressure force are shown in black. This study indicates that the solar sail must be deployed at an altitude of at least 350 km.

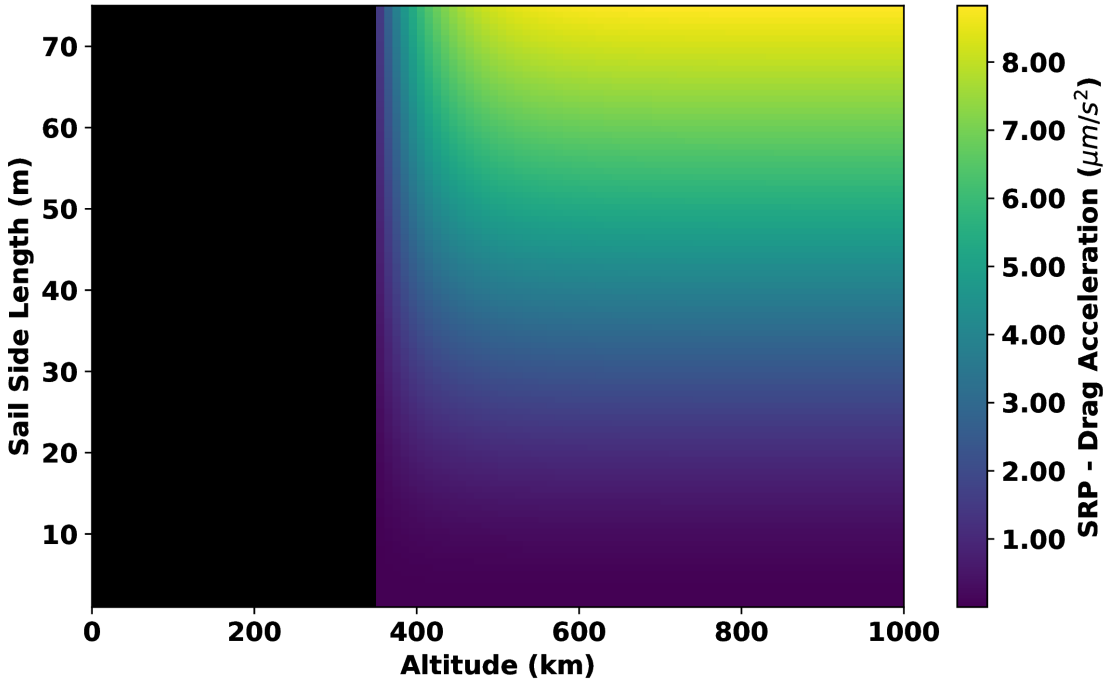

Figure 42: Heatmap of the difference between drag and solar radiation pressure accelerations as a function of solar sail side length (assuming square sails) and the sail deployment altitudes above the surface of the Earth. Values where the drag exceeds the SRP acceleration are shown in black. An absolute minimum deployment altitude of 350 km is set by this analysis.

3.4.3 Initial Orbits

Initial orbits are generated using the launch data described in Section 3.1. Launch site and C_3 data are randomly sampled to generate Low Earth or Geostationary Transfer Orbits, depending on the C_3. The launch site location dictates the inclination of the orbit. Orbits are generated in a geocentric frame and state vectors are converted from to a barycentric frame centered on the Earth-Sun

barycenter by adding the Earth's position vector and velocity relative to the barycenter similarly to the velocity calculations in Sec 3.4.2. Once in the barycentric frame, the states are rotated into the rotating frame using the direction cosine matrices defined in Section 3.2.

3.4.4 Energy Gain Control Law

Once an individual spacecraft is injected onto an initial Earth-centered orbit, it must use solar sail propulsion to assemble near the Sun-Earth L2. To ease the computation of the trajectory to L2 using this low-thrust propulsion, the transfer can be initiated after increasing the energy of the orbit either past the Earth escape energy or enough to match the Jacobi constant of the targeted periodic or quasi-periodic orbit at L2. A control law for energy maximization is incorporated as in [52, 53, 46] but in the Circular Three Body Problem. The control law is found through the same optimization of

$$\max_{\hat{\mathbf{n}}} \ \mathbf{a}_S \cdot {}^{S}\mathbf{v}, \tag{75}$$

finding the direction of the normal sail vector needed to maximize the projection of the solar radiation pressure acceleration on the velocity of the spacecraft, though the velocity is projected onto the Sun frame S. The optimization is solved as a constrained parameter optimization problem with the Hamiltonian

$$H = \beta \frac{1-\mu}{r_1^2} (\hat{\mathbf{r}}_1 \cdot \hat{\mathbf{n}})^2 \hat{\mathbf{n}} \cdot \vec{\mathbf{v}} + \lambda (\hat{\mathbf{n}} \cdot \hat{\mathbf{n}} - 1) \tag{76}$$

where a Lagrange multiplier is added for the constraint that the normal sail vector must be of unit length. The optimal pointing of the normal vector is found through

$$\frac{\partial H}{\partial \hat{\mathbf{n}}} = \mathbf{0} \tag{77}$$

which leads to

$$\begin{aligned} n_x &= \frac{|v_y|}{\sqrt{v_y^2 + \xi^2 (v_y^2 + v_z^2)}}, \\ n_y &= \xi n_x, \quad \text{and} \\ n_z &= \frac{v_z}{v_y} n_y \end{aligned} \tag{78}$$

where

$$\xi = \frac{-3 v_x v_y \pm v_y \sqrt{9 v_x^2 + 8 (v_y^2 + v_z^2)}}{4 (v_y^2 + v_z^2)}. \tag{79}$$

Taking the positive sign in the ξ definition leads to an energy gain trajectory while the negative sign leads to energy loss; a sample energy gain trajectory is shown in Figure 43 as a function of time.

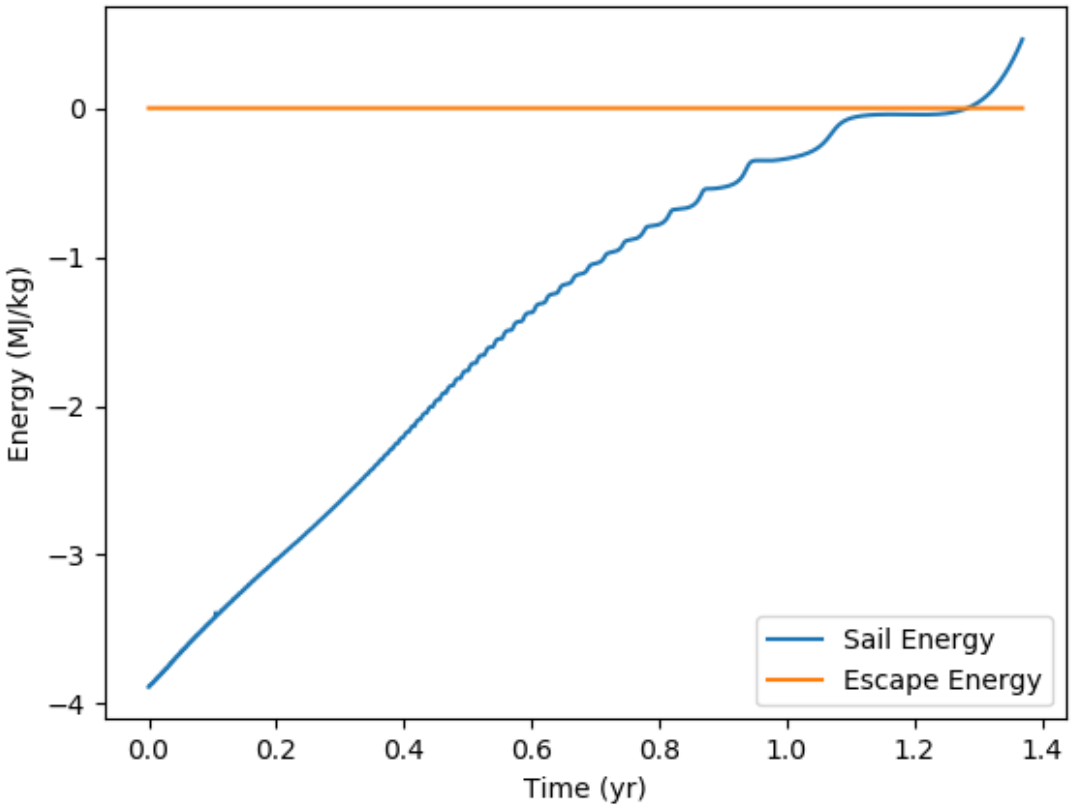

Figure 43: Energy of a sample Earth escape trajectory using a solar sail energy gain control law. Earth escape energy is also plotted for reference.

3.4.5 Escape Time as a Design Metric

The time to escape the Earth, or at least reach an appropriate Jacobi constant, can be used as a metric for measuring the performance of the solar sail. The optimal direction of the normal sail vector is known as a function of the spacecraft state vector; replacing this formula in the equations of motion allows us to integrate this as an initial value problem (IVP). An event function is introduced to terminate the integration after the Jacobi constant reaches the equivalent value at L2.

Simulations of Earth escape trajectories were conducted by seeding random initial Earth-centered orbits as explained in Sec 3.4.3 and "unfurling" the solar sail by solving an IVP with the terminating event that the Earth escape energy in the inertial frame is reached. The β values were varied for these orbits; 200 simulations were conducted. The results are presented in Figure 44, showing an inverse relation between β and escape time.

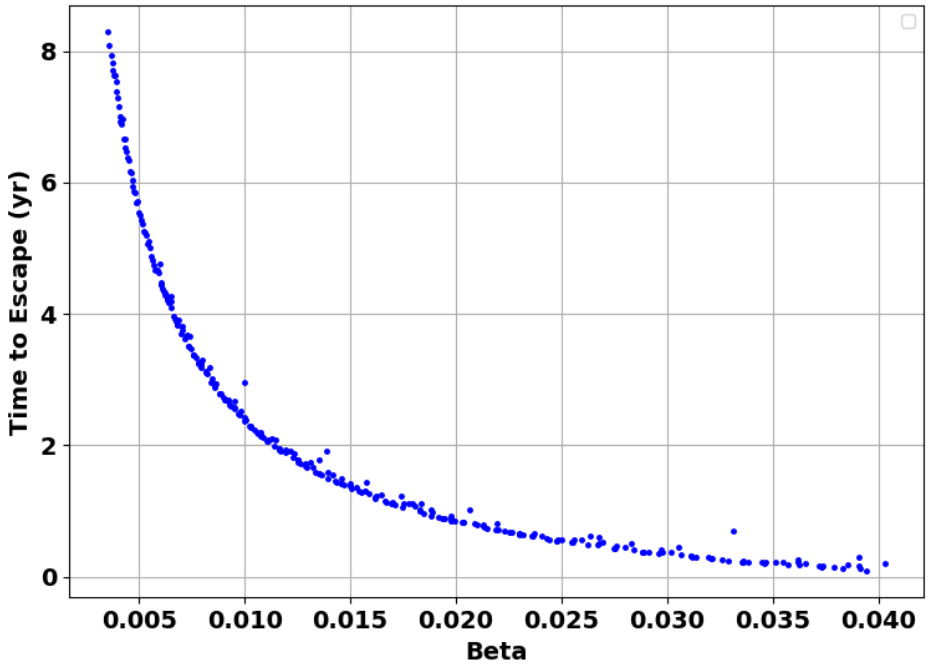

Figure 44: Escape times are plotted for 200 simulations of Earth escape trajectories with varying β values.

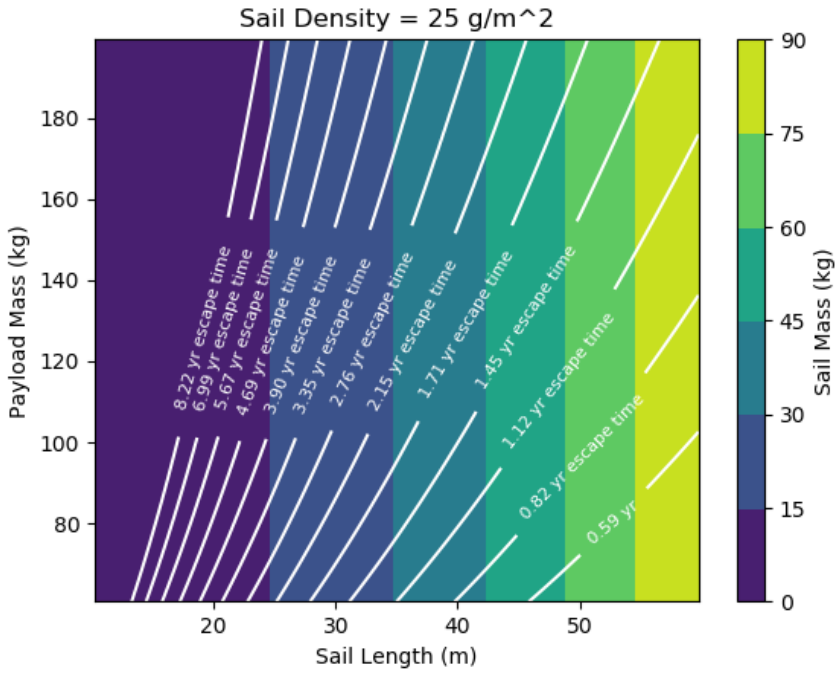

*Figure 45: Heatmap of the corresponding sail mass are plotted for ranges of payload masses and sail side lengths given a fixed sail density of 25*g/m^2*. Contours are created for the corresponding β values on the heatmap and are labeled with the resulting Earth escape times.*

As mentioned in Sec 3.4.1, the β values can be parameterized using the payload mass, sail area and sail density. A visualization of the parameter space for the sail loading is shown in Figure 45. Sail density is assumed a constant (value of $25g/m^2$) while payload mass and sail length are varied in the 2D plot. The corresponding sail mass is shown in the color scale. Each point on the grid corresponds to a β value and, from Figure 44, the β and escape time relationship is nearly one-to-one. Contour lines are drawn on the figure for escape times corresponding to the shown β value. Parameters can be chosen to target feasible escape times under 6 years, for example.

3.5 L2 Transfer

The solar sail solar radiation pressure can be framed as a low thrust propulsion method where the direction of thrust can be controlled and the maximum thrust capacity is constrained by the Sun's radiation at the location of the spacecraft. Low thrust trajectories are notoriously difficult to compute due to either poor initial guesses provided to optimal control methods or due to their winding nature. Trajectories are first found by assuming an unconstrained thruster on the spacecraft. Multiple techniques have been evaluated to solve the full solar sail BVP trajectories including shooting methods with a reformulation of the input controls (the direction of the sail normal), and are detailed below.

3.5.1 Optimal Control Theory

The trajectory from the Earth to L2 can be solved using optimal control theory [54, 55, 56], where a cost function is minimized in the interval $[t_0, t_F]$:

$$J = \phi(\mathbf{x}(t_F)) + \int_{t_0}^{t_F} L(t, \mathbf{x}, \mathbf{u}) dt \tag{80}$$

It is dependent on the states **x** and the control input **u**. The optimization is subject to the constraints of the equations of motion

$$\dot{\mathbf{x}} = \mathbf{f}(t, \mathbf{x}, \mathbf{u}), \tag{81}$$

initial conditions

$$\mathbf{x}(t_0) = \mathbf{x}_0, \tag{82}$$

and a terminal cost of

$$\psi(t_F) = 0. \tag{83}$$

To solve the constrained optimization problem, a Hamiltonian is defined

$$H(t, \mathbf{x}, \mathbf{u}, \lambda) = L(t, \mathbf{x}, \mathbf{u}) + \lambda^T \mathbf{f}(t, \mathbf{x}, \mathbf{u}). \tag{84}$$

The state vector is therefore augmented with the Lagrange multipliers of the control Hamiltonian. The number of equations of motion are augmented as well with

$$\dot{\lambda} = -\left(\frac{\partial H(t, \mathbf{x}, \mathbf{u}, \lambda)}{\partial \mathbf{x}} \right)^T. \tag{85}$$

Pontryagin's Maximum Principle says that the optimal control law is found by solving

$$\frac{\partial H(t, \mathbf{x}, \mathbf{u}, \lambda)}{\partial \mathbf{u}} = \mathbf{0}. \tag{86}$$

3.5.2 Optimal Control with an Unconstrained Thruster

Optimal control theory is applied for the case of an unconstrained thruster [55]. The control inputs are the three-directions of the thrust vector

$$\mathbf{u} = u_1 \hat{\mathbf{x}} + u_2 \hat{\mathbf{y}} + u_3 \hat{\mathbf{z}}. \tag{87}$$

The control effort of the thruster is minimized with the cost function

$$J = \int_{t_0}^{t_F} \frac{1}{2} \mathbf{u} \cdot \mathbf{u} dt \tag{88}$$

and the Hamiltonian becomes

$$H(t, \mathbf{x}, \mathbf{u}, \lambda) = \frac{1}{2} \mathbf{u} \cdot \mathbf{u} + \lambda^T \mathbf{f}(t, \mathbf{x}, \mathbf{u}). \tag{89}$$

Solving Eq. 86 results in the control law

$$\begin{aligned} u_1 &= -\lambda_4, \\ u_2 &= -\lambda_5, \\ u_3 &= -\lambda_6 \end{aligned} \tag{90}$$

Boundary conditions include

$$\begin{pmatrix} \mathbf{x}(t_0) - \mathbf{x}_0 \\ \mathbf{x}(t_F) - \mathbf{x}_F \end{pmatrix} = \mathbf{0}. \tag{91}$$

where the initial conditions $\mathbf{x}_0$ are somewhere on a seeded Earth-centered orbit and the final conditions $\mathbf{x}_F$ are either on a Lissajous orbit or somewhere on the invariant manifold of a Vertical Lyapunov orbit. The BVP is solved using a collocation method implemented in the `scipy` package.

Figure 46 shows a sample trajectory for a single spacecraft. It begins on an Earth escape trajectory and once it reaches the Jacobi constant of the Sun-Earth L2, it transfers to the Lissajous orbit. All phases of the trajectory are shown in the figure. The direction of the thrust can be decomposed into a pitch and clock angle similar to the definition of the solar radiation pressure was for the solar sail. The control history is shown in Figure 47.

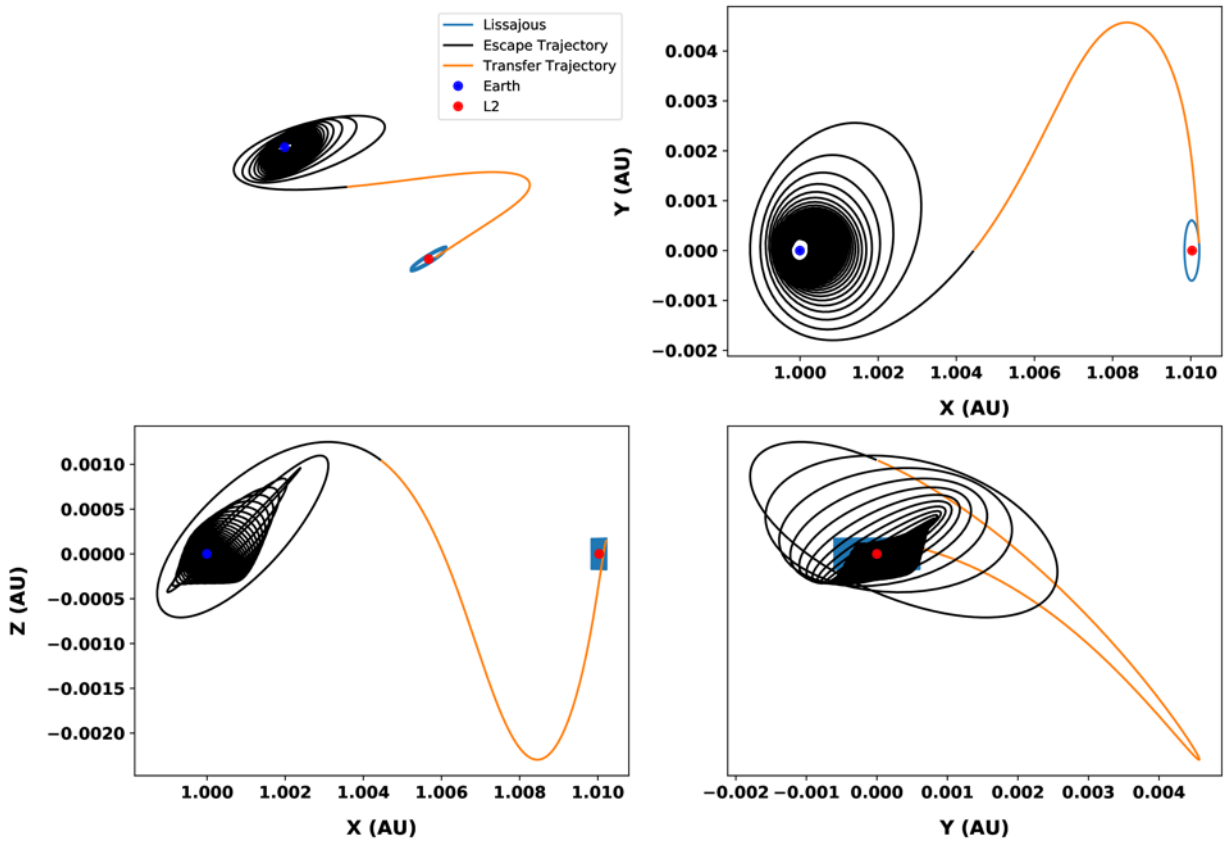

Figure 46: Different views of a full transfer from an Earth orbit to an L2 Lissajous by using an Earth escape solar sail control law to reach a comparable energy to the Lissajous, then using a collocation method with an unconstrained thruster model to inject the spacecraft into the Lissajous.

A full mission simulation was run for a subset of 15 spacecraft as shown in Figure 48. With a β value of 0.03, the average time to inject onto a Lissajous is approximately 1.23 years. If assuming a payload mass of 150kg, this would require a sail side length of approximately 35m.

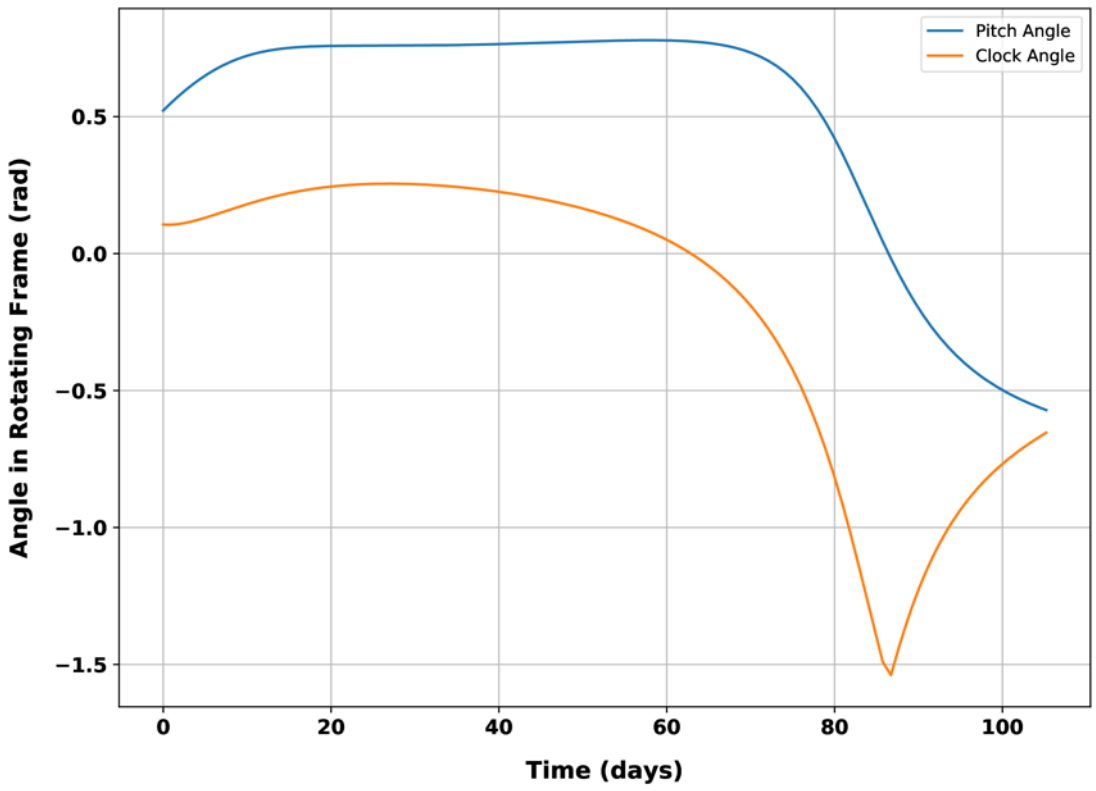

Figure 47: Thruster pointing angles decomposed into a pitch and clock angle similar to those defined for the solar sail.

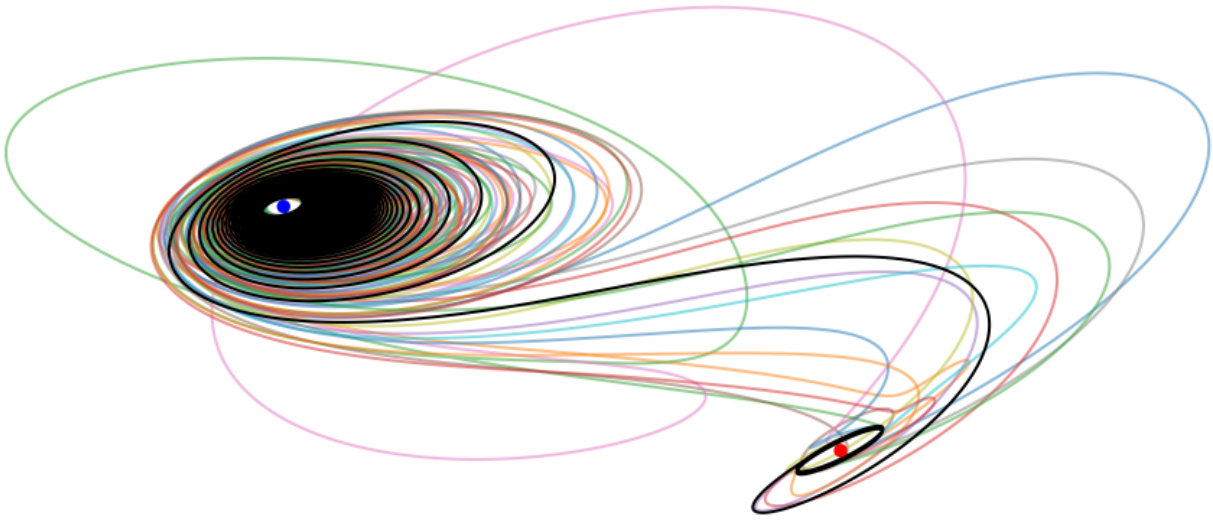

Figure 48: Mock-up of a full mission simulation with 15 spacecraft injected into different parts of the Lissajous orbit.

3.5.3 Optimal Control with a Solar Sail

Optimal control theory is applied for the case of solar sail propulsion [57, 58, 48]. The control inputs are the pitch and clock angles defined in Sec 3.4.1. The time of flight is minimized with the cost function

$$J = \int_{t_0}^{t_F} dt \tag{92}$$

and the Hamiltonian becomes

$$H(t, \mathbf{x}, \mathbf{u}, \lambda) = 1 + \lambda^T \mathbf{f}(t, \mathbf{x}, \mathbf{u}). \tag{93}$$

Solving Eq. 86 results in the following minimization

$$\min_{\alpha,\delta} \ \mathbf{a}_S \cdot {}^{\mathcal{S}}\lambda_v, \tag{94}$$

where $S\boldsymbol{\lambda}_v$=[$\lambda_{4,S}$, $\lambda_{5,S}$, $\lambda_{6,S}$]^T rotated into the S frame defined in Sec 3.4.1 which can be written in terms of similar pitch and clock angles as

$${}^{\mathcal{S}}\lambda_v = \begin{bmatrix} \cos\bar{\alpha} \\ \sin\bar{\alpha}\cos\bar{\delta} \\ \sin\bar{\alpha}\sin\bar{\delta} \end{bmatrix}. \tag{95}$$

Taking derivatives with respect to the sail clock and pitch angles results in the following relationships [57]

$$\begin{aligned} \tan\delta &= \tan\bar{\delta} \\ \tan\alpha &= \frac{-3 + \sqrt{9 + 8\tan^2\bar{\alpha}}}{4\tan\bar{\alpha}} \end{aligned} \tag{96}$$

Boundary conditions include

$$\begin{pmatrix} \mathbf{x}(t_0) - \mathbf{x}_0 \\ \mathbf{x}(t_F) - \mathbf{x}_F \end{pmatrix} = \mathbf{0}. \tag{97}$$

where the initial conditions $\mathbf{x}_0$ are somewhere on a seeded Earth-centered orbit and the final conditions $\mathbf{x}_F$ are either on a Lissajous orbit or somewhere on the invariant manifold of a Vertical Lyapunov orbit. The Hamiltonian is zero at the end point due to the final time being a free parameter [54, 55]. It has been found that this method is incredibly sensitive to the initial guess of the Lagrange multipliers and given the assumed sail loading values will not converge, in general, either by a collocation nor a shooting method for any arbitrary initial conditions.

3.5.4 Stable Manifolds of Periodic Orbits

Transfers to L2 are facilitated by targeting the invariant manifold corresponding to a periodic orbit; these manifolds extend to near Earth orbit and, once a spacecraft is injected into the manifold, can carry them to L2. An invariant manifold of a Vertical Lyapunov is found by calculating the state transition matrix $\boldsymbol{\Phi}(T,t_0)$ where T is the period of the orbit. The 6×6 square matrix has six eigenvalues [36]:

$$\lambda_1 > 1$$
$$\lambda_2 = \frac{1}{\lambda_1}$$
$$\lambda_3 = \lambda_4 = 1$$
$$\lambda_5 = \bar{\lambda}_6 \ , \ |\lambda_5| = 1. \qquad (98)$$

The first two eigenvalues correspond to unstable and stable behavior, respectively. Their corresponding eigenvectors are used to find the invariant manifolds extending towards Earth. A state on the periodic orbit $\mathbf{x}_0^P$ can be offset from the periodic orbit along the direction of one of these eigenvectors and integrated forwards or backwards through time to create the desired trajectory. The new initial state of the unstable manifold, for instance, is

$$\mathbf{x}_0^{\mathcal{U}}(\mathbf{x}_0^P) = \mathbf{x}_0^P + \epsilon Y^{\mathcal{U}}(\mathbf{x}_0^P) \qquad (99)$$

where ε is a sufficiently small number to produce the necessary manifold (on the order of 200 km is sufficient), and Y^U is the unstable eigenvector. A subset of trajectories within the invariant manifold is shown in Figure 49. From the integration, it is noted that a trajectory starting from the closest manifold point to Earth and ending near the vertical Lyapunov has a flight time of approximately 90 days.

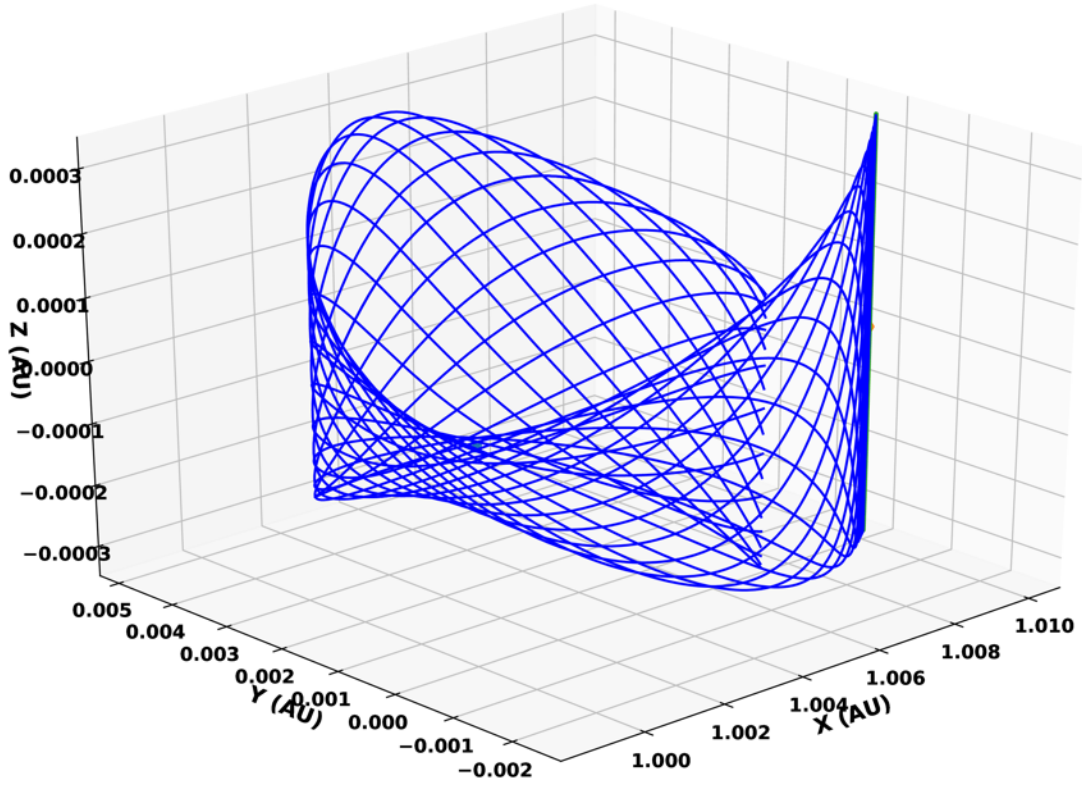

Figure 49: A subset of the Vertical Lyapunov invariant manifold, shown in the rotating frame, found by integrating the unstable eigenvector of the monodromy matrix backwards in time.

3.5.5 Targeting the Manifold

As the collocation method did not provide good performance when applied to a solar sail propulsion method we developed an alternate approach based on a single shooting method. Initial conditions are set for the trajectory and integrated forwards in time. A control history is generated before the integration and used for the sail normal pointing throughout the integration time. The spacecraft ends at some final state at the end of the integration which is most certainly not equal to the desired final state. The integration is therefore wrapped within an optimization problem where the norm of the difference between the desired and final state is minimized.

The final targeted state is some state on the invariant manifold of the Vertical Lyapunov orbit. We select this final boundary conditions because the manifold weaves through the rotating frame near the Earth's location in position space. If the spacecraft can inject itself onto the manifold, it can ride out to L2 where it can inject itself more easily onto the Lissajous orbit.

The initial state is selected as somewhere on the Earth escape trajectory. The spacecraft will switch from using an energy maximization control law for the sail pointing vector and commit onto some more refined controls to target the manifold. Because there is some sinusoidal behavior in the pointing angles, the new controls for the clock and pitch angles can be modeled as a Fourier Series [59]

$$\alpha = \frac{1}{2}a_0 + \sum_{n=1}^{\infty} a_n \cos\left(\frac{2\pi nt}{T}\right) + \sum_{n=1}^{\infty} b_n \sin\left(\frac{2\pi nt}{T}\right),$$

$$\delta = \frac{1}{2}c_0 + \sum_{n=1}^{\infty} c_n \cos\left(\frac{2\pi nt}{T}\right) + \sum_{n=1}^{\infty} d_n \sin\left(\frac{2\pi nt}{T}\right)$$

with Fourier coefficients a_n,b_n for the pitch angle and c_n,d_n for the clock angle. By using the Fourier coefficients (up to a certain N) as the optimization variables, the trajectory can be modified from the looping Earth escape trajectory to target the manifold. Initial guesses for the Fourier coefficients can be found by decomposing the actual control history for the angles from the escape trajectory. This is done by conducting a real Fast Fourier Transform on the data and normalizing by the number of data points. The optimization variables are summed up within the set

$$\mathbf{w} = [\ w_\alpha\ ,\ w_\delta\ ]^T = [\ a_0,\ a_1,\ b_1,\ \ldots,\ a_n,\ b_n,\ c_0,\ c_1,\ d_1,\ \ldots,\ c_n,\ d_n\ ]^T \qquad (100)$$

which has a size K=4N+2: N coefficients for each sine and cosine term for both angles, then two more for a_0 and c_0. Partial derivatives are taken with respect to time and also the coefficients themselves for use in constructing the gradient of the objective function. These partial derivatives are demonstrated relative to one of the Fourier series (α) first:

$$\frac{\partial \alpha}{\partial t} = -\sum_{n=1}^{N} a_n \left(\frac{2\pi n}{T}\right) \sin\left(\frac{2\pi nt}{T}\right) + \sum_{n=1}^{N} b_n \left(\frac{2\pi n}{T}\right) \cos\left(\frac{2\pi nt}{T}\right) \qquad (101)$$

and

$$\frac{\partial \alpha}{\partial w_k} = \begin{cases} \frac{1}{2} & k = 0 \\ \cos\left(\frac{2\pi nt}{T}\right) & k = 1, 3, \ldots, 2n \\ \sin\left(\frac{2\pi nt}{T}\right) & k = 2, 4, \ldots, 2n+1 \end{cases} \qquad (102)$$

Integration is conducted using Eq. 65, where the pointing angles of the solar sail normal vector are calculated from the Fourier Series approximation at each integration step. An event is introduced to the IVP which terminates the integration when the state of the spacecraft reaches the Jacobi constant of the Invariant Manifold. This is labeled as $\mathbf{x}^*$. The closest point on the manifold is found from the state $\mathbf{x}^*$ both in position and velocity space; this state on the manifold is labeled $\mathbf{x}_m$. The optimization is therefore written as

$$\min_{\mathbf{w}} \; J. \tag{103}$$

where

$$J = ||\mathbf{x}^* - \mathbf{x}_m||^2 = (x^* - x_m)^2 + (y^* - y_m)^2 + (z^* - z_m)^2 + (\dot{x}^* - \dot{x}_m)^2 + (\dot{y}^* - \dot{y}_m)^2 + (\dot{z}^* - \dot{z}_m)^2 \tag{104}$$

Calculating a gradient vector for the objective function speeds up the optimization process by bypassing an additional function call for each variable; instead the gradient can be an output of the same objective function. The gradient is calculated as

$$\nabla_{\mathbf{w}} J = \left[\frac{\partial J}{\partial w_0}, \ldots, \frac{\partial J}{\partial w_K} \right]. \tag{105}$$

It can also be reconstructed using the chain rule, one term of which could look like

$$\frac{\partial J}{\partial x^*} \frac{\partial x^*}{\partial t} \frac{\partial t}{\partial \alpha} \frac{\partial \alpha}{\partial w_k}. \tag{106}$$

The full partial derivative relative to a single value of **w** is written as

$$\frac{\partial J}{\partial w_k} = (\nabla_{\mathbf{x}^*} J \cdot \dot{\mathbf{x}}^*) \left(\frac{\partial w_k}{\partial t} \right)^{-1} \tag{107}$$

where

$$\nabla_{\mathbf{x}^*} = \left[\frac{\partial}{\partial x^*}, \frac{\partial}{\partial y^*}, \frac{\partial}{\partial z^*}, \frac{\partial}{\partial \dot{x}^*}, \frac{\partial}{\partial \dot{y}^*}, \frac{\partial}{\partial \dot{z}^*} \right] \tag{108}$$

evaluated at the termination due to the event t_e,

$$\dot{\mathbf{x}}^* = \mathbf{f}(t_e, \mathbf{x}^*, \mathbf{u}_F^*) \tag{109}$$

are the evaluated equations of motion using the Fourier approximations of the input angles, $\mathbf{u}_F^*$, and

$$\left(\frac{\partial w_k}{\partial t} \right)^{-1} = \frac{\partial u_k}{\partial w_k} \frac{\partial t}{\partial u_k} \tag{110}$$

whose derivatives are applied to the Fourier Series formula. Work on this method is ongoing and current implementations have not yet produced consistent results that allow for injection into the manifold from any arbitrary initial conditions. The method is also still fairly computationally

expensive. We are currently exploring the use of a more robust optimizer such as SNOPT [60] and working to reformulate the gradient function.

Enough work, however, has been conducted to show the basic feasibility of the orbital solution and to make approximations for the total assembly time. The time to inject the sailcraft into the manifold from Earth orbit should be on the same order as the total Earth escape time. The transfer from the manifold near Earth towards L2 is nearly a constant, approximately 90 days. The rendezvous times can be calculated as shown in the following section.

3.6 Rendezvous

Analysis of module rendezvous is motivated by the need to determine which maneuvers can be accomplished with solar sails. The first step in rendezvous analysis was identifying the phasing of modules such that a close approach would be induced. To do this, a discretized Lissajous orbit was simulated for 50 years to capture the full quasi-periodic behavior of the orbit.

With this orbit created, the distance between each point on the orbit, and every other point, was calculated in order to identify all locations on the orbit that had a close approach, where two modules would come within 1000 km of one other. Points within +/- 30 days of a given point on the orbit were ignored for this part of the analysis, to prevent close approaches from being identified in immediately adjacent parts of the Lissajous orbit.

This analysis showed that close approaches would be induced if modules were phased by 177.5 days on the orbit. This means that if a module is randomly placed on the Lissajous orbit, it will have a close approach with a module placed 177.5 days ahead of it on the orbit, or 177.5 days behind it. For the following rendezvous simulations, modules were placed near where close approaches were identified, to reduce the amount of the trajectory that needed to be simulated.

Once two modules were appropriately placed on the lissajous orbit, they were assigned roles. One was arbitrarily designated as the leader, which would move passively on the Lissajous orbit, and the other was designated as the follower, which uses control to match the leader's position and velocity. The first attempt at developing rendezvous trajectories involved modeling the propulsion system as an unconstrained thruster, capable of producing arbitrary thrust in an arbitrary direction, with no change in the module's mass, as described above. Following the same optimal control approach as described in the previous section, with a cost function minimizing control input, trajectories and control inputs were generated, with the time to rendezvous set to 1.45 days.

These trajectories and control inputs were used as the initial guess for the multiple shooting method, which was used to solve for the trajectories and control input for a module with a constrained solar sail. Additionally, the multiple shooting method was set to minimize time to rendezvous, and used Eq. 111 as the cost function to minimize. Here, t_0 is the time at close approach, and t_f is the time at rendezvous. In contrast to the unconstrained thruster optimal control solution, this method set the time at rendezvous, t_f, as a free parameter, to be updated every iteration along with the positions and velocities at each segment. Since the position and velocity of the lead satellite at rendezvous is a function of t_f, these values were updated as final time changed, requiring the terminal constraint equation to be updated every iteration. The terminal constraint can be seen in Eq. 112. Here, $\mathbf{x_1}(t_f)$ and $\dot{\mathbf{x}}_\mathbf{1}(t_f)$ are the position and velocity of the lead satellite at t_f. $\mathbf{x_2}(t_f)$ and $\dot{\mathbf{x}}_\mathbf{2}(t_f)$ are the position and velocity of the follower at the final time.

$$L = \int_{t_0}^{tf} dt \tag{111}$$

$$\begin{bmatrix} \mathbf{x_1}(t_f) - \mathbf{x_2}(t_f) \\ \dot{\mathbf{x}}_\mathbf{1}(t_f) - \dot{\mathbf{x}}_\mathbf{2}(t_f) \end{bmatrix} = \mathbf{0} \tag{112}$$

Rendezvous were generated throughout the Lissajous trajectory, to ensure the solar sail was capable of producing a rendezvous trajectory regardless of the direction of the initial and final velocity, as this varies greatly depending on the location on the Lissajous orbit.

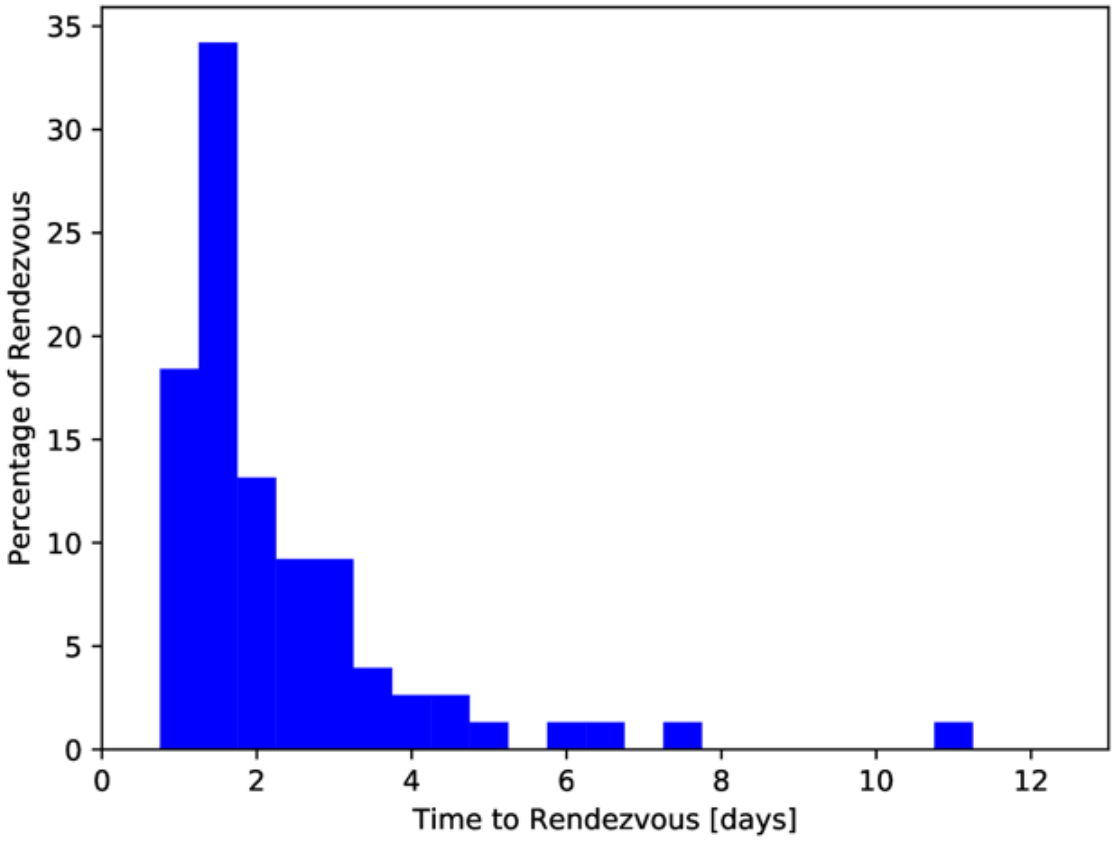

Figure 50: Histogram of the time to rendezvous (in days from initial contact at 1000 km separation) for modules using constrained solar sail propulsion. The majority of rendezvous events last between 1.5 and 2 days.

One hundred rendezvous were simulated; a histogram of the time to rendezvous for these simulations can be seen in Figure 50. This indicates that modules can rendezvous regardless of their position on the orbit. A peak is identified for final times between 1.5 days and 2 days. The multiple shooting algorithm is not deterministic; increasing the number iterations for each rendezvous increases the chances of identifying the true minimum time trajectory. However, the majority of the rendezvous events simulated have a time to rendezvous greater than the initial guess of 1.45, so it is reasonable to assume that this is close to the true minimum time to rendezvous for

most of the simulated events, as no rendezvous events were found to have a time to rendezvous of less than one day.

3.7 Docking

Analysis of the docking procedure is required how larger groups of modules should rendezvous. The concept of operations calls for the assembly of clusters of modules, which will then rendezvous with one another for the final assembly of the primary mirror.

The first step in assessing docking is to identify how many modules should be in a cluster before it switches to the final assembly mode of operation. It is desirable to have a low number of "precision docking events", where a module needs to navigate to a specific location on a cluster. However, it is necessary for some number of precision docking events to take place, to prevent vacant positions from being surrounded and made inaccessible, and to ensure the correct final mirror shape is created.

Additionally, it is desirable for docking events to occur on docking sites where the vacant position is adjacent to three modules. When three modules are adjacent to a docking site, the incoming trajectory can be anywhere within a 60 degree arc, allowing for some error in the incoming module's trajectory. If four modules are adjacent to a docking site, there is only one allowable approach direction, allowing for no error in the approach trajectory. This can be seen in Figure 51.

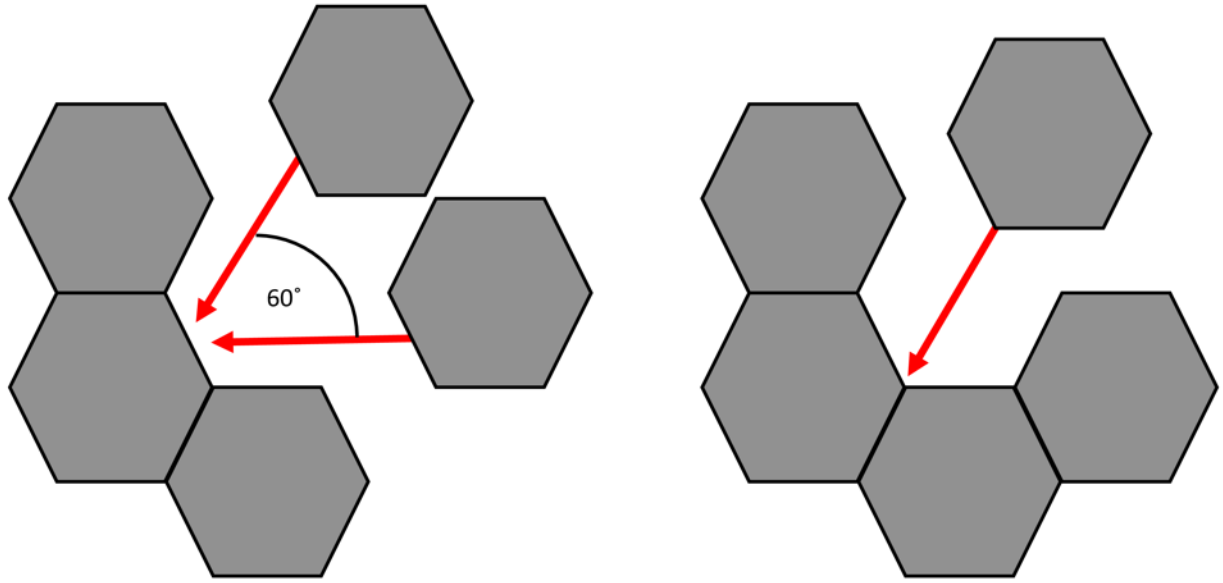

Figure 51: Top view of modules docking in two configurations. In the configuration on the left, an incoming module's trajectory may be anywhere within a 60 degree arc. However, in the configuration on the right, an incoming module only has one available trajectory.

These conditions produce a simple docking scheme, where modules are allowed to randomly add themselves to any available docking site on a cluster, unless there is a docking site that is adjacent to three modules. In that case, a precision docking maneuver must take place, where the incoming module must dock at the site with three adjacent modules.

Figure 52 shows a cluster growing using this scheme. Each frame shows the state after 5 modules have been added. This docking scheme, while simple, prevents difficult docking situations, while still allowing some modules to dock to at random sites.

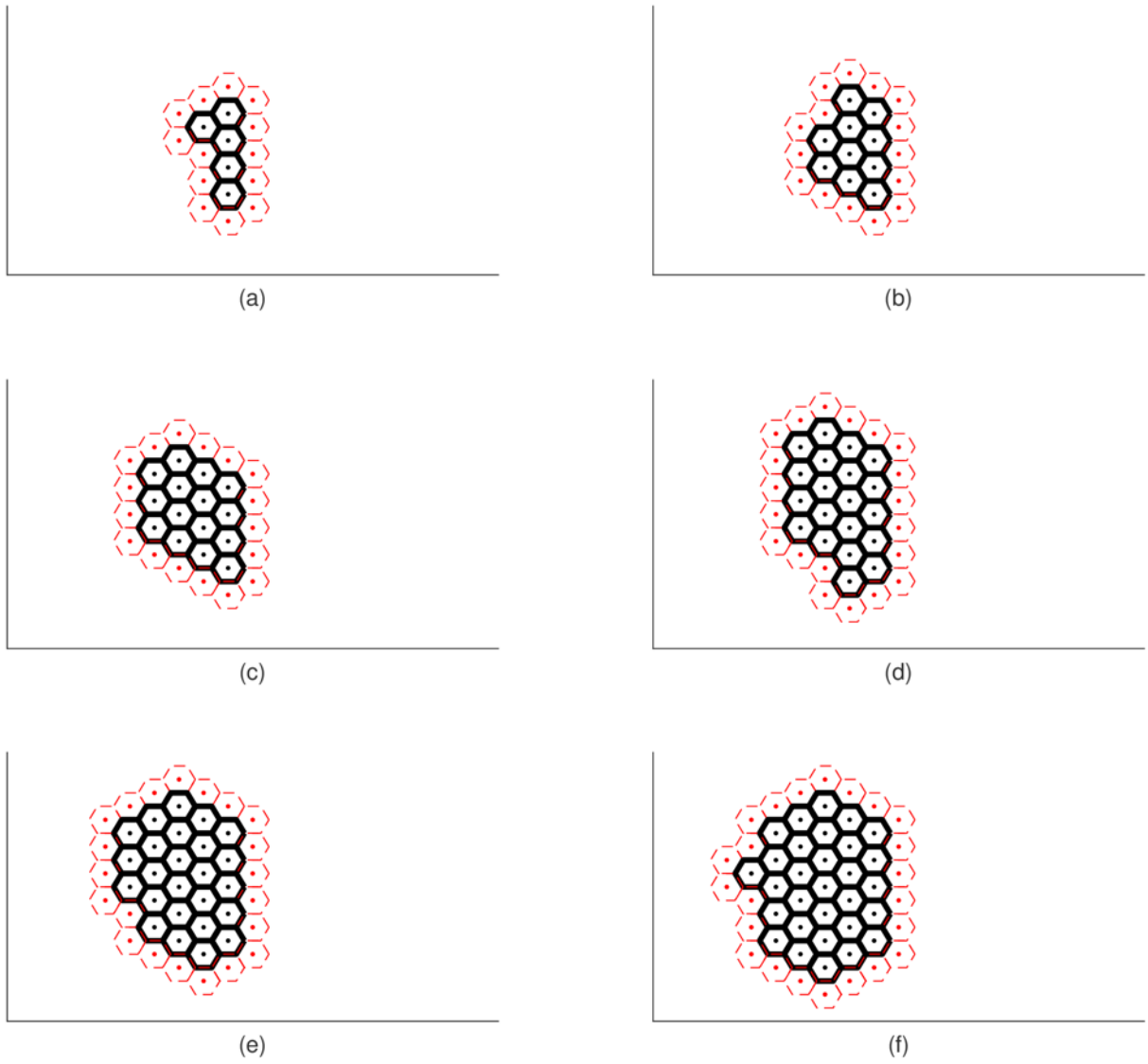

Figure 52: Top views of growing clusters of modules. Frame (a) shows the cluster after the first five modules have docked, and frames (b) through (f) show the state sequentially, with five modules docking in between each frame. The black hexagons represent docked modules, and the red dashed hexagons represent the available docking sites.

4 MODULE DESIGN

The final component of the Phase I work was a limited exploration of the design space for the module spacecraft, including the definition of the design bounds, and a detailed exploration of the subsystem components for our nominal point design.

4.1 Sizing Analyses

An analysis of launch vehicle (LV) configurations is motivated by the need to maximize the number of modules fit into a given number and type of launch vehicles within the spare payload mass of individual launches. In section 3.1, we established a projected number of launches per year and concluded 7 years of launches was sufficient to deliver the required number of modules. While the total module mass requirement is satisfied, we must include LV stack structural support for a specific allocation of modules per LV and also decide how we would allocate them per vehicle. Based on an analysis of currently available packaging options, we selected variations of MOOG's configurable EELV Secondary Payload Adapter (ESPA) [61] ring for our LV stack structural support. This section also presents different configuration options and associated constraints on the module design.

Table 4: Historical launches of ESPA rings on various Launch Vehicles from MOOG's ESPA User Guide [62].

Mission	**Launch Vehicle**	**Carrier**	**ESPA Type**	**Launch Date**
STP-1	Atlas V	ESPA	6-15-24	March 2007
LCROSS	Atlas V	Propulsive ESPA	6-15-24	June 2009
OG2 Mission 1	Falcon 9	ESPA Grande (2)	4-24-42	July 2014
AFSPC-4	Delta IV	ESPA	6-15-24	July 2014
OG2 Mission 2	Falcon 9	ESPA Grande (3)	4-24-42	December 2015
AFSPC-6	Delta IV	ESPA	6-15-24	August 2016
SHERPA Spaceflight	Falcon 9	ESPA Grande	5-24-42	Planned 2017 (canceled)
EAGLE - AFRL	Atlas V	Propulsive ESPA	2-15-24-4PT	April 2018
SSO-A Spaceflight	Falcon 9	ESPA	6-15-24	December 2018
STP-2 (DSX Mission) AFRL	Falcon Heavy	ESPA	4-15-24	Planned 2019
LDPE (STP-3) SMC/AD	Atlas V	Propulsive ESPA	0-15-24-4PT	Planned 2019

This section omits excessively custom launch vehicle stack structural support options on the basis of constraining costs and the challenges associated with integration to each primary payload stack as well as details of specific configuration/packaging. This work does not investigate any configurations resulting in an offset center of gravity (CG) of the LV payload or concepts that do not scale to an arbitrary number of modules. We did not investigate the single mounting of modules to an LV or any kind of custom-structure (e.g. modules with corner-to-corner equal to fairing diameter and vertically mounted above one another).

Our first constraint on module top-down footprint size are any of the launch vehicle fairing dimensions. From the LV capacity analysis in section 3.1, we see the Atlas V and Falcon 9 are the current launch vehicle types with sufficient excess payload capacity so our LV-payload structural

interface, module configuration, and module design must be compatible with these vehicles. MOOG's ESPA is one such common spare payload interface which has been used on many launch vehicles including the Atlas V and Falcon 9 as shown in Table 4. Of note is MOOG's ability to produce at least 2 ESPA rings within 1 year (there will be scaling challenges when this demand is increased to an annual average of $23 \approx \frac{804 modules}{5\ per\ ESPA \times 7 yrs}$). By adopting ESPA rings as our LV-payload interface structure, we minimize additional testing, analysis, and mitigate risk to primary payloads.

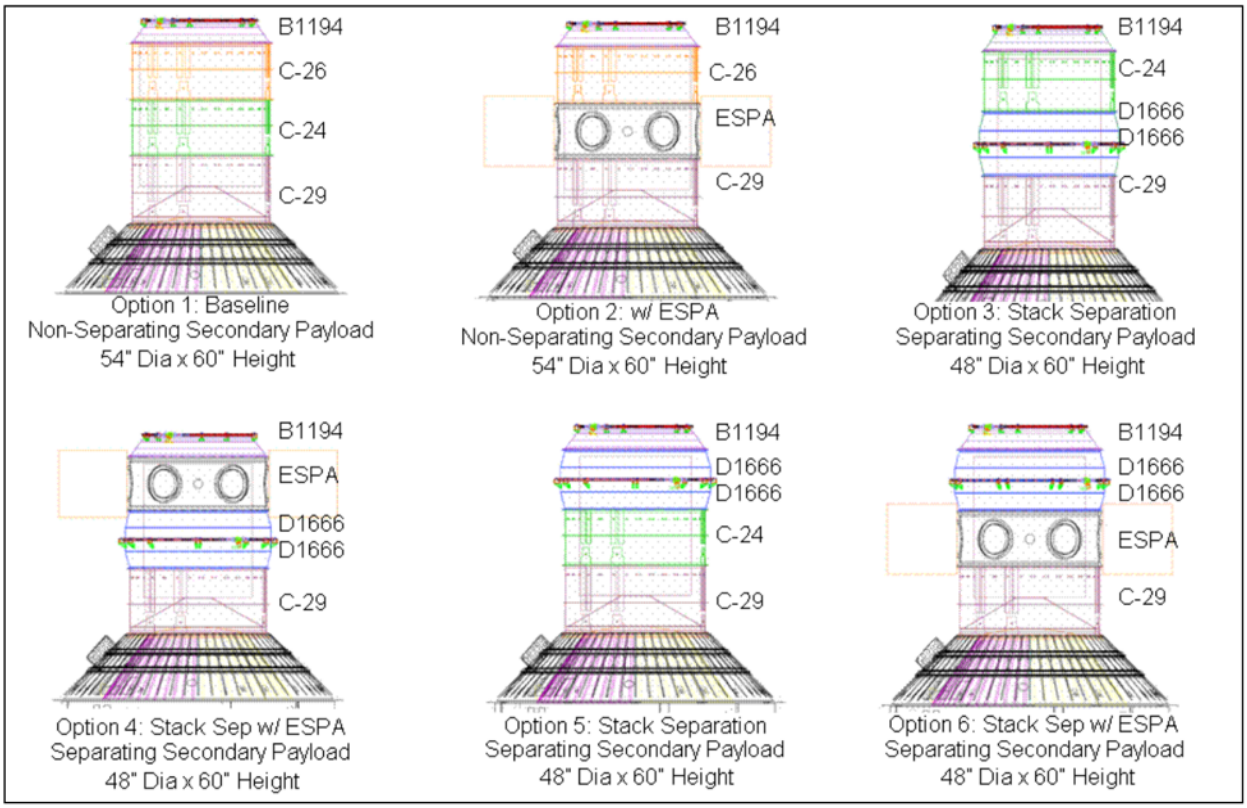

Figure 53: United Launch Alliance Launch Vehicle Configurations of C-Adapters and ESPA rings [63].

Figure 53 shows how an ESPA ring can be mounted onto a launch vehicle (in this case a Delta IV) with modules radially mounted to the ESPA ring at each circular port via C-adapters (a common upper stage adapter option fitting various launch vehicles). The ESPA rings are highly modifiable, but we will limit our analysis to the configurations mentioned explicitly in the ESPA User Guide [62]. The ESPA ring has a combination of integer and continuous variables describing the design; STANDARD, HEAVY, and GRANDE describe 3 of these combinations as listed in Table 5. The only design parameters not included in Table 5 are the ESPA ring's mass as a function of ring height included in Figure 55 and the maximum payload CG distance from the mounting point on the ring in Figure 56. The absolute maximum height of an ESPA ring is 60". If additional height is needed for spacing between segments and the payload, C-Adapters can be added as seen in Figure 53. It is important to note the number of ports represents a maximum and ESPA ring mass is relatively invariant when the number of ports is changed [62]. Each ESPA ring's major

diameter connecting the ring to the rest of the bus is set by the EELV interface with diameter 61.01" (1.5496 m) [64, 65].

Table 5: Table of possible ESPA ring configurations. Z represents a maximum radial distance outwards from the mounting point on the ESPA ring, X represents the nominal width limit in the radial dimension, Y represents the maximum height of the spacecraft on the minimum height ESPA ring. [62]

ESPA Type	Port Size	Max # Ports	Fairing	X (m)	Y (m)	Z (m)
STANDARD	15"	6	4m	0.6096	0.7112	0.9652
STANDARD	15"	6	5m	0.6096	0.7112	0.9652
HEAVY	15"	6	4m	1.0668	1.1684	0.9652
HEAVY	15"	6	5m	1.0668	1.1684	1.4224
HEAVY	24"	5	4m	1.0668	1.1684	0.9652
HEAVY	24"	5	5m	1.0668	1.1684	1.4224
GRANDE	24"	5	4m	1.0668	1.1684	0.9652
GRANDE	24"	5	5m	1.0668	1.1684	1.4224

Combining the limits provided for both 4 m and 5 m fairings, as well as the size of the ESPA ring and the bounding boxes, we can set top-down view geometric constraints that define the physical bounding box space of each module as shown in Figure 54. While it may appear modules exceed box sizes, the radial limits of a module are only set when each secondary payload is different, and do not apply in the case of our identical modules filling a ring. The actual limits are the bounding box necessary to satisfy vibration analysis.

From the ESPA User's Guide [62], we can derive a parametric equation for the ESPA ring mass including Figure 55 to determine the ESPA ring mass as a function of module height. To calculate the number of segments that can be fit on a particular launch vehicle, we need to know the mass of a fully loaded ESPA ring which can be calculated using Eq. 114. From this, we can derive the total number of segments that can be added as

$$N(m_s, m_{ESPA}, P_m) = n_{\max} * \left\lfloor \frac{P_m}{m_{FL}} \right\rfloor + \lfloor P_m \% m_{FL} / m_s \rfloor * m_s + m_{ESPA}.,, \tag{113}$$

where m_s is the mass of an individual segment/module, n_max is the maximum number of modules that can be loaded on that particular ESPA type according to Table 5, m_{ESPA} is the mass of an individual ESPA ring (assuming a nominal 1.5m module height), N is the number of segments, P_m is the total payload mass available and m_{FL} is the mass of a fully loaded ESPA ring, given by

$$m_{FL}(m_s, m_{ESPA}, n_{\max}) = m_s * n_{\max} + m_{ESPA}\,. \tag{114}$$

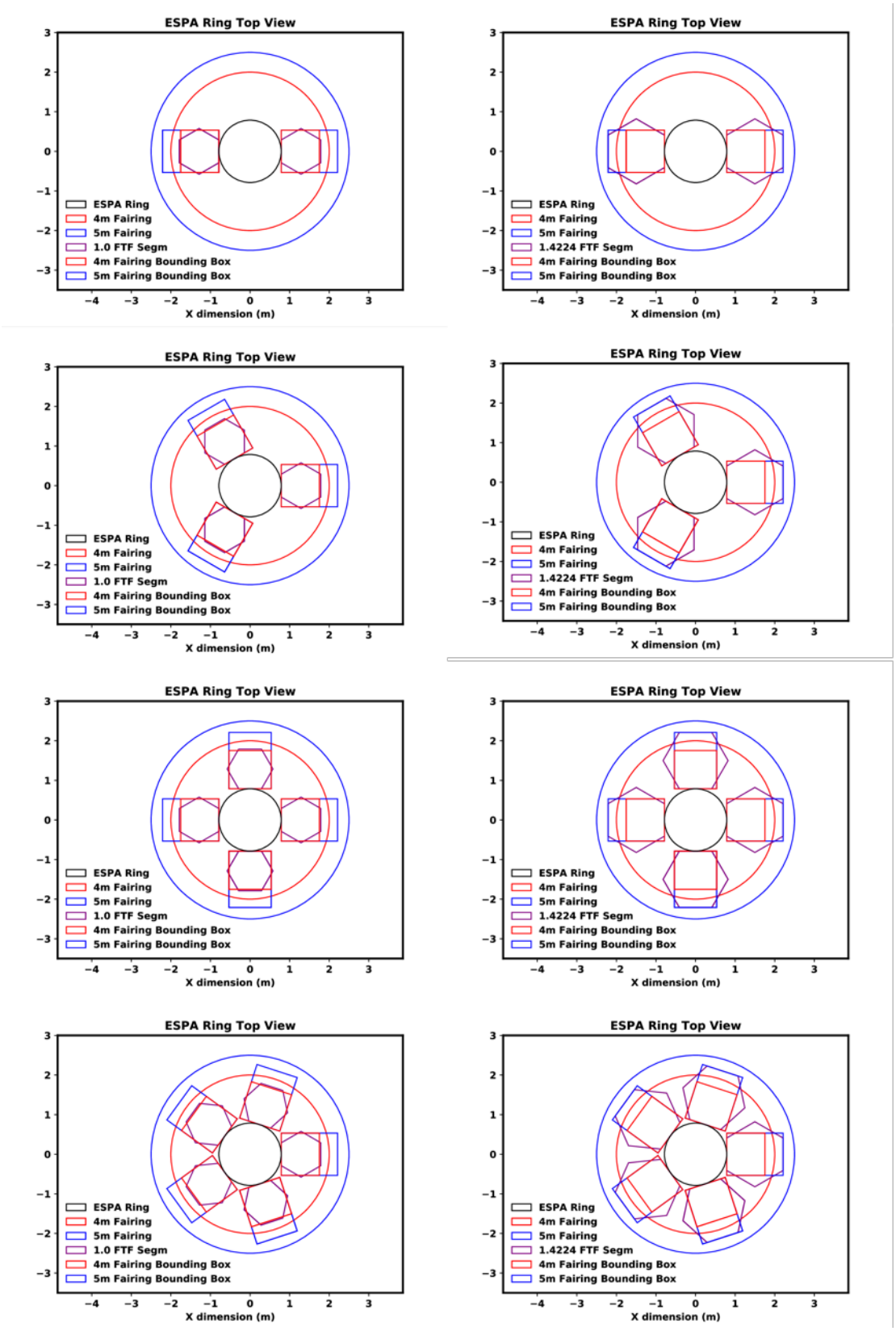

Figure 54: Launch Vehicle Configurations and nominal bounding boxes

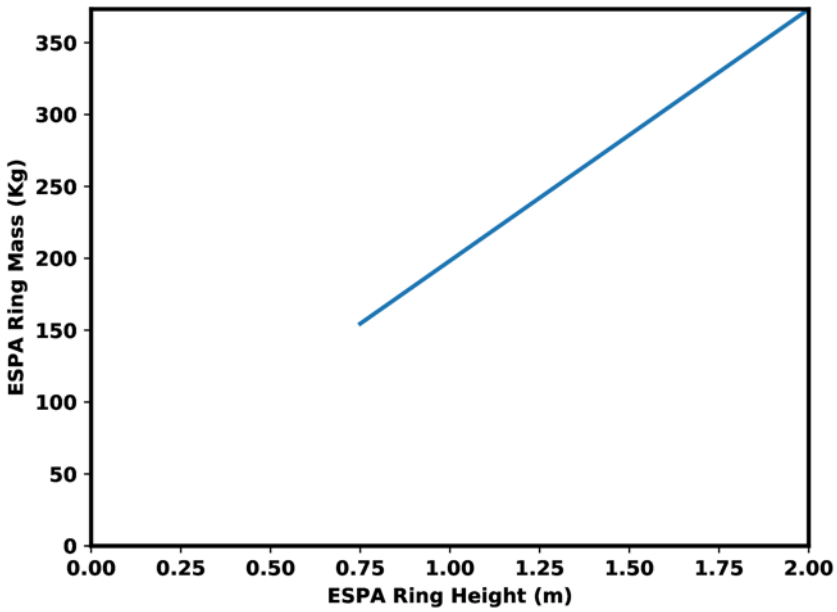

Figure 55: ESPA mass vs ring height based off data in [62].

Note that there is an additional condition on Eq. 113 that assumes there is enough mass for 1 more segment and 1 more ESPA ring. For a set of launch vehicles and spare payloads generated from section 3.1, we can calculate exactly how many ESPA rings and how many modules can fit onto that particular launch vehicle.

Table 6: Using the method described in Section 3.1, we simulate spare payloads and distribute as many 150Kg segments into the launch vehicles

Spare Payload (kg)	**Sum ESPA Mass** (kg)	# **ESPA**	**sum Seg. Mass** (kg)	# **Seg.**
675	210	1	450	3
1100	210	1	750	5
1475	420	2	1050	7
1900	420	2	1350	9
2870	630	3	2100	14
3092	630	3	2250	15
3610	840	4	2700	18

While these calculations demonstrate mission feasibility from a launch vehicle configuration and mass perspective, they place additional constraints on the module design. The loosest constraint among these is:

Constraint 1 The module mirror top surface corner-to-corner distance shall not exceed LV fairing major diameter.

The more restrictive constraint we impose in order to minimize mass spent on structural interfaces with the rocket is:

Constraint 2 Module flat-to-flat size shall not exceed Z as defined in Table 5.

To mitigate the possibility of contamination of the mirror surface before or during launch, we require:

Constraint 3 The module mirror surface shall face antipodes the direction of LV thrust during launch.

Constraint 4 The angle between nominal module mirror surface normal vector and and nominal Earth gravity vector shall not exceed 90deg.

Based on recommendations from the engineers at MOOG [personal communication (2018)] we require:

Constraint 5 Module shall structurally connect to the ESPA ring via a Planetary Systems Lightband.

Finally, we require that the maximum segment mass that can be loaded using an ESPA ring for a module with center of gravity (CG) distance from ESPA ring bolt circle of 0.5m to be 700Kg:

Constraint 6 Module center of gravity distance from ESPA ring mounting bold circle (ESPA bolt circle) shall not exceed the distance specified in Figure 56.

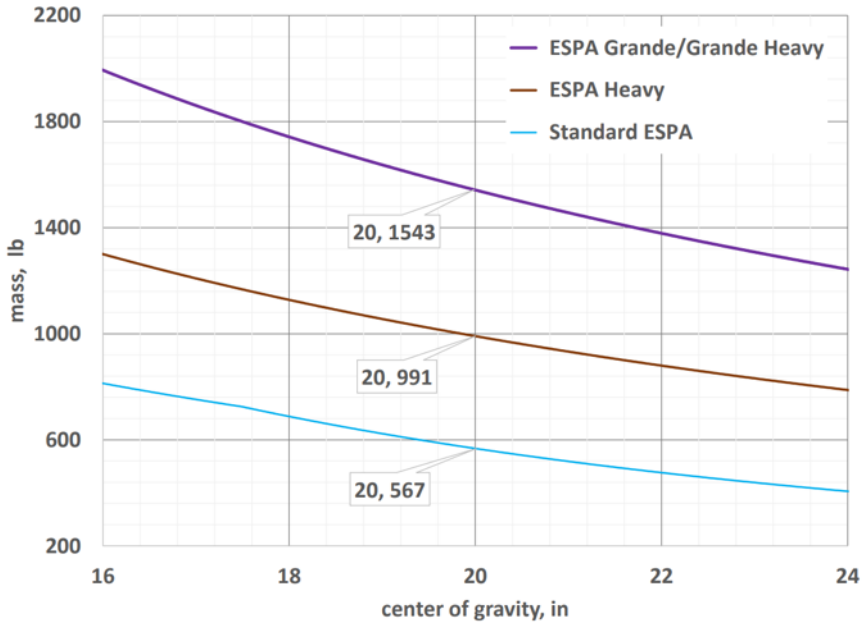

Figure 56: ESPA maximum segment mass vs segment center of gravity distance from ESPA mounting point. From [62].

4.2 Preliminary Subsystem Analysis

In this section we report on our non-comprehensive list of (potential) components for the module design and produce a current best estimate (CBE) for spacecraft mass. For the trajectory modeling sections of this report, we assume a total module mass of 150Kg + 35m sail ≈180.625*Kg* for the total spacecraft mass. We additionally assume a 1 m mirror flat-to-flat dimension. We enumerate a list of all spacecraft components in Table 7.

Table 7: List of required spacecraft components and approximate masses

Component Name	**Quantity**	**Mass Per Unit**
Mirror [19]	1	13.509 kg
Solar Sail Sub-system	1	30.625 kg
Cryo-Actuators [33]	127	0.655 k g per, 85kg total
Cryo-Actuator cabling	254 @3m	0.015 kg/cable, 3.81 kg total
Delta Frame	1	-
Stewart Platform (linear actuators 24") [66]	6	2.26 kg per, 13.55 kg total
Electra Transceiver [67]	1	4.9 kg
Star Tracker	3	-
IMU	1	-
Reaction Wheels	4	-
Lightband [68]	1	4.05 kg
Delta Frame/Lightband Stiffener	1	-
Docking Structure	1	-
Battery [69]	1	35.2 kg
Docking Mechanisms	6	-
Roll Out Solar Array	< 1	-
Fixed Solar Cells	> 1	-
RAD 750 Computer + ~20 motor drivers + Power Distribution Board	1	< 20 kg
Resistive Heating Elements	?	
Deployable Radiator	?	?
Microthruster solenoids	10	« 1 kg
Cold Gas Propellant Tank	?	-
Inter-spacecraft Cabling	18	0.6183 kg total

Since we modeled the mirrors based on the JWST mirror segments and retained the rib structure as well as the original mirror thickness, we can use the areal density of the JWST mirror (ϱ_{mirror}=15.6kg/m^2) for our mass scaling factor [19]. We use the geometric relationship to define mirror mass as a function of mirror flat-to-flat (d) as

$$m_{mirror} = \frac{3d^2}{2}\rho_{mirror}\tan(30°). \tag{115}$$

Evaluating this at d=1 m yields a mirror (only) mass of 13.509 kg.

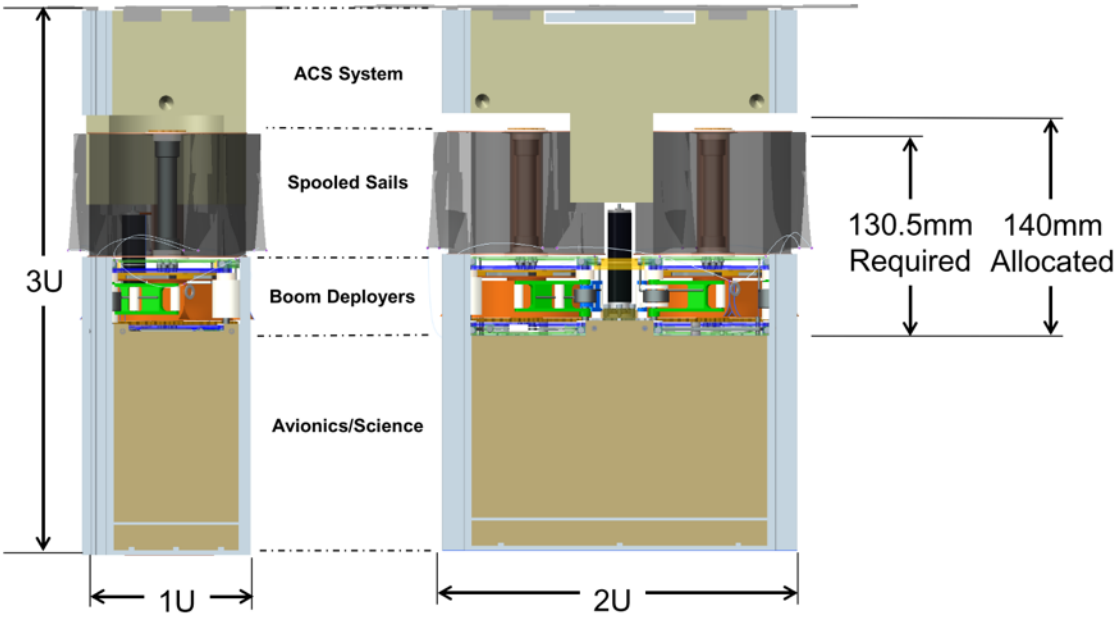

Figure 57: NEA Scout 12U Cubesat Deployment Mechanism Dimensions. From [70].

To estimate our solar sail mass and packaging size, we perform a scaling of the NEA Scout system, shown in Figure 57. Essentially, the NEA Scout solar sail has an area of $80m^2$ and mass of approximately 2Kg resulting in an areal density of approximately $25g/m^2$ which would include the deployment mechanism mass [71]. This is in line with heritage solar sails but represents a conservative estimate for the state of the art since the deployment mechanism should not scale with area. NEA Scout's solar sail is made of aluminized CP-1 with an areal density of ~ 6 g/m^2 at 2.5 μm thickness, which shows we have a mass margin of up to 76%. The advantage of using with the CP-1 sail material is that it has undergone ife testing through by exposing it to the 3 year and 6 year equivalent radiation dosage of the Solar Polar Imager and was subsequently tensile tested. CP-1 maintained strength and 50% the original ductility following radiation exposure [72, 71]. However, future solar sails could be manufactured using Mylar reinforced with Kevlar at intervals of 2.54 cm, which can have an areal density of 3 g/m^2 with a thickness of 2.5 μm [73]. Using the current NEA Scout parameters, we arrive at an estimated mass relationship

$$m_{sail} = \rho_s A_{sail}\,, \tag{116}$$

where ρ_s is the areal density of the sail, A_{sail} the area, and m_{sail} is the sail mass. Using our point design of a solar sail with $35m$ side length, we get a sail area of 1225 m^2 and arrive at a sail mass of 30.625 kg.

For deforming the mirror, we selected Ball Aerospace's cryogenic actuators, since they were the only actuators we could find capable of operating at cryogenic temperatures as shown in Table 8 and they will have flight heritage from JWST [33]. Cryogenic operation is crucial for these actuators in order to minimize time to achieve thermal stability following a mirror surface figure correction. These actuators also have a sufficient motion range to account for slop in the Stewart platform positioning. The primary concern with these actuators is their mass. If we have 127

actuators on the mirror backplane, then at 0.665 kg per actuator assembly, these actuators alone would be 85 kg. This motivates further investigation of how to reduce residual error at the edges of the mirror to achieve the desired surface figure, as well as continued development of lower mass actuators that can directly impart low spatial frequency modes across the whole mirror surface.

Table 8: Ball Aerospace Cryogenic Actuators [33]

Property	JWST Requirement	Capability
Fine range	<7 μm	10 μm
Fine step size	<10 nm	7.7 nm
Fine repeatability	<3 nm	2 nm
Coarse range	>20 mm	21 mm
Coarse step size	<1.0 μm	0.058 μm
Axial load	1890 N	2650 N
Axial stiffness	24,500 N/mm	25,200 N/mm
Axial holding	380 N	890 N
Position feedback	20 μm	12 μm
Cryogenic operation	30 K	20 k
Nominal length	138.8 mm	138.8 mm
Mass	700 g	665 g

Since the Stewart platform extends by up to 1m and there are so many cryo-actuators, it makes sense to calculate their additional cabling mass. Assuming 20 AWG wire at 0.005 kg/m with a 3 m cable length from the power distributor to the actuators and accounting for return cabling, the harness would be ~ 3.81 kg. To date, there are no space qualified linear actuators with the large stroke lengths (~ 0.56 m) we require. The entire platform must extend upwards by at least 1m to accommodate the mirrors on the outer most edge of the primary. Further technology development will be needed to fill this gap.

Our limiting cases in terms of battery draw occur during deployment from the launch vehicle and during docking [69]. We do not yet have a good power use profile, so we assume a single 3300 Whr battery pack will be sufficient. We estimate that it should take less than one day to complete docking activities and so require that power usage be less than 137 W during this time. We have identified a commercial off the shelf (COTS) LiDAR package that uses 18W, our transmitter [67] uses 68W to transmit and 18W to receive, a single microthruster can consume 10 W, reaction wheels can use 10 W of power each, a single star tracker uses less than 8 W, and a RAD 750 processor consumes 10 W of power. In total, if everything were being used at once during docking, we could see power use as high as 260W. Applying some realistic duty cycling on the thrusters and transmitter, we can bring this number down to 77.5 W throughout an entire 24 hour docking process, meeting the stated requirement with margin.

We baseline the Electra transceiver which has heritage use on the Mars Reconnaissance Orbiter and many other deep space missions, so we will be able to stay in communication with each module on the way to and at L2. An alternative option which is slightly smaller and consumes slightly less power is the Sphynx-Iris combination but is not as robust. A picture of the Electra transciever is shown in Figure 58.

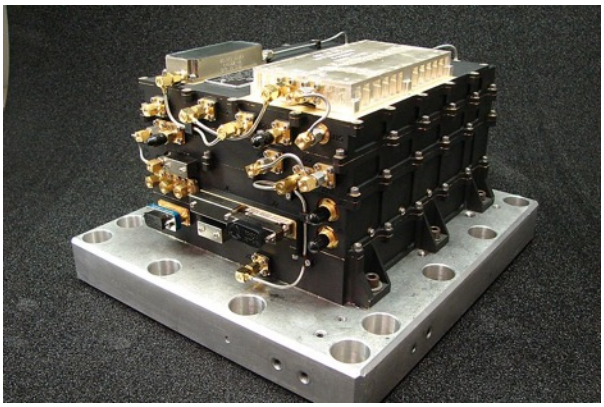

Figure 58: Electra Transceiver mass of 4.9Kg, size of 17.2cm (W) x 21.9cm (L) x 14.0cm (H) used aboard the Mars Reconnaissance Orbiter (MRO). Image Credit: NASA/JPL-Caltech.

Based on discussion with MOOG engineers, we have adopted the Planetary Systems Lightband for interface with the launch vehicle, which will serve as the electrical passthrough for communication of separation events and spacecraft wake up from the launch vehicle. The Lightband also mechanically propels the spacecraft away from the upper stage and provides a tumble state for the spacecraft, and is shown in Figure 59.

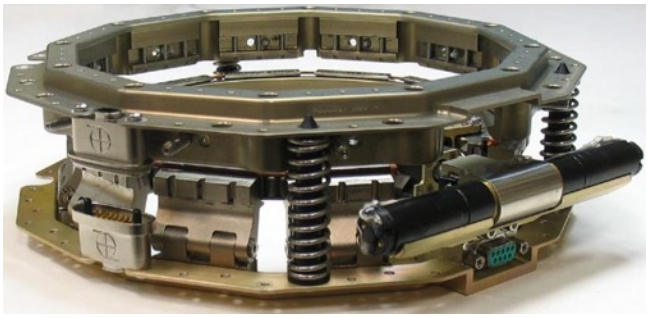

Figure 59: Motorized Lightband capable of interfacing with ESPA Grande. From [68].

Immediately upon release of the module from the launch vehicle, the spacecraft will begin operating on battery power in it's tumble state. To reduce mission risk, the best option is to add body mounted solar panels which ensure the spacecraft receives power even during a tumble state. For final assembled operations, the roll out solar array (ROSA) is capable of providing sufficient power for operations. The caveat is the high mass of the array and difficulty with arrays overlapping on final assembly, however, a single array can power multiple modules; incentivizing inter-module cabling. The ROSA array deployed on the ISS can be seen in Figure 60. The nominal dimensions of the version flight tested on the ISS were 1.7m wide by 5.4 m long. Vendors provided solar power modules which created a total power of 300 Watts during the flight demonstration, but these solar strings only constituted 10% of the total blanket area and the other 90% was filled with mass simulators [74]. A full array of this size and same make would supply 3000 Watts of power (`https://www.dss-space.com/`).

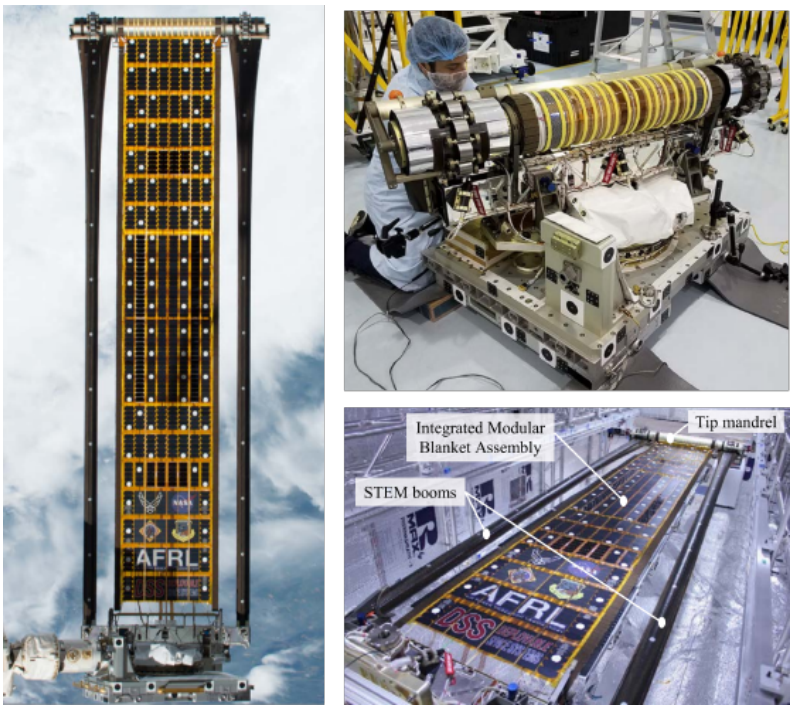

Figure 60: Roll-Out Solar Array. From: [74]. From top right in clockwise order: ROSA assembled in a clean room; Tip mandrel next to a man for scale; Deployed array mounted on the International Space Station Canada Arm.

Inter-module cabling is a unique opportunity represented by this mission. Since all modules will end up hard docked to one another, adding a universal bus to the electrical interface enables sharing of power, computer processing, power distribution, and motor controllers. The challenge of implementing this is the added complexity of new module addition events.

We baseline the standard RAD 750 processor, although newer processors are currently in development that would mature in time for this mission. Because there are so many actuators, and all actuators do not need to be activated at once, there is an open question of equipping individual motor controller cards for each actuator or multiplexing a larger collection of motor controllers.

The mass and design of the final spacecraft structure is challenging and is still in progress. The wavefront at two opposing extremums of the primary mirror must be within a wavelength of one another. This requirement means the physical hard-dock systems as well as the connected spacecraft structure acts as a bending beam with a sufficient stiffness to deflect less than a few nm across 30 m. In a similar fashion, the mirror and mirror actuators must have a high stiffness connection during launch and then be detached via some frangible bolts, or the Stewart platform actuators must have an extremely high stiffness and protection of their motors. Some of these requirements are alleviated by the prospect of continuous, active control of the whole structure, but the overall stability requirements on the structure remain difficult and require additional technology development. Based on all of the above, the current mass of the spacecraft is estimated at around 200Kg, but this omits spacecraft structure which typically accounts for ~ 30% of the total spacecraft mass. Technology development in multiple of the highlighted areas (and

particularly the actuators) will be required to meet the mass requirements imposed by the preceding mission analyses.

4.3 Preliminary Module Design

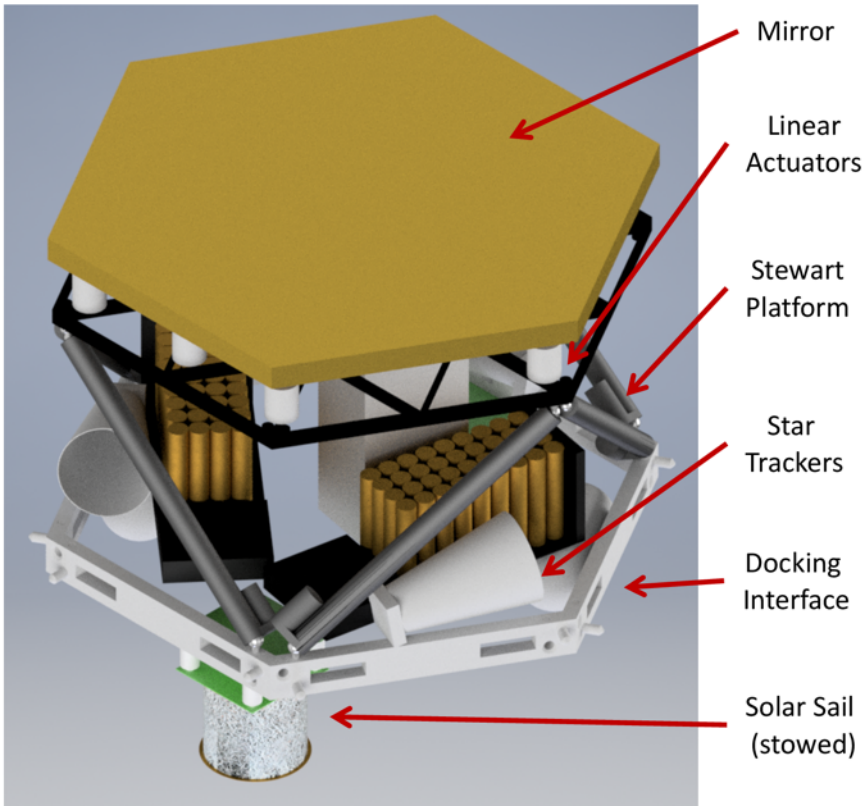

Figure 61: Preliminary module CAD with visible components labeled. The model shows the polished mirror, the Stewart platform upon which it is mounted and a subset of the linear actuators between the mirror and backplane. Also shown are the star trackers, the docking interface and a stowed solar sail.

The preliminary design of the module is shown in Figure 61. From top to bottom, the mirror is attached to a set of linear actuators that control the deformation of the mirror surface. These linear actuators rest on a rigid backplane, which itself is a Stewart platform which can control the tilt, tip, and piston of the mirror surface. Major spacecraft subcomponents are housed within the bus of the spacecraft, including star trackers, batteries, and flight computers. At the bottom of the spacecraft is a rigid hexagonal frame which provides a mechanical docking interface between modules. The solar sail is stowed in a cylindrical container at the bottom of the module.

4.4 Design Phase Space

Thus far, we have presented a single point design for this mission. However, there are many different module design options that can meet the requirements of our proposed self-assembling architecture. We have specifically identified two parameters that together parametrize mission

time, wavefront quality, and control complexity: solar sail side length and mirror size. Their relationship to the resultant parameters is shown in Figure 62.

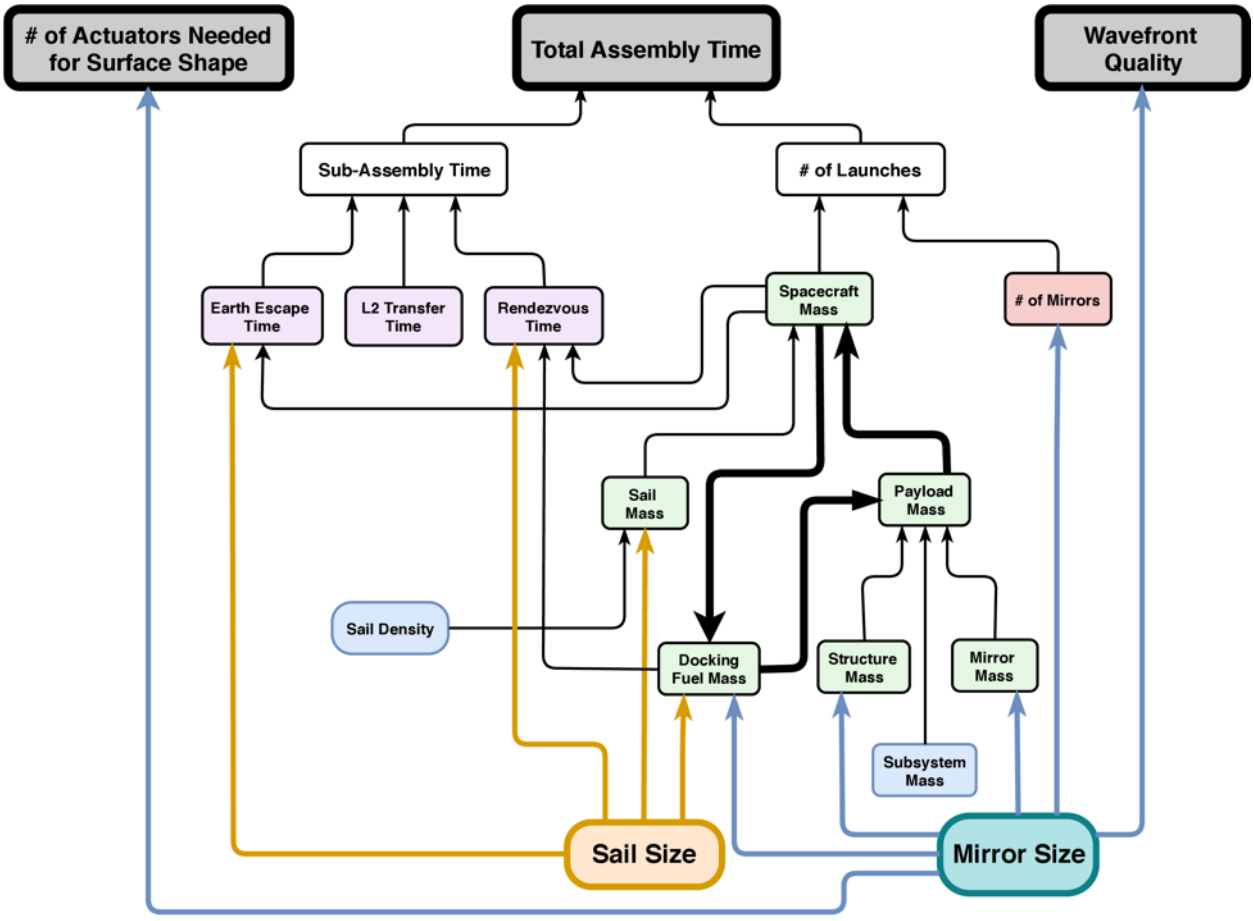

Figure 62: Flowchart of the final cost function and its dependencies on just two parameters: sail size and mirror size (all other quantities kept constant). From these two inputs, we can calculate the required number of mirror actuators, the resulting wavefront quality, and the total assembly time, including the transfer and rendezvous times. These inputs also trace directly to the required number of modules and the required number of launches.

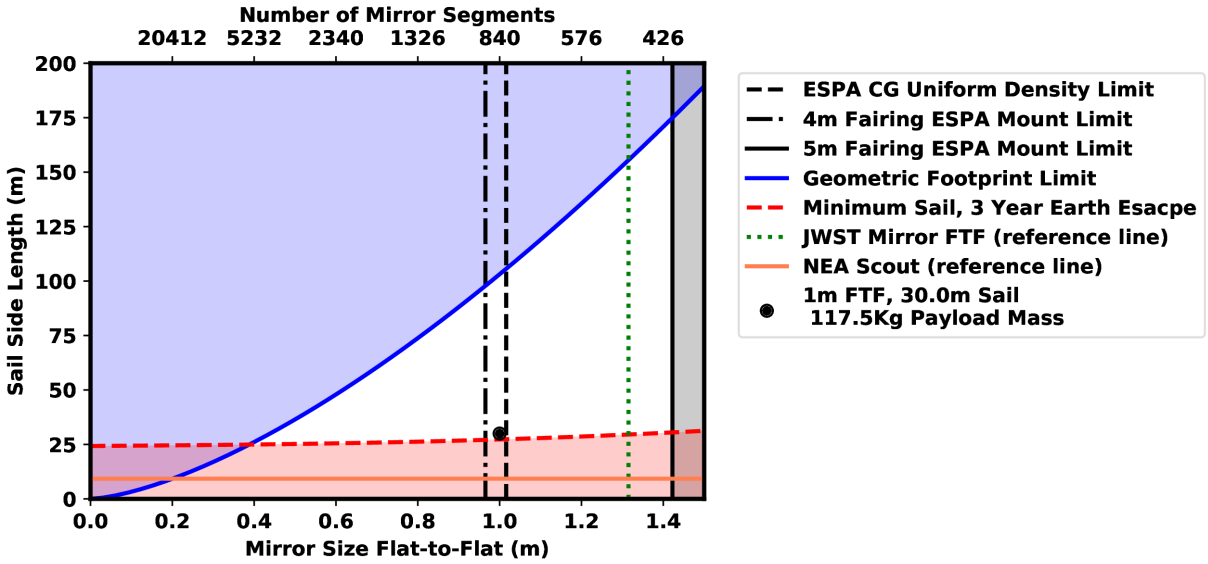

Figure 63: Design phase space between mirror size and sail size. Multiple limits on each of these parameters exist, and the resultant, optimal design must not lie in any of the shaded regions.

Additionally, we have identified limits on these variables. All designs must exist in a phase space defined by the limits in Figure 63. In order of appearance on the legend, more complete descriptions for each line are:

1. ESPA CG Uniform Density Limit: if the spacecraft mass is symmetrically distributed about the vertical axis (along the direction of reflection of the flat mirror), then this line represents the maximum mirror size that ensures the cg of the spacecraft is within the limiting distance from the docking port on the ESPA ring.

2. 4 m Fairing ESPA Mount Limit: Geometric constraints mean the mirror size must be less than this value should any launch vehicle we use have a 4 m diameter fairing.

3. 5 m Fairing ESPA Mount Limit: the same as above, but for launch vehicles with 5 m diameter fairings.

4. Geometric Footprint Limit: The stowed solar sail (in a cylinder) will have dimensions greater than that of the mirror, and will therefore be larger than the footprint of the mirror above this blue line, excluding that area.

5. Minimum Sail, 3 Year Earth Escape: This assumes a constant value of 85 kg of payload needed regardless of mirror size, and assumes the relationship between the increase in mass of the payload and the mirror size is known. Below this line, the solar sail is not large enough to achieve earth escape in under 3 years. The equation used for the payload mass is

$$m_p = 85 + 5f_m + d_m t_m a_m + 7.5(\frac{f_m}{1.315}) + 7.5, \qquad (117)$$

where m_p is the mass of the payload, f_m is the flat-to-flat distance of the mirror a_m is the mirror area, t_m is the mirror thickness, and d_m is the mirror density. The last 2 terms in the

expression represent a static and scaling component of the actuators required as well. This equation intersects with the known value for the weights of the mirror actuators for the James Webb Telescope.

6. The size of the mirrors on JWST (provided as reference only).
7. The size of the solar sail on a reference mission, NEA Scout (provided as reference only).
8. The single datapoint represents the point design we have identified for study in Phase I, with a particular sail size (30 m) and mirror size (1 m flat-to-flat) for the mission. It lies within the acceptable region based on the bounds of the other lines.

Beyond bounding the sail and mirror sizes, we can create surface plots of the three final parameters from Figure 62. If these are normalized and overlaid in the acceptable region of the design phase space, we can find a local minimum that will optimize the mirror size and sail size.

5 CONCLUSIONS AND FUTURE WORK

The Phase I study activities have successfully retired the primary risks to mission feasibility originally identified in the Phase I propsal, namely the ability to find orbital and optical solutions for the modular telescope architecutre. Therefore, we believe that we have successfully progressed the concept from TRL 1 to 2. That said, and as highlighted throughout this report, there remain many open questions and engineering challenges associated with progressing this concept to higher technology readiness levels, which merit additional study. In particular, the key focus must now turn from demonstrating basic feasibility to showing detailed implementation details for both the generalized calculation of all orbital solutions, and the specific actuation design that will allow individual mirror segments to assume their prescribed shapes to the required precisions. At the same time, there are many gaps in the current subsystem analyses that must be filled, and there is a pressing need to continued technology development in both solar sail materials and cryogenic mirror actuation in order to meet the mass and size requirements derived here.

Another key finding of the Phase I study is the level to which the required technology developments of this concept overlap with existing NASA technology roadmaps. Unsurprisingly, many of our technology fit directly within the technology plan and technology gap list of the NASA Exoplanet Exploration Program (ExEP)[2]. These technology needs are sourced from the community and well-integrated with program priorities, serving as the basis for program investment. Because our concept brings together many of the technologies required to build a large optical space telescope, but in a way that enables aperture scales well beyond those currently being considered by ExEP, many of the technology developments prioritized by ExEP are exactly those that will be needed to mature our concept. There are also extensive overlaps between our needs and the high priority technologies identified in NASA technology roadmaps TA4 (Robotics and Autonomous Systems) as well as TA8 (Science Instruments, Observatories, and Sensor Systems) and TA2 (In-Space Propulsion Technologies). This makes continued study of this concept highly synergistic with ongoing NASA activities, and means that future developments of our architecture will be cros-cutting and directly infuseable into other NASA programs.

[2] https://exoplanets.nasa.gov/exep/technology/gap-lists/

REFERENCES

[1] B. Macintosh, J. R. Graham, P. Ingraham, Q. Konopacky, C. Marois, M. Perrin, L. Poyneer, B. Bauman, T. Barman, A. S. Burrows, A. Cardwell, J. Chilcote, R. J. De Rosa, D. Dillon, R. Doyon, J. Dunn, D. Erikson, M. P. Fitzgerald, D. Gavel, S. Goodsell, M. Hartung, P. Hibon, P. Kalas, J. Larkin, J. Maire, F. Marchis, M. S. Marley, J. McBride, M. Millar-Blanchaer, K. Morzinski, A. Norton, B. R. Oppenheimer, D. Palmer, J. Patience, L. Pueyo, F. Rantakyro, N. Sadakuni, L. Saddlemyer, D. Savransky, A. Serio, R. Soummer, A. Sivaramakrishnan, I. Song, S. Thomas, J. K. Wallace, S. Wiktorowicz, and S. Wolff, "First light of the Gemini Planet Imager," *Proceedings of the National Academy of Sciences*, vol. 111, no. 35, pp. 12661–12666, 2014.

[2] G. H. Sanders, "The thirty meter telescope (tmt): An international observatory," *Journal of Astrophysics and Astronomy*, vol. 34, no. 2, pp. 81–86, 2013.

[3] C. Kouveliotou, E. Agol, N. Batalha, J. Bean, M. Bentz, N. Cornish, A. Dressler, E. Figueroa-Feliciano, S. Gaudi, O. Guyon, *et al.*, "Enduring quests daring visions," *NASA Technical Report (Dec. 2013)*, 2013.

[4] N. Rioux, H. Thronson, L. Feinberg, H. P. Stahl, D. Redding, A. Jones, J. Sturm, C. Collins, A. Liu, and M. Bolcar, "Future large-aperture uvoir space observatory: reference designs," *Journal of Astronomical Telescopes, Instruments, and Systems*, vol. 2, no. 4, pp. 041214–041214, 2016.

[5] D. A. Fischer, B. Peterson, LUVOIR Team, *et al.*, "The luvoir mission concept study interim report," *arXiv preprint arXiv:1809.09668*, 2018.

[6] Y. Fujii and H. Kawahara, "Mapping earth analogs from photometric variability: spin-orbit tomography for planets in inclined orbits," *The Astrophysical Journal*, vol. 755, no. 2, p. 101, 2012.

[7] R. K. Kopparapu, E. Hébrard, R. Belikov, N. M. Batalha, G. D. Mulders, C. Stark, D. Teal, S. Domagal-Goldman, and A. Mandell, "Exoplanet classification and yield estimates for direct imaging missions," *The Astrophysical Journal*, vol. 856, no. 2, p. 122, 2018.

[8] H. P. Stahl, T. M. Henrichs, A. Luedtke, and M. West, "Update to single-variable parametric cost models for space telescopes," *Optical Engineering*, vol. 52, no. 9, p. 091805, 2013.

[9] H. P. Stahl and T. Henrichs, "Multivariable parametric cost model for space and ground telescopes," in *Modeling, Systems Engineering, and Project Management for Astronomy VI*, vol. 9911, p. 99110L, International Society for Optics and Photonics, 2016.

[10] L. D. Feinberg, J. Budinoff, H. MacEwen, G. Matthews, and M. Postman, "Modular assembled space telescope," *Optical Engineering*, vol. 52, no. 9, pp. 091802–091802, 2013.

[11] D. W. Miller, S. Mohan, and J. Budinoff, "Assembly of a large modular optical telescope (almost)," The International Society for Optical Engineering, 2008.

[12] J. T. Dorsey, W. R. Doggett, R. A. Hafley, E. Komendera, N. Correll, and B. King, "An efficient and versatile means for assembling and manufacturing systems in space," in *AIAA Space 2012 Conference and Exposition*, 2012.

[13] N. N. Lee, J. W. Burdick, P. Backes, S. Pellegrino, K. Hogstrom, C. Fuller, B. Kennedy, J. Kim, R. Mukherjee, C. Seubert, *et al.*, "Architecture for in-space robotic assembly of a modular space telescope," *Journal of Astronomical Telescopes, Instruments, and Systems*, vol. 2, no. 4, p. 041207, 2016.

[14] J. G. Katz, S. Mohan, and D. W. Miller, "On-orbit assembly of flexible space structures with swarm," *AIAA Infotech@ Aerospace*, 2010.
[15] D. Barnhart, L. Hill, E. Fowler, R. Hunter, L. Hoag, B. Sullivan, and P. Will, "A market for satellite cellularization: a first look at the implementation and potential impact of satlets," in *Proceedings of AIAA Space 2013Conference and Exposition. Washington DC: AIAA*, pp. 2579–2589, 2013.
[16] C. Underwood, S. Pellegrino, H. Priyadarshan, H. Simha, C. Bridges, A. Goel, T. Talon, A. Pedivellano, Y. Wei, F. Royer, *et al.*, "Aarest autonomous assembly reconfigurable space telescope flight demonstrator," in *Proceedings of the 69th International Astronautical Congress (IAC)*, International Astronautical Federation (IAF), 2018.
[17] D. Izzo, L. Pettazzi, and M. Ayre, "Mission concept for autonomous on orbit assembly of a large reflector in space," in *56th International Astronautical Congress*, 2005.
[18] W. R. Oegerlea, L. D. Feinberga, L. R. Purvesa, T. T. Hydea, H. A. Thronsona, J. A. Townsenda, M. Postmanb, M. R. Bolcara, J. G. Budinoffa, B. H. Deana, *et al.*, "Atlast-9.2 m: a large-aperture deployable space telescope," in *Proc. SPIE*, vol. 7731, pp. 77312M–1, 2010.
[19] H. P. Stahl, "Jwst mirror technology development results," in *Proc. SPIE*, vol. 6671, pp. 667102–1, 2007.
[20] M. D. Lallo, "Experience with the hubble space telescope: 20 years of an archetype," *Optical Engineering*, vol. 51, no. 1, 2012.
[21] M. D. Perrin, A. Sivaramakrishnan, C.-P. Lajoie, E. Elliott, L. Pueyo, S. Ravindranath, and L. Albert, "Updated point spread function simulations for jwst with webbpsf," in *Space Telescopes and Instrumentation 2014: Optical, Infrared, and Millimeter Wave*, vol. 9143, p. 91433X, International Society for Optics and Photonics, 2014.
[22] J. S. Knight, D. S. Acton, P. Lightsey, A. Contos, and A. Barto, "Observatory alignment of the james webb space telescope," in *Space Telescopes and Instrumentation 2012: Optical, Infrared, and Millimeter Wave*, vol. 8442, p. 84422C, International Society for Optics and Photonics, 2012.
[23] D. Baiocchi and H. P. Stahl, "Enabling Future Space Telescopes : Mirror Technology Review and Development Roadmap," tech. rep., 2009.
[24] G. Cole, R. Garfield, T. Peters, W. Wolff, K. Johnson, R. Bernier, C. Kiikka, T. Nassar, H. A. Wong, J. Kincade, T. Hull, B. Gallagher, D. Chaney, R. J. Brown, A. McKay, and L. M. Cohen, "An overview of optical fabrication of the JWST mirror segments at Tinsley," *Space Telescopes and Instrumentation I: Optical*, vol. 6265, no. June 2006, p. 25, 2006.
[25] H. P. Stahl, L. D. Feinberg, and S. C. Texter, "JWST primary mirror material selection," vol. 5487, p. 818, International Society for Optics and Photonics, oct 2004.
[26] M. Clampin, "JWST Telescope Optics: Progress Report," 2011.
[27] Materion Corporation, "MatWeb: Beryllium, Be."
[28] R. Weast, *CRC Handbook of Chemistry and Physics*. Boca Raton: CRC Press, 62 ed., 1981.
[29] R. Ross, *Metallic Materials Specification Handbook*. London: Chapman & Hall, 4th ed., 1992.
[30] ASM International, *Metals Handbook Vol 2 Properties and Selection: Nonferrous Alloys and Special-Purpose Materials*. 10th ed., 1990.
[31] A. Nayer, *The Metals Databook*. New York: McGraw-Hill, 1997.

[32] D. Lide, *CRC Handbook of Chemistry and Physics*. Boca Raton: CRC Press, 80th ed., 1999.
[33] R. M. Warden, "Cryogenic Nano-Actuator for JWST," 2006.
[34] "Launch Log." `http://www.planet4589.org/space/log/launch.html`, 2018. [Online; accessed 18-Nov-2018].
[35] "Union of Concerned Scientists Satellite Catelog." `https://www.ucsusa.org/nuclear-weapons/space-weapons/satellite-database#.W-HGuZNKg70`, 2018. [Online; accessed 18-Nov-2018].
[36] W. S. Koon, M. W. Lo, J. E. Marsden, and S. D. Ross, *Dynamical Systems, the Three-Body Problem and Space Mission Design*. Marsden Books, 1.2 ed., 2011.
[37] V. Szebehely, *Theory of Orbits: The Restricted Problem of Three Bodies*. Academic Press, 1967.
[38] M. R. Bolcar, K. Balasubramanian, M. Clampin, J. Crooke, L. Feinberg, M. Postman, M. Quijada, B. Rauscher, D. Redding, N. Rioux, S. Shaklan, H. P. Stahl, C. Stahle, and H. Thronson, "Technology development for the advanced technology large aperture space telescope (ATLAST) as a candidate large uv-optical-infrared (LUVOIR) surveyor," in *Proc.SPIE*, vol. 9602, pp. 9602 – 9602 – 14, 2015.
[39] D. L. Richardson, "A note on a lagrangian formulation for motion about the collinear points," *Celestial Mechanics*, vol. 22, 1980.
[40] D. L. Richardson, "Analytic construction of periodic orbits about the collinear points," *Celestial Mechanics*, vol. 22, 1980.
[41] D. J. Grebow, *Generating Periodic Orbits in the Circular Restricted Three-Body Problem with Applications to Lunar South Pole Coverage*. Purdue University, 2006.
[42] E. Kolemen, *Optimal Configuration of a Planet-Finding Mission Consisting of a Telescope and a Constellation of Occulters*. Princeton University, 2008.
[43] E. Jones, T. Oliphant, P. Peterson, *et al.*, "SciPy: Open source scientific tools for Python," 2001–.
[44] J. Kierzenka and L. F. Shampine, "A bvp solver based on residual control and the maltab pse," *ACM Transactions on Mathematical Software (TOMS)*, vol. 27, no. 3, pp. 299–316, 2001.
[45] K. Howell and H. Pernicka, "Numerical determination of lissajous trajectories in the restricted three-body problem," *Celestial Mechanics*, vol. 41, pp. 107–124, 1988.
[46] S. Gong, H. Baoyin, and J. Li, "Solar sail three-body transfer trajectory design," *Journal of guidance, control, and dynamics*, vol. 33, no. 3, pp. 873–886, 2010.
[47] C. McInnes, *Solar Sailing: Technology, Dynamics and Mission Applications*. Springer-Praxis Books, 1999.
[48] B. Dachwald, G. Mengali, A. A. Quarta, and M. Macdonald, "Parametric model and optimal control of solar sails with optical degradation," *Journal of Guidance, Control, and Dynamics*, vol. 29, no. 5, pp. 1170–1178, 2006.
[49] T.-K. Yeh, W. Chen, X. Tianhe, and G. Xu, "Analytical solution of a satellite orbit disturbed by atmospheric drag," *Monthly Notices of the Royal Astronomical Society*, vol. 410, pp. 654–662, 12 2010.
[50] B. Lewis, "Complete 1976 standard atmosphere," 2007–.
[51] NOAA, "U.s. standard atmosphere," *US Government Printing Office*.
[52] V. Coverstone, "Technique for escape from geosynchronous transfer orbit using a solar sail," *JGCD*, 2003.

[53] M. Macdonald and C. McInnes, “Realistic earth escape strategies for solar sailing,” *Journal of Guidance, Control, and Dynamics*, vol. 28, no. 2, pp. 315–323, 2005.
[54] C. Zhang, F. Topputo, F. Bernelli-Zazzera, and Y.-S. Zhao, “Low-thrust minimum-fuel optimization in the circular restricted three-body problem,” *Journal of Guidance, Control, and Dynamics*, vol. 38, no. 8, pp. 1501–1510, 2015.
[55] E. Kolemen and N. Kasdin, “Optimization of an occulter-based extrasolar-planet-imaging mission,” *JGCD*, vol. 35, pp. 172–185, 2012.
[56] J. A. Englander and B. A. Conway, “Automated solution of the low-thrust interplanetary trajectory problem,” *Journal of Guidance, Control, and Dynamics*, pp. 15–27, 2016.
[57] C. G. Sauer Jr., “Optimum solar-sail interplanetary trajectories,” in *AIAA/AAS Astrodynamics Conference*, 1976.
[58] G. Mengali and A. A. Quarta, “Optimal three-dimensional interplanetary rendezvous using non-ideal solar sail,” *Journal of Guidance, Control, and Dynamics*, vol. 28, no. 1, pp. 173–177, 2005.
[59] J. S. Hudson and D. J. Scheeres, “Reduction of low-thrust continuous controls for trajectory dynamics,” *Journal of guidance, control, and dynamics*, vol. 32, no. 3, pp. 780–787, 2009.
[60] P. E. Gill, W. Murray, and M. A. Saunders, “Snopt: An sqp algorithm for large-scale constrained optimization,” *SIAM J. on Optimization*, vol. 12, pp. 979–1006, Apr. 2002.
[61] J. R. Maly, S. A. Haskett, P. S. Wilke, E. Fowler, D. Sciulli, and T. E. Meink, “Espa: Eelv secondary payload adapter with whole-spacecraft isolation for primary and secondary payloads,” in *Smart Structures and Materials 2000: Damping and Isolation*, vol. 3989, pp. 430–440, International Society for Optics and Photonics, 2000.
[62] MOOG, “ESPA User’s Guide,” tech. rep., 2018.
[63] K. Karuntzos, “United Launch Alliance Rideshare Capabilities To Support Low-Cost Planetary Missions,” tech. rep.
[64] “DoD Space Test Program Secondary Payload Planner ’ s Guide For Use On The EELV Secondary Payload Adapter,” tech. rep., 2001.
[65] J. R. Maly, P. S. Wilke, P. M. Wegner, L. Berenberg, and G. E. Sanford, “ESPA from Concept to Flight Hardware,”
[66] Tolomatic, “Premium High Force Linear Actuator,” tech. rep.
[67] C. D. Edwards, T. C. Jedrey, E. Schwartzbaum, A. S. Devereaux, R. Depaula, M. Dapore, and T. W. Fischer, “The Electra Proximity Link Payload for Mars Relay TeIecommunications and Navigation,” (Bremen), 2003.
[68] Planetary Systems Corporation, “2000785G MkII MLB User Manual,” tech. rep.
[69] Eagle Picher, “SAR-10199 Aerospace Battery,” tech. rep.
[70] L. Johnson, B. Cohen, L. Mcnutt, and J. Castillo-Rogez, “Solar Sail Propulsion for Interplanetary CubeSats,” tech. rep.
[71] L. Johnson, R. Young, E. Montgomery, and D. Alhorn, “STATUS OF SOLAR SAIL TECHNOLOGY WITHIN NASA,” tech. rep.
[72] D. M. Murphy, “Validation of a Scalable Solar Sailcraft System,” 2006.
[73] C. Garner and M. Leipold, “A Summary of Solar Sail Technology Developments and Proposed Demonstration Missions,” tech. rep.
[74] J. Banik, S. Kiefer, M. Lapointe, and P. Lacorte, “On-orbit validation of the roll-out solar array,” *IEEE Aerospace Conference Proceedings*, vol. 2018-March, pp. 1–9, 2018.